



Durham E-Theses

Light storage and control of photon-photon interactions in a cold Rydberg gas

MAXWELL, DANIEL, THOMAS

How to cite:

MAXWELL, DANIEL, THOMAS (2013) *Light storage and control of photon-photon interactions in a cold Rydberg gas*, Durham theses, Durham University. Available at Durham E-Theses Online: <http://etheses.dur.ac.uk/7757/>

Use policy

The full-text may be used and/or reproduced, and given to third parties in any format or medium, without prior permission or charge, for personal research or study, educational, or not-for-profit purposes provided that:

- a full bibliographic reference is made to the original source
- a [link](#) is made to the metadata record in Durham E-Theses
- the full-text is not changed in any way

The full-text must not be sold in any format or medium without the formal permission of the copyright holders.

Please consult the [full Durham E-Theses policy](#) for further details.

Light storage and control of photon-photon interactions in a cold Rydberg gas

Daniel Maxwell

Abstract

The effect of strong interatomic interactions on an optical field stored in Rydberg states of a cold atomic gas is investigated. Due to their large dipole moments Rydberg atoms interact very strongly with each other. The strength of these interactions can be significant over length scales of several microns. An effect known as dipole blockade leads to a suppression in the number of Rydberg excitations supported in a medium of finite size. The experiments described in this thesis aim to exploit this effect to create a medium with a non-linear response which occurs at the level of single-photons.

A cold atomic cloud is tightly confined such that only a few Rydberg excitations are supported. It is shown that the dipole blockade phenomenon leads to strong photon-photon interactions, resulting in the generation of quantum states of light. A microwave field is used to control the strength and range over which the interactions between the stored optical photons occur. In addition, it is shown that the propagation of the optical field through the medium is non-trivial. Preliminary evidence is presented suggesting that the slow-light group delay in the medium is dependent on the number of propagating photons.

Light storage and control of photon-photon interactions in a cold Rydberg gas

Daniel Maxwell

A thesis submitted in partial fulfilment
of the requirements for the degree of
Doctor of Philosophy



Department of Physics
Durham University

August 20, 2013

Contents

	Page
Abstract	i
Title	ii
Contents	iii
List of Figures	vi
Declaration	ix
Acknowledgements	xi
1 Introduction	1
1.1 Aims and motivation	1
1.2 Single-photon non-linearities	2
1.3 Rydberg EIT	4
1.4 Quantum memories	5
1.5 Thesis summary	6
1.6 Publications arising from this work	8
I Atom-atom & Atom-light interactions	9
2 Rydberg atoms	10
2.1 Properties	10
2.2 Dipole-dipole interactions	11
2.3 Dipole blockade	13
3 Atom-light interactions	16
3.1 Two-level atom	17
3.1.1 Rabi oscillations	19
3.2 Three-level atom	20
3.2.1 EIT	21
3.2.2 Dark-state polaritons and photon storage	23
3.3 Four-level atom	26

II	Experimental demonstration of photon storage in Rydberg states	28
4	Experiment	29
4.1	Setup	29
4.2	MOT	33
4.2.1	Experimental sequence	34
4.2.2	Optimisation	35
4.3	Single-photon detection	38
4.3.1	Quantum states of light	38
4.3.2	Intensity correlations	39
5	Microscopic dipole trap	43
5.1	Theory	43
5.2	Trap loading and optimisation	46
5.2.1	Rough alignment	46
5.2.2	Trap loading	48
5.2.3	Fine alignment	53
5.3	Trap modulation	56
5.3.1	Sequence	57
5.3.2	Probe absorption	59
5.3.3	Loss	62
5.4	Atom temperature	65
5.4.1	Experimental geometry	67
6	EIT	69
6.1	Experimental procedure	69
6.2	Weak probe	70
6.3	Strong probe	72
6.4	Microwave dressing	75
7	Photon storage	79
7.1	Experimental procedure	79
7.2	Optimisation	82
7.3	Saturation	86
7.4	Photon statistics	90
7.4.1	Predictions of Monte-Carlo model	90
7.4.2	Observation of quantum states of light	92
7.4.3	Preliminary evidence for a photon number dependent group delay	95
8	Coherent control of Rydberg polaritons	100
8.1	Coherent evolution of polariton state	100
8.2	Weakly-Interacting Regime	103
8.3	Strongly-Interacting Regime	105
8.3.1	Interaction induced dephasing	106

8.3.2	Modification of photon statistics	108
8.3.3	Dependence on initial conditions and microwave pulse parameters	113
III	Outlook	120
9	Conclusions and future work	121
9.1	Overview of the experiment	121
9.2	Plans for an improved experimental setup	122
9.3	Future experiments	124
	Appendices	124
A	Appendix	125
A.1	Dipole trap laser system	125
A.2	Crossed dipole trap	128
A.3	Absorption spectra of dipole trapped atoms	129
A.4	EIT transients	130
	Bibliography	133

List of Figures

Figure	P0.8ge
1.1 Two-qubit CNOT phase-gate using a pair of single photons. . .	3
2.1 Dipole-dipole interaction between two atoms	12
2.2 Dipole blockade	14
3.1 Excitation scheme for a 2-level system and its steady-state susceptibility.	18
3.2 Rabi oscillations of a two-level atom.	19
3.3 Excitation scheme for a 3-level system and its steady-state susceptibility	20
3.4 Excitation scheme for a 4-level system and its steady-state susceptibility	26
4.1 Schematic of the experimental setup.	30
4.2 Atomic level schemes used for laser-cooling and Rydberg ex- citation of atoms.	32
4.3 Schematic of the timing sequence used for loading and imaging the atoms in the MOT.	34
4.4 Optimising the atom number loaded into the MOT.	35
4.5 Minimising the temperature of the atoms after the molasses cooling stage.	36
4.6 MOT loading curve.	37
4.7 Schematic of Hanbury Brown Twiss interferometer.	41
4.8 Variation of the measured value of the second order correlation function in the presence of a background signal.	42
5.1 Zemax calculations to determine the sensitivity of the effective focal length of the input aspheric lens on the properties of the input beam.	47
5.2 Timing sequence for loading the dipole trap.	49
5.3 Optimising the number of atoms loaded into the dipole trap. .	50
5.4 Dependence of atom number in the dipole trap on its overlap time with the MOT loading stage.	51
5.5 Measurement of trap lifetime.	53
5.6 Fluorescence images of atoms in the MOT and dipole trap. . .	54

5.7	Fluorescence signal as a diagnostic of dipole trap alignment.	55
5.8	Variation in probe absorption with the focal position of the dipole trap.	56
5.9	Dipole trap modulation sequences.	57
5.10	Characterising the loss of atoms when modulating the dipole trap.	58
5.11	Comparison of absorption signal when the dipole trap is turned off completely, with the absorption signal when the dipole trap is modulated.	59
5.12	Probe absorption as a function of repumping parameters.	60
5.13	Variation in probe absorption and atom number with dipole trap depth.	61
5.14	Decay in probe absorption signal over trap modulation time due to atom loss from the dipole trap.	63
5.15	Fluorescence signal from atoms as a function of dipole trap modulation time when applying a probe beam.	64
5.16	Release and recapture procedure.	66
5.17	Release and recapture results.	67
5.18	Schematic of the experimental geometry.	67
6.1	Pulse sequence used to measure EIT spectra.	70
6.2	Probe absorption and EIT spectra in the weak probe regime.	71
6.3	Suppression of transmission on EIT resonance for a strong probe beam.	73
6.4	Pulse sequence used for studying EIT spectra with microwave coupling.	75
6.5	Variation of EIT spectra with frequency of applied microwave field.	76
6.6	Variation of EIT spectra with power of applied microwave field.	78
7.1	Experimental procedure for the storage and retrieval of probe photons.	80
7.2	Variation in retrieved photon signal over trap modulation time.	81
7.3	Mean number of retrieved photons per store/ retrieve cycle as a function of the width of the probe pulse.	83
7.4	Dependence of the storage and retrieval process on the Rabi frequency of the coupling laser.	84
7.5	Dependence of EIT bandwidth and storage bandwidth on Ω_c	85
7.6	Modification of the photon number distribution of the probe field in the regime of dipole blockade.	87
7.7	Results of Monte-Carlo model simulating saturation in the number of photons stored.	88
7.8	Mean number of retrieved photons per store/ retrieve cycle as a function of probe power for different Rydberg states.	89
7.9	$g^{(2)}(0)$ predicted by Monte-Carlo model.	91

7.10	Measurements of $g^{(2)}$, where the entire retrieved field has been binned.	92
7.11	Dependence of $g^{(2)}(0)$ on probe power.	93
7.12	Variation of $g^{(2)}$ away from $\tau = 0$	95
7.13	Variation of $g^{(2)}(0)$ across the retrieved pulse.	96
7.14	Retrieved pulse shape and variation of $g^{(2)}(0)$ across the pulse, fitted using a model which assumes a photon number dependent group delay.	98
8.1	Procedure for quantum state control of stored photons.	102
8.2	Rabi oscillations of polaritons between the $60s_{1/2}$ and $58p_{3/2}$ Rydberg states.	104
8.3	Rabi oscillations of polaritons between the $60s_{1/2}$ and $59p_{3/2}$ Rydberg states.	106
8.4	Eigenvalues of polariton Hamiltonian as a function of their separation.	108
8.5	Variation in number of polaritons with Ω_{μ}	109
8.6	Modification of $g^{(2)}$ of the retrieved field after microwave coupling.	110
8.7	Variation in $g^{(2)}(0)$ with trap modulation time after microwave coupling.	111
8.8	Modification of the shape of the retrieved pulse after microwave coupling.	113
8.9	Rabi oscillations for different microwave pulse durations.	114
8.10	Phase shift of Rabi oscillations.	115
8.11	Rabi oscillations for different probe powers.	116
8.12	Variation of the visibility and many-body nature of the Rabi oscillations as a function of the number of polaritons written.	117
8.13	Rabi oscillations at different microwave frequencies.	119
A.1	The home-built laser system used to provide light for the dipole trap.	126
A.2	Characterisation of the output power from the TA.	128
A.3	Fluorescence from dipole trapped atoms as a function of transverse trap position.	129
A.4	Absorption spectra of dipole trapped atoms.	130
A.5	Transients in EIT.	131

Declaration

I confirm that no part of the material offered has previously been submitted by myself for a degree in this or any other University. Where material has been generated through joint work, the work of others has been indicated.

Daniel Maxwell
Durham, August 20, 2013

The copyright of this thesis rests with the author. No quotation from it should be published without their prior written consent and information derived from it should be acknowledged.

*To my family,
and Lucy.*

Acknowledgements

I am enormously grateful to my supervisor Prof. Charles Adams for his relentless support and encouragement throughout my PhD. Charles' enthusiasm and scientific intuition is inspiring, and I feel privileged to have worked on his experiment.

My thanks must also go to the second supervisor on the experiment, Matthew Jones. The success of the experiment is largely indebted to Matt's insight and experience when it came to solving difficult technical issues. Like Charles, Matt is incredibly encouraging and enthusiastic, and I feel very fortunate to have had such a fantastic supervisory team.

I have also been very lucky to work with a range of PhD students and post-docs on the experiment. I will be forever grateful to Jonathan Pritchard and Alexandre Gauguet for the training they gave me during the early days of my PhD. They were both incredibly patient and gave me the opportunity to become fully integrated with the team from day-one. The results in this thesis would not have been possible if not for their fantastic work on the construction of the experiment, and their continued contribution after leaving Durham. I am also extremely grateful to the second postdoc I worked with on the experiment, David Szwer. David has always been on hand to discuss every aspect of the experiment, and we have done a lot of head-scratching together. Thanks must also go to David Paredes who is never short of ideas when it comes to answering difficult questions. I wish David all the best during his time running the experiment. Both David S. and David P. have been heavily involved in the experiments described in this thesis. I must also thank Hannes Busche who has made an active contribution to the publications arising from this work. I wish him the very best in building the next generation version of the experiment. The experiment has very much been a team effort, so I must reiterate my thanks to the people mentioned above.

I would like to thank the AtMol group as a whole for providing such an enjoyable and supportive working environment. In particular, thanks must go to Kevin Weatherill, Ifan Hughes, Ulrich Krohn, and Graham Lochhead for providing various forms of technical advice. I would also like to thank my office mates James Keaveney, Lee Weller, and Tim Wiles, especially for making the months of thesis writing bearable.

Finally I must thank my family and my girlfriend Lucy for their continued support in everything that I do. This thesis is dedicated to them.

Chapter 1

Introduction

This thesis describes work towards the realisation of a medium whose response to an incident optical field is non-linear at the level of single-photons. The motivation for the creation of such a medium is outlined in the following section. The concept of single-photon non-linearities will then be briefly introduced. Following this, the system employed in this experiment, which combines Rydberg atoms with the technique of electromagnetically induced transparency, will be described. Finally, quantum memories will be briefly discussed.

1.1 Aims and motivation

The remarkable level of control over isolated quantum systems that is now possible is a consequence of major technological and theoretical advances over the past few decades. For example, the invention of lasers [1] has provided coherent, intense light sources which can be used to manipulate the internal states of particles. The development of laser-cooling [2, 3] was also a major breakthrough as it allows extremely cold, optically dense gases to be produced. The low temperature of laser-cooled particles leads to increased interaction times with laser fields and long coherence times. The preparation of cold samples of trapped particles is now essentially routine.

It is this enormous level of control that has made theoretical ideas regarding the storage and processing of information in quantum systems experimen-

tally feasible. In quantum information processing information is stored in quantum bits, known as qubits. The key difference between these quantum bits compared with classical bits, is that qubits can be in a superposition of their 0 and 1 states. It has been shown that processing information stored in qubits is more efficient than with classical computing for certain problems [4]. In addition to its applications in computing, cryptography is another field where quantum information can bring major advances [5]. Quantum cryptography has already been implemented in commercial applications [6]. One of the aims of the experiment described in this thesis is to demonstrate proof-of-principle techniques for use in *optical* quantum information processing. Photons have emerged as ideal candidates for the storage and transmission of quantum information due to their weak coupling with the environment and fast transmission rates [7]. However, to create a deterministic gate where the information in these photons can be *processed*, it is necessary to introduce interactions between the photons. The current experiment aims to exploit the strong dipole-dipole interactions between highly excited atoms to mediate interactions between photons.

In addition to the demonstration of strong photon-photon interactions, another aim of the experiment is to observe the associated generation of non-classical states of light. In particular, single photon generation is an area of interest since optical quantum computing schemes generally require a deterministic source of single photons. Theoretical proposals exist which exploit strong interatomic interactions to generate single photons [8].

1.2 Single-photon non-linearities

The key gate operation which is required for the construction of a quantum computer is the CNOT gate [4]. In a CNOT gate the state of a target qubit is flipped, conditional on the state of a control qubit. Consider a two-qubit gate where the effect of the control qubit on the state of the target qubit can be written as [9]

$$\frac{1}{\sqrt{2}}(|0\rangle + |1\rangle)|1\rangle \rightarrow \frac{1}{\sqrt{2}}(|0\rangle + e^{-i\phi}|1\rangle)|1\rangle. \quad (1.1)$$

Here the first term on each side corresponds to the target qubit, and the second term is the control qubit. The phase, ϕ , picked up by the $|1\rangle$ component of the target qubit depends on the strength of its interaction with the control qubit. To realise a CNOT gate a π -phase shift is required. If the state of the control qubit is $|0\rangle$ then there should be no interaction, giving $\phi = 0$.

An example of the implementation of the CNOT gate is schematically illustrated in figure 1.1 [7]. A target photon is incident upon a 50:50 beam-splitter creating the state on the left hand side of equation 1.1. In this case the states $|0\rangle$ and $|1\rangle$ correspond to the two paths of the qubit. The final state after recombination of the two paths depends on the acquired phase-shift. If a π -phase shift is acquired then the NOT operation is realised. For this to be a CNOT gate the phase shift should only be acquired if the control qubit is in the state $|1\rangle$.

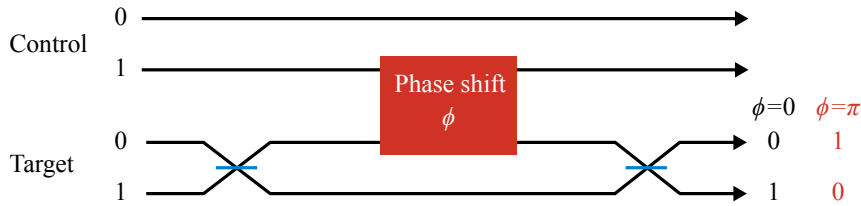


Figure 1.1: Two-qubit CNOT phase-gate using a pair of single photons. The target photon is incident upon a 50:50 beam-splitter. It then acquires a phase shift, ϕ , if the control photon is in state $|1\rangle$. If $\phi = \pi$ then the CNOT operation is realised. Adapted from [7].

The issue is realising a sufficiently strong interaction such that a single photon in the control arm causes a π -phase shift of a single photon in the target arm. It has been proposed that a Kerr non-linearity could be exploited to produce this large phase shift [10]. The Kerr non-linearity refers to the intensity dependence of a materials refractive index [11]. Normally a very large laser intensity is required to produce a significant Kerr non-linearity. However, large non-linearities are also possible using electromagnetically induced transparency (EIT) [12]. A cross-phase modulation scheme exploiting EIT has been proposed [13], where the presence of one beam modifies the refractive index experienced by the other. However, it was later shown that pulse distortion arising from an inhomogeneous phase acquisition limits the fidelity

of such an operation, even if it were realised at the single-photon level [9, 14]. Nevertheless, the route of cross phase modulation is still being pursued using more elaborate schemes [15]. Although single-photon non-linearities have yet to be demonstrated using cross-phase modulation, an all-optical switch operating at the level of a few-hundred photons has been demonstrated [16]. Large single-photon non-linearities have been proposed [17] and demonstrated in cavity QED systems [18]. However, up until very recently [19–21] non-linearities approaching the single-photon level had not been realised in free space. The aim of the current experiment is to demonstrate such a non-linearity. The realisation of a CNOT gate is beyond the scope of this work.

1.3 Rydberg EIT

Rydberg atoms (chapter 2) and EIT (section 3.2.1) will be discussed independently in more detail later in this thesis. At this stage key concepts will be introduced to motivate the use of Rydberg EIT in realising strong optical non-linearities.

A Rydberg state is a state of high principal quantum number [22]. Rydberg atoms are extremely sensitive to external electric fields and as a consequence exhibit a very large Kerr effect [23]. The main property of Rydberg atoms which is of interest in the current context is their strong interactions with other Rydberg atoms. For sufficiently strong interactions, one Rydberg excitation can block the Rydberg excitation of all other atoms in a surrounding volume. This phenomenon is known as dipole blockade [24].

EIT is an effect where a medium is transparent to a laser frequency to which it would otherwise be opaque [25]. The simplest setting for EIT is a three-level system driven by two laser fields. The transparency arises on two-photon resonance where two excitation pathways interfere destructively [12]. The laser field is partially converted into an atomic coherence as it propagates through the atomic medium. When the field reaches the end of the medium it is then converted back into an electromagnetic excitation. The field which leaves the sample is therefore sensitive to interactions between the atoms, or

dephasing of the atomic states.

In the experiments described in this thesis one of the atomic levels used in EIT is a Rydberg state [26]. The aim is to map the strong interactions between Rydberg atoms onto an optical field which undergoes EIT. The effect of dipole blockade has already been shown to produce strong absorptive nonlinearities [27, 28]. Recently these nonlinearities were demonstrated the single-photon level, where a filter for single photons was demonstrated [20]. The large dispersive component of the non-linearity has also been probed in a cavity Rydberg EIT system [29].

It has been proposed that the long-range interactions between Rydberg atoms could be used to realise a homogeneous π -phase shift between two single photons undergoing EIT [30]. The homogeneity of the phase shift in this scheme is a consequence of the fact that the dipole-dipole interaction is non-local. The pulse distortion issues arising with the cross phase modulation schemes mentioned in the previous chapter (which rely on the Kerr effect) could therefore potentially be circumvented.

1.4 Quantum memories

The ability to store and retrieve quantum information is essential for communication over large distances [31], and synchronisation in quantum computation [32]. A quantum memory is a medium where the reversible storage of quantum information is possible [33]. The storage and retrieval of optical photons from quantum memories has been realised in several different experimental settings [32]. Tremendous progress has been made in solid-state systems [34] where photon storage efficiencies of around 70% [35] have been demonstrated. However, one difficulty is that it is difficult to generate *single* photons with a sufficiently narrow bandwidth for use with solid-state memories [36]. In contrast, the generation of single photons [19, 37, 38] and their subsequent storage [37, 38] has been successfully demonstrated using atomic gases. It has also been shown that cold atomic gases can provide a long-lived quantum memory, with photon storage possible on time scales of tens of seconds [39].

As is demonstrated in this work, a quantum memory also provides a suitable environment for the controlled interaction between photons. The storage of photons in Rydberg states means that the retrieved light field is sensitive to the interactions between the Rydberg atoms [19, 21]. In this experiment photon storage is performed by exploiting the slow-light effect associated with EIT. The group velocity of the field undergoing EIT can be controlled by varying the intensity of the second control field. The quantum statistical properties of the field have previously been shown to be preserved using this method [37, 38]. Storage efficiencies were previously limited to approximately 50% in both cold atoms [40], and in thermal samples [41], using EIT. However in a recent breakthrough, a storage efficiency of 78% has been demonstrated [42].

1.5 Thesis summary

The majority of the work presented in this thesis concerns experimental techniques and measurements. However, in part I relevant theoretical concepts necessary for understanding the experimental data are briefly introduced. Part II is mostly devoted to describing experimental techniques, presentation of experimental data and its interpretation. In part III experimental limitations and potential future work will be discussed.

The thesis is structured as follows:

- **Chapter 2** A brief introduction to the special properties of Rydberg atoms is given to motivate their use in this work. Particular attention is paid to the interactions between Rydberg atoms, and the phenomenon of *dipole blockade*.
- **Chapter 3** The interaction between a classical, monochromatic light source and an atom is introduced. The form of the electric susceptibility for two, three, and four level atoms is discussed. Effects associated with a three level atom such as electromagnetically induced transparency and photon storage are considered in most detail as they are relevant to the experiments described in this work.

- **Chapter 4** The experimental setup is presented. Key experimental techniques are described, including laser-cooling in a magneto-optical trap, and single photon detection. In addition, theoretical concepts regarding quantum states of light are introduced.
- **Chapter 5** The loading and alignment of a microscopic dipole trap is discussed. Important experimental methods such as intensity modulation of the dipole trap are presented. The trap is characterised in terms of atom number, temperature, and loss.
- **Chapter 6** Experimental measurements of electromagnetically induced transparency using Rydberg atoms are presented. The effects of dipole blockade on the spectra are discussed. Microwave dressing of the Rydberg atoms is also performed.
- **Chapter 7** The storage of optical photons in Rydberg states is studied. Further evidence of dipole blockade is presented. The generation of non-classical light fields provides evidence of photon-photon interactions. In addition, preliminary evidence suggesting that the group delay through the atomic medium is dependent on the number of propagating photons is presented.
- **Chapter 8** Experiments involving the coherent control of the state of the stored photons using a microwave field are presented. Rabi oscillations of the stored photons are observed between two microwave coupled Rydberg states. The strength of the photon-photon interactions in the atomic medium can also be controlled with the microwave field.
- **Chapter 9** The experimental findings are summarised. The limitations of the experimental setup and potential improvements are discussed. Future experiments which could be performed with an improved setup are identified.

1.6 Publications arising from this work

- D. Maxwell, D. J. Szwer, D. Paredes-Barato, H. Busche, J. D. Pritchard, A. Gauguet, M. P. A. Jones, and C. S. Adams. *Microwave control of the interaction between two optical photons*, arXiv:1308.1425 [physics.atom-ph].
- D. Maxwell, D. J. Szwer, D. Paredes-Barato, H. Busche, J. D. Pritchard, A. Gauguet, K. J. Weatherill, M. P. A. Jones, and C. S. Adams. *Storage and Control of Optical Photons Using Rydberg Polaritons*, Phys. Rev. Lett. **110**, 103001 (2013).
- S. Bettelli, D. Maxwell, T. Fernholz, C. S. Adams, I. Lesanovsky, and C. Ates. *Exciton dynamics in emergent Rydberg lattices*, arXiv:1306.0869 [physics.atom-ph].

Related publications

- J. D. Pritchard, D. Maxwell, A. Gauguet, K. J. Weatherill, M. P. A. Jones, and C. S. Adams. *Cooperative Atom-Light Interaction in a Blockaded Rydberg Ensemble*, Phys. Rev. Lett. **105**, 193603 (2010).
- M. Tanasittikosol, J. D. Pritchard, D. Maxwell, A. Gauguet, K. J. Weatherill, R. M. Potvliege, and C. S. Adams. *Microwave dressing of Rydberg dark states*, J. Phys. B: At. Mol. Opt. Phys. **44** 184020 (2011).
- S. Sevinçli *et al.* *Quantum interference in interacting three-level Rydberg gases: coherent population trapping and electromagnetically induced transparency*, J. Phys. B: At. Mol. Opt. Phys. **44** 184018 (2011).

Part I

Atom-atom & Atom-light interactions

Chapter 2

Rydberg atoms

In this chapter the special properties of Rydberg atoms will be briefly introduced. This will motivate their use in the experiments described in this thesis. The main property of interest is the strong dipole-dipole interaction which arises between neighboring Rydberg atoms. The key concepts regarding these interactions will therefore be discussed. In addition, the phenomenon of dipole blockade will be introduced as this is vital to the interpretation of many experimental results discussed in later chapters.

2.1 Properties

A Rydberg state is a state of high principal quantum number, n . The experiments described in this thesis use ^{87}Rb atoms which have a single valence electron. The term Rydberg atom will therefore be used to describe an atomic state where the valence electron occupies a state of large n .

Even using the simple Bohr theory of an atom, the interesting properties of Rydberg atoms become immediately apparent. Bohr's theory models a Hydrogen atom as an electron moving in a classical orbit around a single proton. This theory can also be applied to Rydberg atoms where a valence electron in a highly excited state experiences an approximately Coulombic potential arising from the net charge of the nucleus and the core electrons. Bohr's theory shows that the valence electrons orbital radius increases as n^2 and its binding energy decreases as n^{-2} . This means that Rydberg atoms

have valence electrons with very small binding energies and with large orbits. As a result of this it is relatively easy to ionize Rydberg atoms and to cause strong shifts in their energy levels using an external electric field [22].

The scaling of key properties of Rydberg atoms with n are listed below [22].

- Dipole moment for transitions between adjacent Rydberg levels: n^2 .
- Energy separation between adjacent Rydberg levels: n^{-3} .
- Polarisability: n^7 .
- Radiative lifetime of Rydberg state (for low angular momentum states): n^3 .

The n^2 scaling of the dipole moment gives an enormous level of control over the interaction strength through the choice of the atomic state [43]. This makes Rydberg atoms ideal qubits in the implementation of neutral atom quantum gates [44]. In addition to their strong inter-atomic interactions, another desirable feature of Rydberg atoms is their long lifetime, scaling as n^3 .

2.2 Dipole-dipole interactions

The sensitivity of Rydberg atoms to external fields means that they interact strongly with each other via dipole-dipole interactions. The electric dipole-dipole interaction energy between two atoms is given by [45]

$$V(\mathbf{r}) = \frac{1}{4\pi\epsilon_0} \left(\frac{\mathbf{p}_1 \cdot \mathbf{p}_2}{r^3} - 3 \frac{(\mathbf{p}_1 \cdot \mathbf{r})(\mathbf{p}_2 \cdot \mathbf{r})}{r^5} \right). \quad (2.1)$$

Here r is the separation between the two atoms, and \mathbf{p}_1 and \mathbf{p}_2 are their dipole moments. It is important to note that the two atoms under consideration do not have permanent electric dipole moments. However, the dipole-dipole interaction causes mixing of the initial two-atom state with other two-atom states accessible within the selection rules for electric dipole transitions [46]. The dipole moments $\mathbf{p}_{1,2}$ correspond to transitions between these states. The dipole-dipole interaction is illustrated schematically in figure 2.1.

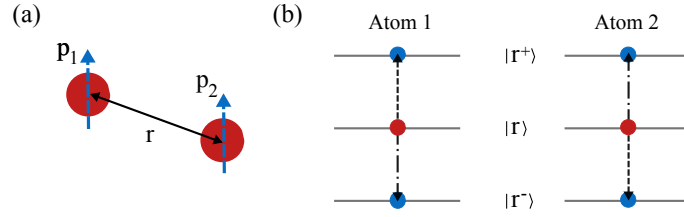


Figure 2.1: Dipole-dipole interaction between two atoms. (a) Induced dipole moment $p_{1,2}$ of two atoms separated by a distance r . (b) The dipole-dipole interaction couples the initial state of the atoms, $|r\rangle$, to neighboring states.

The dipole-dipole interaction energy causes coupling between adjacent states of the form

$$|nlj\rangle + |nlj\rangle \rightarrow |n^+l^+j^+\rangle + |n^-l^-j^-\rangle. \quad (2.2)$$

Here both atoms are initially in the state $|nlj\rangle$, and the states $|n^+l^+j^+\rangle$ and $|n^-l^-j^-\rangle$ are higher and lower in energy respectively. The energy separation between the states involved in the excitation transfer is given by

$$\Delta = E(n^+l^+j^+) + E(n^-l^-j^-) - 2E(nlj), \quad (2.3)$$

where the energies, E , are those of the bare states i.e. when the two atoms are at infinite separation.

The form of the dipole-dipole interaction depends on the separation between the atoms. For small separations, resonant dipole-dipole interactions dominate, scaling as $1/r^3$. These arise when the magnitude of the interaction energy is of the same order as the energy separation, Δ , to the neighboring pair states [46]. The strength of the interaction is parameterised by the state dependent C_3 coefficient, scaling as n^4 [43]. Resonant dipole-dipole interactions cause a change of state of the atoms, as illustrated in figure 2.1 (b). For larger separations the dipole-dipole interaction couples states off-resonantly. In this case van der Waals interactions dominate, scaling as $1/r^6$. These are not associated with a change in the internal state of the atoms. The state dependent van der Waals coefficient, C_6 , parameterises the interaction strength, scaling as n^{11} [43]. For the $60s_{1/2}$ state, the inter-atomic separation at which the van der Waals and resonant dipole-dipole regimes cross-over is approximately $2.1 \mu\text{m}$ [47].

As will become clear later when experiments exploiting the dipole blockade effect are discussed, resonant dipole-dipole interactions are often desirable due to their long range. The length scale requirement for the realisation of resonant dipole-dipole interactions can be lifted by applying an external field. For example, a DC electric field can be used to Stark-shift adjacent pair states into resonance [48, 49]. Similarly, off-resonant microwave frequency AC fields can be used [50]. In these methods the interaction from the resonantly coupled pair state dominates, leading to resonant dipole-dipole interactions. Resonant microwave fields have also been shown to induce resonant dipole-dipole interactions through the mixing of opposite parity Rydberg states [51, 52]. External fields therefore provide an additional level of control over the strength and range of dipole-dipole interactions.

2.3 Dipole blockade

The experiments described in this thesis involve the laser excitation of a cloud of atoms initially in the ground state, $|g\rangle$, to a Rydberg state $|r\rangle$. It is important to consider the effect of dipole-dipole interactions on the Rydberg excitation process. Throughout this section it will be assumed that the van der Waals interaction dominates, although the described effects also occur in the regime of resonant dipole-dipole interactions.

In figure 2.2 (a) the effect of the van der Waals interaction on the Rydberg excitation of two ground state atoms, $|gg\rangle$, is illustrated schematically. The energy of the pair states is plotted as a function of the interatomic separation. The dipole-dipole interaction energy for two ground state atoms or for the singly excited Rydberg state is taken to be negligible. The energy of these pair states is therefore independent of the interatomic separation. A laser field resonant with the transition $|g\rangle \rightarrow |r\rangle$ can excite the singly excited Rydberg state, $|gr\rangle$ or $|rg\rangle$. The doubly excited Rydberg state, $|rr\rangle$, can also be excited for large inter-atomic separations. However, due to the strong van der Waals interaction between Rydberg atoms, the energy of the doubly excited Rydberg state $|rr\rangle$ is strongly shifted at small separations. If the detuning of this state from the resonant laser frequency is larger than the excitation linewidth, Γ , then excitation of $|rr\rangle$ is not possible. The sup-

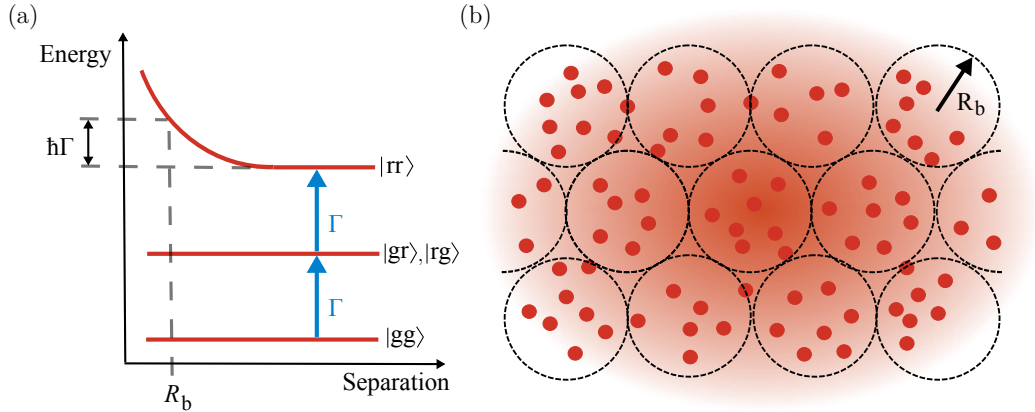


Figure 2.2: Dipole blockade. (a) Two atoms initially in the ground state, $|gg\rangle$, are excited by a laser field resonant with the transition $|g\rangle \rightarrow |r\rangle$. For interatomic separations below R_b , the doubly excited state $|rr\rangle$ is detuned from resonance. (b) In the regime of dipole blockade spheres of radius R_b can only contain a single Rydberg excitation.

pression of states containing multiple Rydberg excitations is known as dipole blockade [24, 53]. An analogous effect is the Coulomb blockade in electron transport [54].

The excitation of a single atom to a Rydberg state can in principle block the Rydberg excitation of N atoms contained within a region of space known as the blockade sphere. The blockade radius, R_b , is found by equating the weakest van der Waals interaction, i.e. the interaction between two atoms separated by the blockade radius, to the excitation linewidth. This gives [55],

$$R_b = \left(\frac{C_6}{\hbar\Gamma} \right)^{\frac{1}{6}}. \quad (2.4)$$

Atoms separated by R_b have the minimum energy shift to be blocked. Since the van der Waals interaction scales as n^{11} , the blockade radius scales as $n^{11/6}$. Blockade radii of more than $10 \mu\text{m}$ have been observed [56].

The avoided volume between Rydberg excitations is illustrated schematically in figure 2.2 (b). For a sufficiently dense sample, the number of allowed Rydberg excitations is less than the total number of atoms. This can be observed as a saturation in the fraction of atoms excited into the Rydberg state [57]. An associated suppression in the width of the Rydberg atom number distribution has also been observed [58]. In addition, spatial correlations be-

tween Rydberg excitations have been experimentally verified [59, 60]. It has been proposed that a crystal of Rydberg excitations could be formed using a technique where the frequency of the laser excitation pulse is chirped [61].

It is important to note that within each blockade sphere the single Rydberg excitation is collectively shared between all N atoms [24]. The collective Rydberg state formed results in a number of interesting effects. For example, the collective Rabi frequency of the transition between the ground state and the Rydberg state is enhanced by a factor of \sqrt{N} relative to the single-atom Rabi frequency [62]. In addition, as will be discussed in section 3.2.2, singly excited symmetric collective states can produce directional emission of single photons [8, 63].

Dipole blockade forms the basis of the experiments described in this thesis. As will be shown, the suppression in the number of Rydberg excitations is accompanied by a non-linear response of the atomic medium to the laser field. Under certain conditions this can be exploited to produce single photon non-linearities.

Chapter 3

Atom-light interactions

In this chapter the interaction between a coherent light field and a sample of atoms will be discussed. Although this work is centered around quantum light fields interacting with a highly non-linear medium, it is more instructive to initially consider the atom-light interaction in a simpler setting. Therefore in this chapter monochromatic, classical light fields will be considered, and it will be assumed that the response of the atomic medium to the field is linear. Non-linear effects will be discussed briefly in chapter 6, although this is mostly from a qualitative viewpoint.

The effect of the light field is to polarise the atoms in the medium according to

$$\mathbf{P} = \epsilon_0 \chi \mathbf{E}. \quad (3.1)$$

Here \mathbf{P} is the polarisation of the medium, χ is its susceptibility, and \mathbf{E} is the electric field of the light. The polarisation is the dipole moment, $\mathbf{d} = -e\mathbf{r}$, per unit volume. The change in the field after passing through the medium can be characterised in terms of the fraction of its intensity transmitted, T , and its phase shift.

For a medium of length l , in the limit of small values of χ and when $I_0 \ll I_{\text{sat}}$,

$$T = \frac{I}{I_0} = \exp(-k\chi l) = \exp(-\text{OD}), \quad (3.2)$$

where k is the wavevector of the light in free-space, I_0 is the intensity incident upon the medium, and $\text{OD} = k\chi l$ is the optical depth of the medium. The

transmission is therefore related to the imaginary part of the susceptibility.

The real part of the susceptibility is related to the refractive index by $n = \sqrt{1 + \chi_R}$, and is manifest as a phase shift of the light field through, $\Delta\phi = k\chi_R l/2$. In this work measurements of the phase shift are not performed.

The frequency dependence of the susceptibility will be considered for a few relevant systems. Particular attention is given to the case of a three-level atom since this is important for many of the experiments described in this thesis.

3.1 Two-level atom

The natural starting point when considering atom-light interactions is to take the case of a laser field incident upon a two-level atom. The laser field will be referred to as the probe field, with frequency ω_p . The excitation scheme of the two-level system is shown in figure 3.1 (a). The resonant transition between the ground state, $|1\rangle$, and the excited state, $|2\rangle$, occurs at a frequency ω_{21} . The detuning of the probe field from this resonance frequency is given by $\Delta_p = \omega_p - \omega_{21}$, and its Rabi frequency is denoted Ω_p . The excited state decays at a rate Γ_{21} due to spontaneous emission. In addition to spontaneous emission, another source of decoherence is the finite linewidth of the laser, γ_p [64]. The total dephasing rate is given by $\gamma_{21} = \Gamma_{21}/2 + \gamma_p$ [47, 64].

It is possible to calculate the components of the density matrix, $\rho = |\psi\rangle\langle\psi|$, of the two-level system starting from the master equation [65]. This provides a convenient way of incorporating decay of the components of the density matrix. In order to use analytical solutions of the master equation it will be assumed that the system is in a steady-state, and that the probe field is weak such that the atomic population remains in the ground state. The rotating wave approximation is also taken.

The polarisation of the medium can be written in terms of the coherence between levels $|1\rangle$ and $|2\rangle$, ρ_{21} , through [12, 64],

$$\mathbf{P} = \sum_{\mathbf{N}} \langle e\mathbf{r} \rangle / V = \rho_0 [\mathbf{d}_{12} \rho_{21} \exp(-i\omega_p t) + \text{c.c.}] \quad (3.3)$$

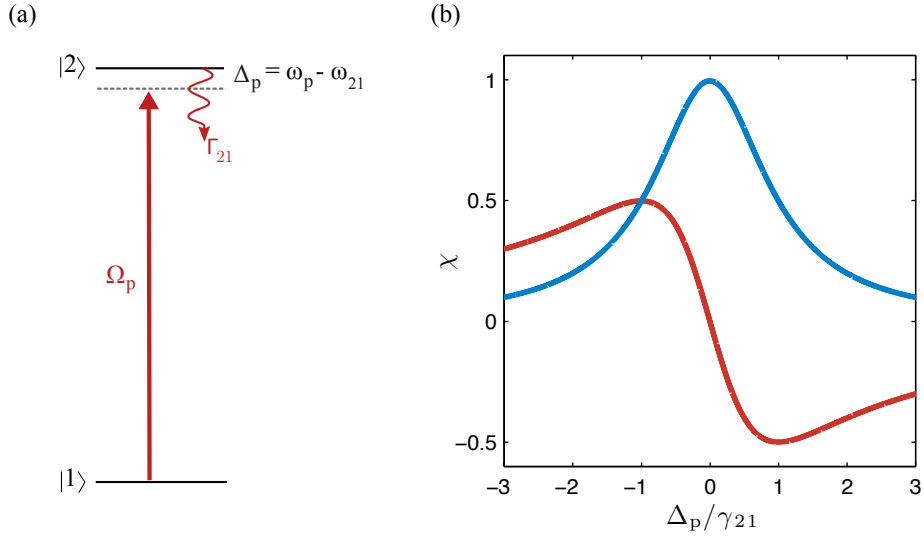


Figure 3.1: Excitation scheme for a 2-level system coupled to a probe laser field, and its steady-state susceptibility. (a) The probe field couples the ground state, $|1\rangle$, to an excited state, $|2\rangle$, with a Rabi frequency of Ω_p . (b) The real (red line) and imaginary (blue line) parts of the steady-state susceptibility for $\Omega_p = 0.1\gamma_{21}$. The susceptibility is scaled in units of $d_{21}^2\rho_0/\epsilon_0\hbar\gamma_{21}$.

The expectation value of the transition dipole moment is summed over N atoms in a volume V , with density ρ_0 . The relation $\langle e\mathbf{r} \rangle = \text{Tr}(\rho e\mathbf{r})$ has been used to obtain the expression on the right-hand side. It has been assumed that the response of all N atoms to the probe field is the same. Using equation 3.1 to substitute for \mathbf{P} , it can be shown that χ is related to ρ_{21} by

$$\chi = \frac{-2d_{21}^2\rho_0\rho_{21}}{\epsilon_0\hbar\Omega_p}. \quad (3.4)$$

The expression for ρ_{21} obtained from the master equation in the steady-state, weak probe regime then gives [47, 65],

$$\chi = \frac{d_{21}^2\rho_0}{\epsilon_0\hbar} \frac{i\gamma_{21} - \Delta_p}{\Omega_p^2/2 + \gamma_{21}^2 + \Delta_p^2}. \quad (3.5)$$

The real and imaginary parts of the susceptibility are plotted in figure 3.1. The imaginary part of the susceptibility is centered around $\Delta_p=0$ with a half-width at half maximum of γ_{21} .

3.1.1 Rabi oscillations

The driven two-level atom will now be considered outside of steady-state conditions. It will be assumed that the atom is initially in the ground state, $|1\rangle$, and that the probe field is on resonance and has a constant Rabi frequency. Ignoring the effect of spontaneous emission from the excited state, it can be shown that the probability the atom is in the ground state, $P(|1\rangle)$, evolves with time as [66]

$$P(|1\rangle) = \cos^2\left(\frac{\Omega_p t}{2}\right). \quad (3.6)$$

The rotation angle, $\Theta = \Omega_p t$, governs the evolution of population between the states.

To include the effect of spontaneous emission the master equation is used. In figure 3.2 the excited state population, ρ_{22} , is plotted as a function of time. When the ratio of the spontaneous decay rate of the excited state to the Rabi frequency of the probe field is very small, high contrast oscillations of the population between the ground and excited state can be observed. As this ratio becomes larger, the Rabi oscillations are more heavily damped, and the

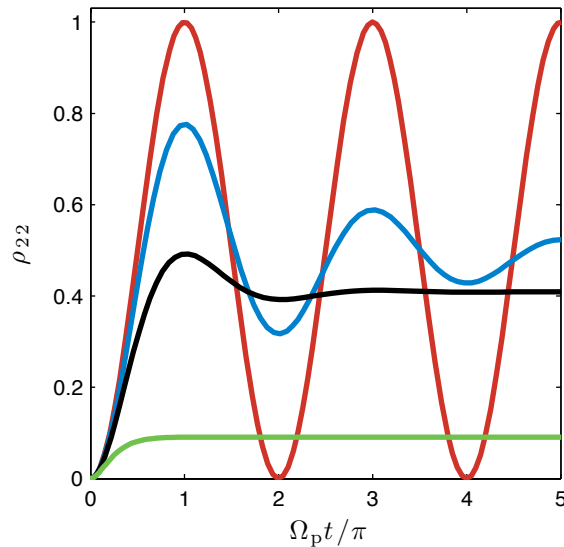


Figure 3.2: Rabi oscillations of a two-level atom. The excited state population, ρ_{22} , is plotted as a function of the rotation angle, $\Theta = \Omega_p t$. The different lines are for spontaneous decay rates of the excited state of $\Gamma_{21}/\Omega_p = 0$ (red), $\Gamma_{21}/\Omega_p = 2/9$ (blue), $\Gamma_{21}/\Omega_p = 2/3$ (black), and $\Gamma_{21}/\Omega_p = 3$ (green).

population approaches a steady state value more quickly.

3.2 Three-level atom

A three level system where state $|2\rangle$ is coupled to a third state, $|3\rangle$, will now be considered. The second laser field, with frequency ω_c , will be referred to as the coupling field. The resonant transition between the intermediate and upper excited state occurs at a frequency ω_{32} . The spontaneous decay rate from state $|3\rangle$ is given by Γ_3 . The excitation scheme is shown in figure 3.3 (a). A ladder scheme is adopted in this work, where the upper level is a Rydberg state. With a ladder scheme it is beneficial to arrange the probe and coupling lasers in a counter-propagating configuration as this minimises their Doppler mismatch.

In the regime of a weak probe field where the coherence ρ_{32} can be ignored, equation 3.4 is also valid for a 3-level atom. Substituting the steady-state expression for ρ_{21} yields [12, 47, 64],

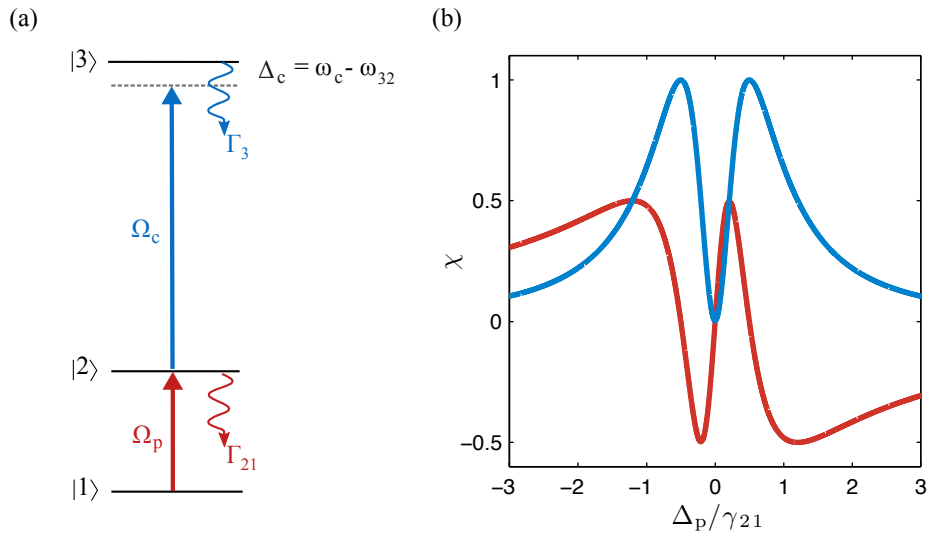


Figure 3.3: Excitation scheme for a 3-level system and its steady-state susceptibility. (a) The coupling field couples the intermediate state, $|2\rangle$, to state $|3\rangle$ with a Rabi frequency of Ω_c . (b) The real (red line) and imaginary (blue line) parts of the steady-state susceptibility for $\Omega_c = \gamma_{21}$, $\Delta_c = 0$, $\gamma_{31} = \gamma_{21}/1000$. The susceptibility is scaled in units of $d_{21}^2 \rho_0 / \epsilon_0 \hbar \gamma_{21}$.

$$\chi = \frac{i\rho_0 d_{21}^2 / \epsilon_0 \hbar}{\gamma_{21} - i\Delta_p + \frac{\Omega_c^2/4}{\gamma_{31} - i(\Delta_p + \Delta_c)}}, \quad (3.7)$$

where $\gamma_{31} = \Gamma_3/2 + \gamma_p + \gamma_c$ [47, 64], $\Delta_c = \omega_c - \omega_{32}$, and Ω_c is the Rabi frequency of the coupling laser. The linewidth of the coupling laser is γ_c .

The real and imaginary parts of the susceptibility are plotted in figure 3.3 (b). There is a remarkable difference in comparison with the susceptibility of a two-level atom. The imaginary part of the susceptibility now vanishes in a narrow window around the two-photon resonance, rendering the medium transparent to the probe field. This effect is known as electromagnetically-induced transparency (EIT). It can also be seen that the narrow transparency window coincides with a steep variation of the real part of the susceptibility. Note that a prominent transparency window, and therefore a steep dispersion feature, emerges when state $|3\rangle$ is metastable, such that $\Gamma_3 \ll \Gamma_2$. Some of the special properties associated with the three-level system will now be discussed in more detail.

3.2.1 EIT

The origin of the transparency on resonance can be understood by considering the eigenstates of the Hamiltonian governing the atom-light interaction [12]. It is found that a dark-state exists which does not contain a contribution from the intermediate level, $|2\rangle$. The dark state does not couple to the probe field, and is given by [12]

$$|D\rangle = \cos\theta|1\rangle - \sin\theta|3\rangle, \quad (3.8)$$

where,

$$\tan\theta = \frac{\Omega_p}{\Omega_c}. \quad (3.9)$$

For a weak probe field the dark-state corresponds to the ground state $|1\rangle$. There are also two other eigenstates [12], known as bright-states. However, destructive interference between these means that the probe field is not absorbed. As a result a transparency window emerges on resonance. Assuming

negligible decoherence of the state $|3\rangle$, i.e. $\gamma_{31} = 0$, the full width at half maximum of the EIT window is given by [12]

$$\Delta_{\text{EIT}} = 2 \frac{\Omega_c^2}{\sqrt{\Gamma_{21}\gamma_{21}}} \frac{1}{\sqrt{\rho_0\sigma l}}. \quad (3.10)$$

Here σ is the absorption cross section. It can be seen that the width of the EIT window scales as Ω_c^2 . The dependence of the width on the density-length product can be understood by examining equations 3.2 and 3.7. For large density-length products, where $k\rho_0 l \gg 1$, the transparency window narrows as only probe frequencies close to the center (where $\chi_I = 0$) are transmitted [67].

The probe pulse propagates through the medium with a group velocity given by [12]

$$v_{\text{gr}} = \frac{d\omega_p}{dk_p} = \frac{c}{n + \omega_p(dn/d\omega_p)} = \frac{c}{1 + \chi_R/2 + \frac{\omega_p}{2}(d\chi_R/d\omega_p)}. \quad (3.11)$$

This equation shows the dependence of the group velocity on the gradient of the real part of the susceptibility. As shown in figure 3.3, the gradient can be very large around the two-photon resonance leading to low group velocities [68, 69]. When both the probe and coupling lasers are on resonance, the group velocity is given by [12]

$$v_{\text{gr}} = \frac{c}{1 + \frac{6\pi}{k^2} \frac{\rho_0 c \Gamma_{21}}{\Omega_c^2 + \gamma_{31}\gamma_{21}}} = \frac{c}{n_{\text{gr}}}. \quad (3.12)$$

Here n_{gr} is the group index of the medium. It will be assumed that the group index is much bigger than 1, in which case it is given by

$$n_{\text{gr}} = \frac{6\pi}{k^2} \frac{\rho_0 c \Gamma_{21}}{\Omega_c^2 + \gamma_{31}\gamma_{21}}. \quad (3.13)$$

As with the width of the EIT window, the group velocity and group index are a function of Ω_c^2 . The decoherence terms impose an upper limit on the group index, and hence a lower limit on the group velocity.

The group velocity also depends on the optical depth of the medium. The density of the medium can be related to its optical depth over a propagation

distance z , OD_z , through [47]

$$\rho_0 = \frac{\text{OD}_z k^2}{6\pi z}. \quad (3.14)$$

The reduced group velocity of the probe pulse results in it acquiring a time delay relative to a free-space pulse. The time taken to propagate a distance z is given by

$$\tau = \frac{z}{v_{\text{gr}}} = \frac{\text{OD}_z \Gamma_{21}}{\Omega_c^2 + \gamma_{21} \gamma_{31}}. \quad (3.15)$$

Where equation 3.14 has been substituted into equation 3.12. This equation will be useful later when considering the time delay between different photons propagating through a highly non-linear medium.

3.2.2 Dark-state polaritons and photon storage

The propagation of the probe pulse through the medium can be described in terms of quasi-particles known as polaritons [70]. These correspond to superpositions of atomic and electromagnetic excitations. Under conditions of EIT the polariton field does not include the intermediate level, $|2\rangle$, and it is therefore referred to as a dark-state polariton [70]. The dark-state polariton field is given by [12]

$$\Psi(z, t) = \cos \theta \mathcal{E}_p(z, t) - \sin \theta \sqrt{\rho_0} \rho_{31}(z, t) e^{i\Delta k z}, \quad (3.16)$$

where the effective wavevector of the spin wave is given by $\Delta k = k_c - k_p$, \mathcal{E}_p corresponds to the probe electric field, and the mixing angle is related to the group index by $\tan^2 \theta = n_{\text{gr}}$. The atomic component of the polariton, contained in the coherence ρ_{31} , is referred to as a spin wave. In this thesis the terms polariton and spin wave will be used interchangeably.

Since the mixing angle between the electromagnetic and atomic components of the polariton is governed by the group index, it is dependent on Ω_c through equation 3.13. In the limit where $\Omega_c \rightarrow 0$, $\theta \rightarrow \pi/2$, and therefore $\cos \theta \rightarrow 0$ and $\sin \theta \rightarrow 1$. Thus the reduction of the group velocity towards zero is accompanied by the complete transfer of the electromagnetic field into the

atomic coherence. This is referred to as photon storage [71, 72]. Note that the reduction of Ω_c also leads to a modification of the dark state given by equation 3.8. As a result the atomic population is transferred to state $|3\rangle$ during storage.

An important consideration in the storage process is the role of the finite width of the transparency window, Δ_{EIT} . Frequency components of the probe pulse outside this window are absorbed. As Ω_c is reduced so is the width of the transparency window, as shown by equation 3.10. A consequence of this is that Ω_c must be reduced dynamically [73]. As Ω_c is lowered there is also a reduction in the width of the frequency distribution contained in the probe pulse. This reduction is proportional to the reduction in Δ_{EIT} [73]. Provided that the frequency distribution of the probe pulse is contained within the initial value of Δ_{EIT} , the storage efficiency is not bandwidth limited. For a probe pulse of a given duration one may think that Ω_c can simply be increased so that Δ_{EIT} exceeds its bandwidth. However, for the entire probe pulse to be stored it must be sufficiently spatially compressed such that it fits inside the medium. This requires a sufficiently low group velocity, and therefore sets an upper limit on the value of Ω_c . For the bandwidth and group velocity criteria to be both fulfilled, the optical depth of the medium must satisfy the condition $\text{OD} \gg 1$ [74, 75]. The optical depth of the medium therefore sets the upper limit on the storage efficiency.

The stored photons can be retrieved from the medium by increasing Ω_c . This leads to an increase in the group velocity and a transfer of the atomic coherence back into an electromagnetic excitation. Under ideal conditions the retrieved field is emitted into the same mode as the probe field. To understand the directionality of the retrieval it is important to note that the spin waves are *collective* atomic coherences [73]. For example a spin wave, $|\psi\rangle$, with a single atomic excitation has the form [8, 76]

$$|\psi\rangle = \frac{1}{\sqrt{N}} \sum_{j=1}^N e^{i\phi_j} |3^j\rangle, \quad (3.17)$$

where $|3^j\rangle = |1_1 1_2 \cdots 3_j \cdots 1_N\rangle$ denotes the state with atom j excited to state $|3\rangle$ with all other atoms in the ground state, and N is the number of atoms. The phase factors are given by $\phi_j = \Delta\mathbf{k} \cdot \mathbf{r}_j$, where \mathbf{r}_j is the position

of atom j . The phase of each term in the superposition ensures that the read-out emits a photon into the same spatial mode as the input. Since the directionality of the retrieval relies on constructive interference between each term, it increases with the number of atoms in the spin wave [8, 76], or equivalently with the optical depth of the medium. The retrieval efficiency into the phase-matched mode scales as approximately $1 - 1/\text{OD}$ [77]. The size of the medium determines the spatial width of the emission distribution [8, 76].

The retrieval efficiency of the spin wave is reduced by motional dephasing of the atoms during the storage interval. Motion of the atoms disturbs the initial phase structure written into the medium, given by the ϕ_j terms in equation 3.17. It can be shown that the retrieval efficiency, η_{ret} , decays exponentially in the regime where motional dephasing dominates [78],

$$\eta_{\text{ret}} = \exp\left(-\frac{t^2}{\tau^2}\right), \quad (3.18)$$

where t is the storage time. The $1/e$ lifetime of the spin wave, τ , depends on its wavelength and the atomic velocity through [78]

$$\tau = \frac{\Lambda}{2\pi v}. \quad (3.19)$$

Here v is the atomic velocity, and Λ is the period of the spin wave. The wavelength of the spin wave is related to the wavelength of the excitation lasers through

$$\Lambda = \frac{2\pi}{k_c - k_p}. \quad (3.20)$$

The lifetime of the spin wave essentially corresponds to the time it takes for the atoms to move a distance equal to its wavelength [78]. For photon storage in Rydberg states using a 780 nm probe beam and a 480 nm coupling beam, as in this thesis, $\Lambda \approx 1.2 \mu\text{m}$. The short spin wave period means that motional dephasing limits the lifetime of the spin wave to time scales on the order of a few μs [19]. Longer lifetimes can be achieved by using colder atoms, or by tightly confining the atoms in a lattice [79]. In addition much longer spin wave periods are achievable by storing the photons in a ground hyperfine state using a lambda excitation scheme [71, 72]. Using these methods, spin

wave lifetimes of tens of seconds have been demonstrated [39].

3.3 Four-level atom

A four level system where state $|3\rangle$ is coupled to a fourth state, $|4\rangle$, will now be considered. The excitation scheme is shown in figure 3.4 (a). For the experiments described in this thesis the third field, with frequency ω_μ , is a microwave field. The resonant transition frequency between the microwave coupled levels is ω_{43} .

Again in the steady-state, weak probe regime equation 3.4 holds. The susceptibility of the four level medium is given by [80]

$$\chi = -\frac{id_{21}^2\rho_0}{\epsilon_0\hbar} \left[i\Delta_p - \gamma_{21} + \frac{\Omega_c^2}{4} \left[i(\Delta_p + \Delta_c) - \gamma_{31} + \frac{\Omega_\mu^2}{4} \left[i(\Delta_p + \Delta_c + \Delta_\mu - (\gamma_p + \gamma_c + \gamma_{41})) \right]^{-1} \right]^{-1} \right]^{-1}. \quad (3.21)$$

Here $\gamma_{41} = \Gamma_4/2 + \gamma_\mu$, $\Delta_\mu = \omega_{43} - \omega_\mu$, and Ω_μ is the Rabi frequency of the

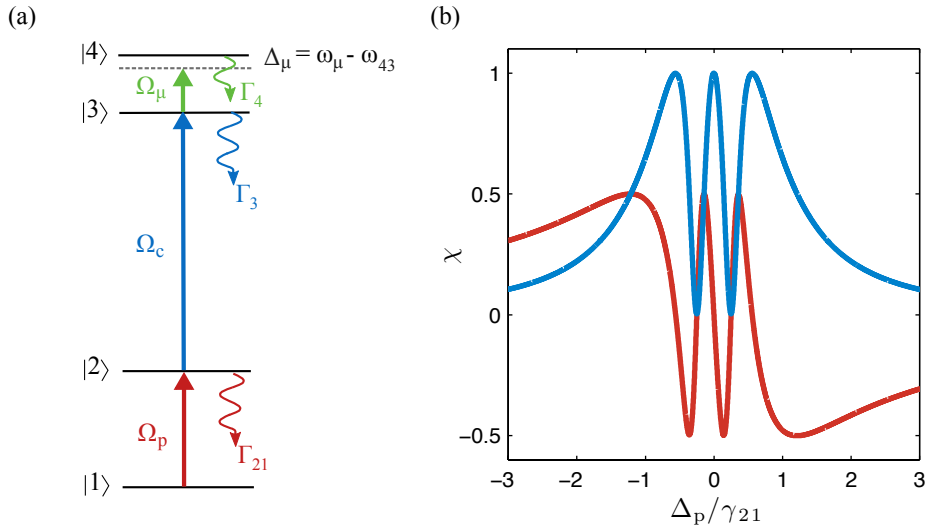


Figure 3.4: Excitation scheme for a 4-level system and its steady-state susceptibility. (a) The microwave field couples state $|3\rangle$ to state $|4\rangle$ with a Rabi frequency of Ω_μ . (b) The real (red line) and imaginary (blue line) parts of the steady-state susceptibility for $\Omega_\mu = \gamma_{21}/2$, $\Omega_c = \gamma_{21}$, $\Delta_\mu = 0$, $\Delta_c = 0$, $\gamma_{31} = \gamma_{21}/1000$, and $\gamma_{41} = 0$. The susceptibility is scaled in units of $d_{21}^2\rho_0/\epsilon_0\hbar\gamma_{21}$.

microwave field.

The real and imaginary parts of the susceptibility are plotted in figure 3.4 (b). The effect of the microwave field is to split the EIT resonance such that there are two transmission peaks.

Part II

Experimental demonstration of photon storage in Rydberg states

Chapter 4

Experiment

This chapter gives an overview of the experimental setup and key experimental methods. In order to obtain the largest single photon non-linearity, a single blockade sphere should be addressed by the excitation light. This can be achieved through tight focusing of the probe field. In order to maximise the optical depth of the medium, the atoms should also be tightly confined on a scale comparable to the size of the probe focus to achieve a high atomic density. This can be readily achieved using an optical dipole trap. Loading the dipole trap requires a cold atomic cloud as a source of atoms. This chapter includes a discussion of the laser cooling and trapping of atoms in a magneto-optical trap (MOT), with measurements of atom number and temperature. At this stage the details of loading the dipole trap will be ignored. This is discussed in chapter 5. The method of detecting and characterising optical fields at the single-photon level is also discussed.

4.1 Setup

A schematic of the experimental setup is shown in figure 4.1. Full details of the construction of the vacuum chamber and the initial beam alignment can be found in [47]. An aspheric lens pair (Lightpath 350240) mounted inside the vacuum chamber provides strong focusing of the laser beams used for atomic excitation and trapping. In principle, diffraction limited beam waists can be achieved with these lenses. The probe beam, at a wavelength of 780.2 nm,

propagates along the lens axis and is focused to a waist of $1.2 \pm 0.1 \mu\text{m}$. The 480 nm coupling beam, which counter-propagates with the probe beam, is focused to a waist of $17.9 \pm 0.3 \mu\text{m}$. The larger waist of this beam ensures that the Rabi frequency of the coupling laser is almost uniform across the region addressed by the probe beam. A red-detuned dipole trapping beam co-propagates with the probe beam, and is focused to a waist of $5.1 \pm 0.2 \mu\text{m}$. The dipole trap is loaded from a MOT formed in the center of the aspheric lens pair. The MOT is formed using a quadrupole trap created by a pair of current-carrying coils in an anti-Helmholtz configuration. Three pairs of rectangular coils provide a bias magnetic field for stray field cancellation. These coils are also used to provide a quantisation axis directed along the lens axis. Due to the small distance ($\approx 1 \text{ cm}$) separating the aspheric lens

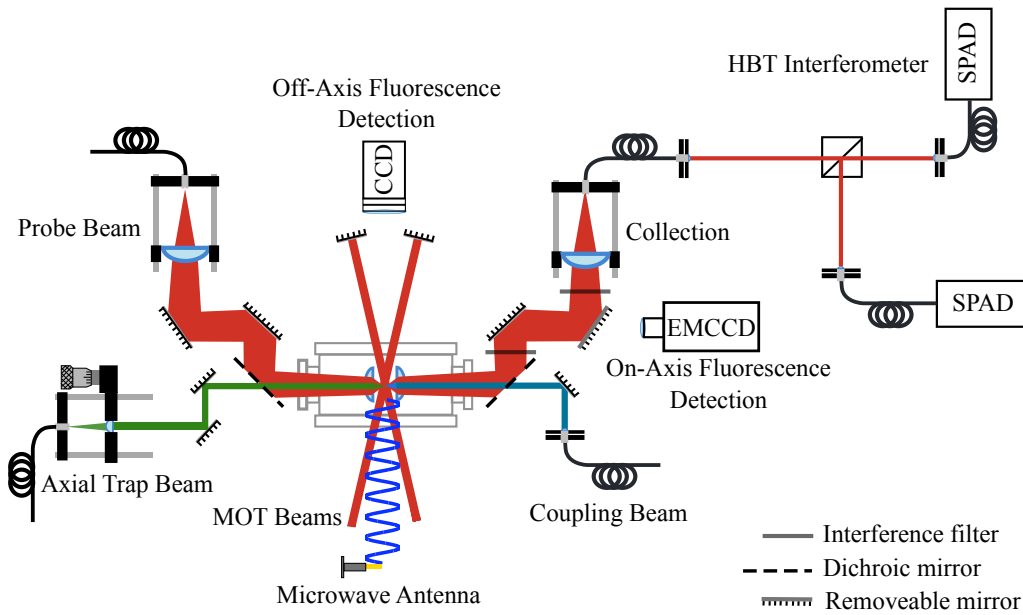


Figure 4.1: Schematic of the experimental setup, adapted from [47]. The vacuum chamber contains a pair of aspheric lenses which are used to strongly focus the excitation and trapping beams. A magneto-optical trap (MOT) is formed in the region between the lenses, from which an optical dipole trap is loaded. Photo-detection is provided mainly by single photon avalanche photodiodes (SPADs). A pair of CCD cameras are used to collect fluorescence from the atoms along, and perpendicular to, the lens axis. A stub antenna provides a microwave field which is incident perpendicular to the lens axis.

pair, the planar MOT beams intersect at an angle of 20° . At larger angles the MOT beams would clip the lenses.

After passing through the vacuum chamber the probe beam is coupled into an optical fibre and sent to single-photon avalanche photodiodes (SPADs). The single-photon detection system is described in more detail in section 4.3. The collection fibre for the probe beam can also be used to collect fluorescence from atoms trapped in the MOT or the dipole trap. In addition, CCD cameras are used to image the atom cloud. An off-axis CCD camera is used to collect fluorescence from atoms in the MOT. As will be discussed in section 4.2.2, this is mainly for measuring the atom number and the temperature of the atoms in the MOT. It is also used to position the atom cloud between the aspheric lens pair. A second, electron-multiplying CCD camera is used to collect fluorescence along the lens axis. This is mainly used to image atoms in the dipole trap.

When collecting the probe beam or fluorescence along the lens axis, several sources of background light must be suppressed in order to achieve reasonable signal to noise levels. The two main sources of background light come from the dipole trap beam and the coupling beam. These two wavelengths are attenuated using three narrow-band interference filters (Semrock LL01-780-25), which transmit more than 90 % of the 780 nm light.

In addition to the optical laser fields, a microwave field can be used to couple adjacent Rydberg states. The microwave field is emitted from a stub antenna and is incident at right-angles to the lens axis.

The excitation scheme for laser cooling in the MOT is shown in figure 4.2 (a). The MOT uses cooling light on the $5s^2S_{1/2}(F = 2) \rightarrow 5p^2P_{3/2}(F = 3)$ transition, and repump light on the $5s^2S_{1/2}(F = 1) \rightarrow 5p^2P_{3/2}(F = 2)$ transition. The details of the laser system and the modulation-transfer locking scheme used for the cooling light can be found in reference [47]. The probe light originates from the same laser as the cooling light. The repump laser is locked using the DAVLL technique described in [81].

The Rydberg excitation scheme is shown in figure 4.2 (b). The circularly polarised probe light drives σ^+ transitions on the same hyperfine transition as the cooling light. The coupling light drives σ^- transitions and is locked

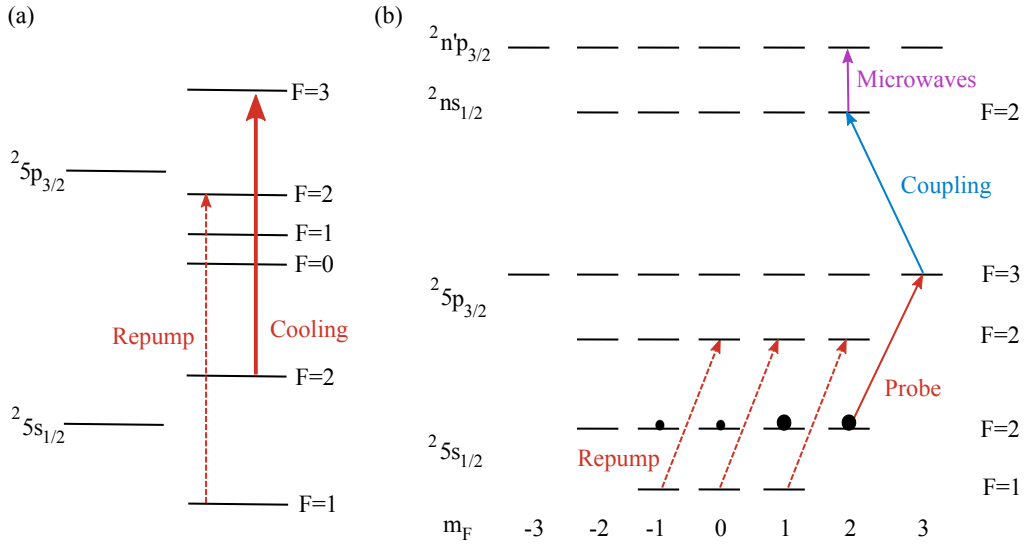


Figure 4.2: Atomic level schemes used for laser-cooling and Rydberg excitation of atoms. (a) The laser-cooling of ^{87}Rb uses two distinct laser frequencies. In addition to the cooling light, repump light pumps atoms which have fallen into the $F = 1$ ground state back onto the cooling transition. (b) Atoms are coupled to a $2ns_{1/2}$ Rydberg state via the intermediate $2^5p_{3/2}$ state using a probe (780.2 nm) and coupling laser (480 nm). Adjacent Rydberg states can be coupled with a microwave frequency field. Prior to Rydberg excitation repump light is required to pump atoms onto the probe transition.

using the EIT scheme described in [82]. The microwaves are linearly polarised along the quantisation axis and drive π transitions. Ideally atoms are optically pumped into the $5s^2S_{1/2}(F = 2, m_F = 2)$ state before excitation. This simplifies the situation since only one excitation pathway is followed. The coupling of the atoms to the probe field is also maximised for this transition [83]. Optical pumping is discussed briefly in section 5.3.2. However it is important to note that prior to excitation, while the atoms are held in the dipole trap, the atomic population is distributed among the $F = 1$ ground state. Repump light is therefore applied prior to excitation to pump atoms into the $F = 2$ ground state. The repump light originates from the same fiber as the probe beam and also drives σ^+ transitions.

The power and the detuning of the cooling, repump, and probe beams can be controlled using independent double-pass AOMs. For example, when

measuring probe absorption and EIT spectra the detuning of the probe beam is varied using an AOM. The power of the coupling light is controlled using an EOM (Leysop EM 200K). This allows fast switching of light which is useful for the photon storage experiments described in chapter 7.

4.2 MOT

Typically optical dipole traps have trap depths which are on the order of mK. Therefore in order to load a dipole trap a cold source of atoms is required. A cold atomic cloud is formed from a background of thermal ^{87}Rb atoms in the vacuum chamber, which originates from a dispenser. This cloud is formed using a magneto optical trap (MOT). The necessity of having a cold sample of atoms extends beyond loading of the dipole trap. In order for the blockade radius to be on a scale comparable to the extent of the atomic medium, Doppler broadening needs to be suppressed. In addition, as discussed in section 3.2.2, cold atoms are required to effectively store optical photons in Rydberg states. For room temperature atoms, motional dephasing would destroy the phase coherence of the spin wave on a time scale on the order of 1 ns [78]. In order to access usable time scales for storage and subsequent manipulation of the stored states, temperatures on the order of μK are required.

Since the optical dipole trap is loaded with atoms from the MOT, the cloud must be located in the region between the aspheric lens pair. This requires careful alignment of the MOT beams. The position of the MOT is also sensitive to the field produced by the bias coils, which means that the beam alignment has to be done in conjunction with optimisation of the magnetic field cancellation. Since the planar MOT beams intersect at an angle of 20° they form an interference pattern with a much greater contrast than if the MOT beams were in the standard 90° configuration. As the interference pattern is not stable, the atomic cloud moves to follow the high intensity fringes. This causes issues with the stability of the dipole trap loading as will be discussed later.

4.2.1 Experimental sequence

The experimental sequence used for loading the MOT and imaging the atoms is shown in figure 4.3. The MOT is typically loaded with a magnetic field gradient of 15 G cm^{-1} . Following this there is a molasses stage where the quadrupole coils are turned off, and the detuning of the cooling light is increased. The molasses stage reduces the temperature of the atoms via sub-Doppler cooling [84]. After a time-of-flight period of 1 ms where all of the laser light is extinguished, the atoms are imaged using the MOT beams for a period of 0.3 ms. The fluorescence from the atoms is collected on the off-axis CCD camera shown in figure 4.1. The pixel count of the CCD camera is calibrated using beams of known power. This allows the fluorescence counts from the atoms in the MOT to be converted into an atom number. The magnification of the imaging system is also calibrated so that the size of the cloud can be determined.

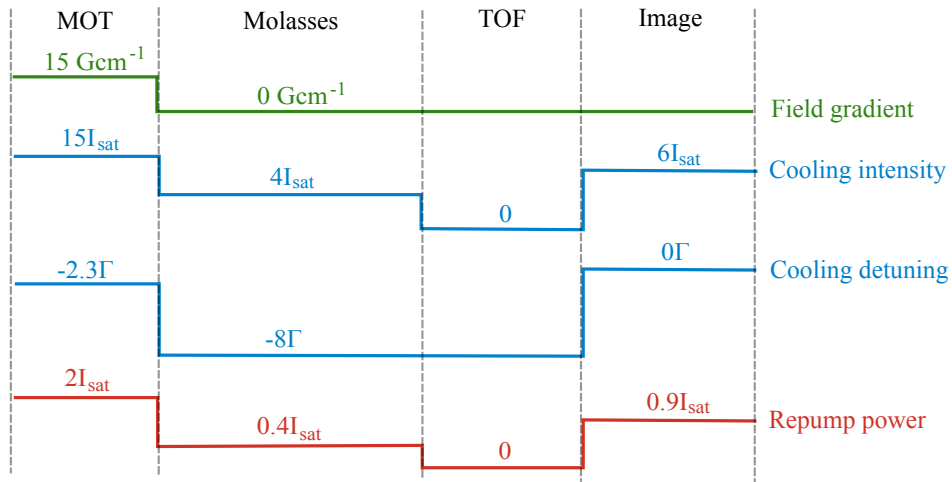


Figure 4.3: Schematic of the timing sequence used for loading and imaging the atoms in the MOT. The experimental parameters during the “MOT” stage are chosen to maximise the atom number, whilst the parameters during the “Molasses” stage are chosen to minimise the atom temperature.

4.2.2 Optimisation

The optimum experimental parameters for loading the MOT will now be studied. The two properties of interest are the number of atoms loaded, and their temperature. Since the atoms in the MOT are ultimately transferred to an optical dipole trap, a full characterisation of the MOT is not of primary importance. The experimental parameters were eventually adjusted to maximise the number of atoms loaded into the dipole trap (see section 5.2.2).

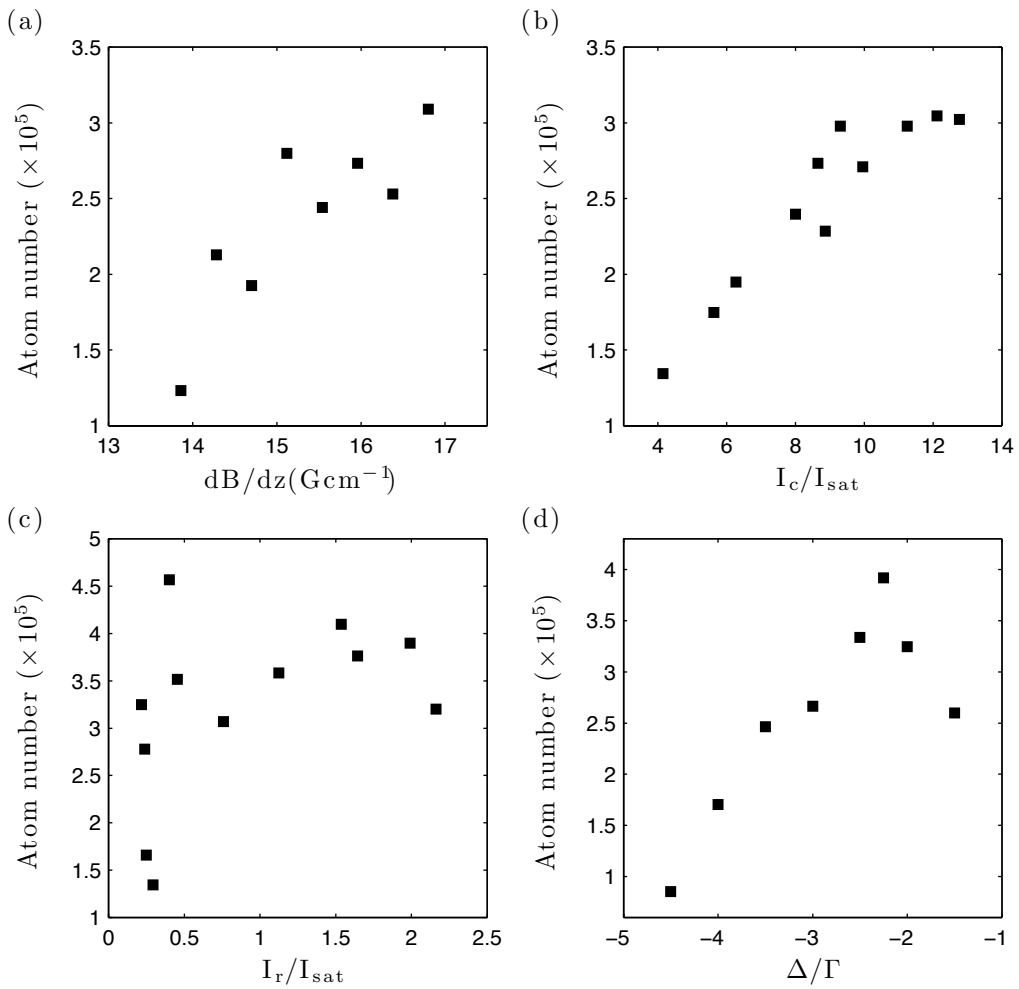


Figure 4.4: Optimising the atom number loaded into the MOT. (a) Effect of varying the magnetic field gradient, dB/dz , at the center of the quadrupole trap. (b) Effect of varying the intensity of the cooling light, I_c . (c) Effect of varying the intensity of the repump light, I_r . (d) Effect of changing the detuning of the cooling light, Δ .

However, optimisation of the MOT performance is a natural starting point before considering loading of the dipole trap.

The dependence of the number of atoms loaded into the MOT as a function of various parameters was first examined. The molasses stage of the sequence shown in figure 4.3 was not used for these experiments. The results shown in figure 4.4 show that the atom number is relatively sensitive to the magnetic field gradient and the cooling light parameters. After setting the

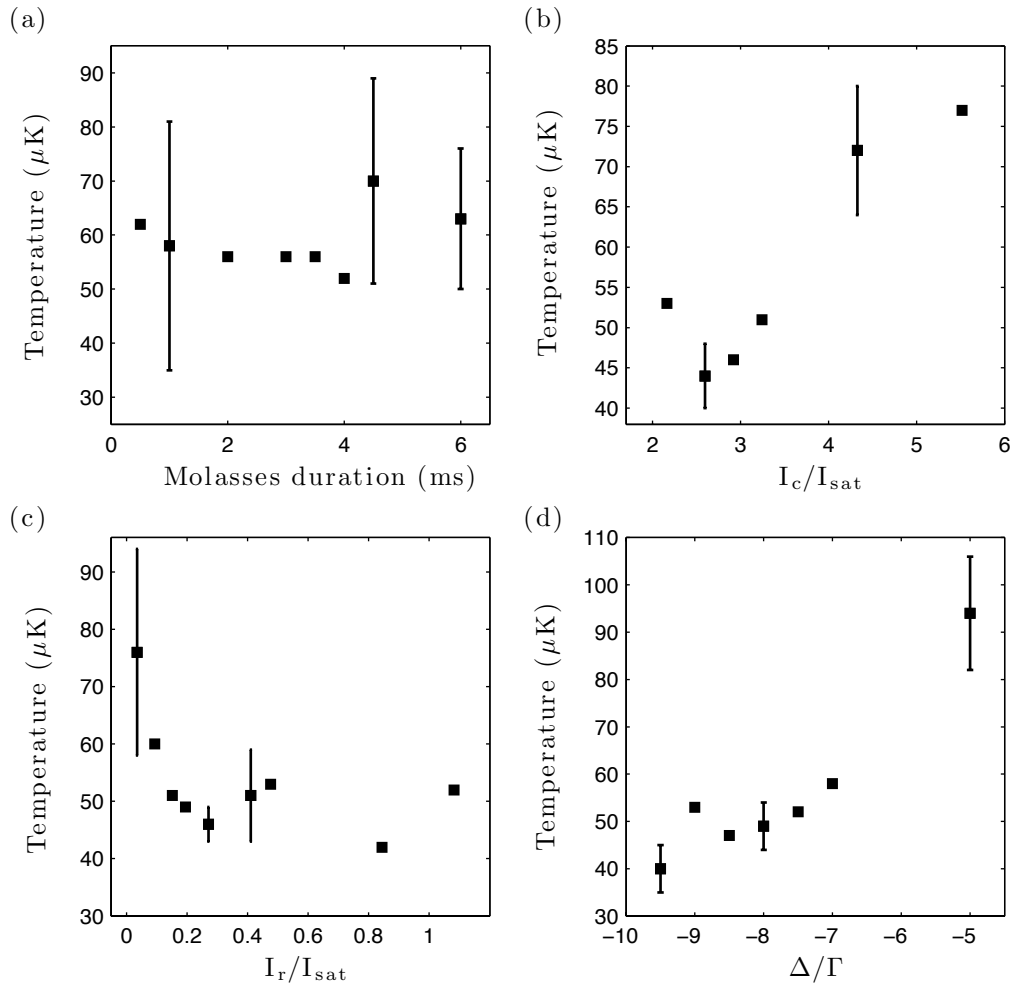


Figure 4.5: Minimising the temperature of the atoms after the molasses cooling stage. (a) Effect of changing the duration of the molasses stage. (b) Effect of changing the intensity of the cooling light, I_c . (c) Effect of changing the intensity of the repump light, I_r . (d) Effect of changing the detuning of the cooling light, Δ . Representative errorbars are shown on selected data points.

experimental parameters to optimise the atom number, a molasses stage was introduced to minimise the temperature of the atoms. The dependence of the atom temperature on the laser parameters during the molasses stage is plotted in figure 4.5. The temperature of the atoms was measured using a standard time-of-flight technique [85]. It can be seen that the temperature of the atoms is relatively insensitive to the duration of the molasses stage. In contrast to the optimum conditions for loading the trap, the minimum temperatures are obtained with far-detuned, relatively weak cooling light. This behavior is in qualitative agreement with other work, for example [86]. The methods used to measure the atom number and temperature are described in more detail in reference [47].

In figure 4.6 the number of atoms in the MOT is studied for different load times. It can be seen that after roughly 6 s the number of atoms has saturated. Note that due to systematic errors such as the collection efficiency of the imaging system, the fractional uncertainty on the atom number in the MOT is approximately 20%. For a 1 s load time around 2×10^5 atoms are loaded into the MOT. The cloud radius is roughly 0.1 mm (standard deviation of Gaussian fit). The atom number is probably limited by the small size of the MOT beams and the small angle at which the planar beams intersect.

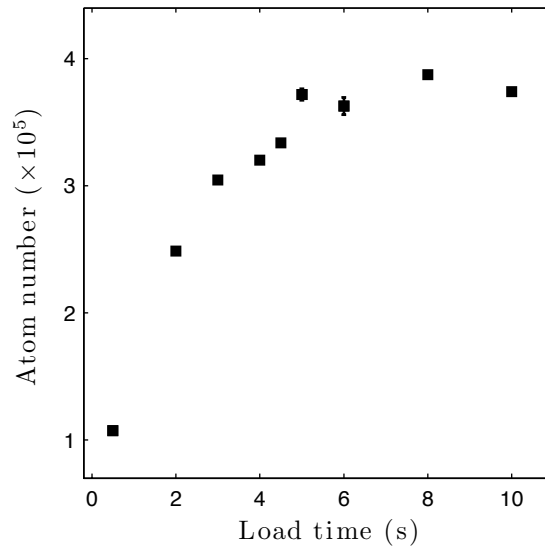


Figure 4.6: MOT loading curve. The atom number in the MOT saturates after a load time of roughly 6 s.

4.3 Single-photon detection

Since the aim of this experiment is to create and manipulate light at the single-photon level, a detection system capable of observing the quantum nature of a light field is required. As the probe beam is very tightly focused, the saturation intensity of the probe transition corresponds to powers in the region of only 40 pW. Low-noise, high sensitivity detectors are therefore required.

To detect these weak light fields, single-photon avalanche photodiodes (SPADs) were employed (PerkinElmer SPCM-AQRH-14-FC). The detectors have a dark-count rate of roughly 50 Hz and a dead-time of 28 ns. The typical background count rate on the SPADs is around 2 kHz. The 480 nm beam accounts for most (around 70 %) of the background light. The contribution from ambient light in the laboratory is negligible. The detectors can be gated with an external TTL signal. This is very useful as the detector only counts photons during the periods of interest, reducing background counts. The SPAD emits a TTL pulse for every counting event. These TTL pulses are time-tagged using a commercial counting card (SensL HRMTime). The time-tagged photon events are recorded on a computer for post-processing. The maximum photon count rate that can be recorded is limited by the counting card to roughly 2 MHz. The SPADs are capable of detecting count rates in the region of 25 MHz.

4.3.1 Quantum states of light

Classical and quantum states of light can be distinguished by measuring the photon statistics of the field under consideration [87]. To provide some insight into this we will consider two different quantum states of light. For simplicity single-mode excitations, where the electric field has a single wavevector and polarisation, will be considered.

A single photon state, $|1\rangle$, is an eigenstate of the photon number operator, $\hat{n} = \hat{a}^\dagger \hat{a}$, where

$$\hat{n}|n\rangle = n|n\rangle. \quad (4.1)$$

Here a^\dagger and a are creation and annihilation operators respectively. The

photon number state $|n\rangle$ has no number uncertainty, i.e. its variance $(\Delta n)^2 = 0$. Photon number states are also known as Fock states.

The photon number state will now be compared with the quantum state which is the closest analogue to a classical field, the coherent state. A coherent state is a good approximation to the field emitted by a laser [88]. It is given by

$$|\alpha\rangle = \exp\left(-\frac{|\alpha|^2}{2}\right) \sum_{n=0}^{\infty} \frac{\alpha^n}{(n!)^{1/2}} |n\rangle, \quad (4.2)$$

where $|\alpha|^2 = \langle n \rangle$. A coherent state is a superposition of photon number states with a Poissonian distribution. It follows that the number uncertainty of this state is non-zero. Its variance is equal to $(\Delta n)^2 = \langle n \rangle$. As will be discussed in the following section, classical fields *cannot* have sub-Poissonian photon statistics. A suppression in the photon number variance of a state below the level of a Poisson distribution can therefore reveal its non-classicality. In principle the photon statistics of a field can be obtained through a direct measurement of the photon number distribution. The Mandel Q parameter [89] can then be used to quantify the nature of the fields photon statistics. However, this method is sensitive to losses between the source and detector [90]. Another method, which is immune to losses, involves measuring intensity correlations of the light field [91]. This is introduced in the following section.

4.3.2 Intensity correlations

Temporal correlations in the intensity of a light field, known as its degree of second order coherence, $g^{(2)}$, can reveal non-classical properties. Initially a classical field, with cycle averaged intensity \bar{I} , will be considered. In this case $g^{(2)}$ can be written as [88]

$$g^{(2)}(\tau) = \frac{\langle \bar{I}(t)\bar{I}(t+\tau) \rangle}{\langle \bar{I}^2 \rangle}, \quad (4.3)$$

where $\tau = t_2 - t_1$ is the time delay between intensity measurements performed at t_1 and t_2 . This assumes a stationary light field where the processes responsible for producing intensity fluctuations are not time dependent [88]. In

other words $g^{(2)}$ is only a function of the delay between t_1 and t_2 , τ , not their absolute values. The angled brackets represent statistical averages. It will be assumed that $g^{(2)}$ has no spatial dependence. The $g^{(2)}$ function quantifies the correlation between intensity fluctuations separated by τ . Its calculation involves the cross correlation

$$\langle \bar{I}(t)\bar{I}(t+\tau) \rangle = \frac{1}{T} \int_T \bar{I}^*(t)\bar{I}(t+\tau)dt. \quad (4.4)$$

Here T represents a time scale which is large compared to the time scale of the intensity fluctuations being studied. Classically, the possible values of $g^{(2)}(\tau=0)$ are bounded by $1 \leq g^{(2)}(0) \leq \infty$ [88].

The experiments described in this thesis involve pulses of light, therefore an important consideration is whether the assumption of stationary light is valid. The $g^{(2)}$ measurements described in chapters 7 and 8 do not involve the correlation of temporally separate sections of the light pulse. It is therefore not significant that the light is in the form of a pulse since the intensity fluctuations which are being cross-correlated should in principle be identical.

When considering a quantised light field, the classical intensity \bar{I} must be replaced by the quantum intensity operator. It is then possible to show that $g^{(2)}$ can be written as [88]

$$g^{(2)}(\tau) = \frac{\langle n(n-1) \rangle}{\langle n \rangle^2} = \frac{(\Delta n)^2 - \langle n \rangle}{\langle n \rangle^2} + 1, \quad (4.5)$$

where $(\Delta n)^2$ is the variance of the photon number. In contrast to the possible values of $g^{(2)}(0)$ allowed by equation 4.3, its possible values now lie in the range $0 \leq g^{(2)}(\tau) \leq \infty$ [88]. Values of $g^{(2)}$ below 1 correspond to sub-Poissonian statistics and signify quantum states of light. For a (non-vacuum) number state equation 4.5 reduces to

$$g^{(2)}(\tau) = 1 - \frac{1}{n}. \quad (4.6)$$

It follows that for a single photon number state $g^{(2)} = 0$. In contrast it can be shown that for a coherent state $g^{(2)} = 1$ for all α [88].

In principal $g^{(2)}$ can be measured with a single detector as long as its temporal resolution is fast compared to the time-scale over which intensity fluctuations

are being investigated. The finite dead-time of the detector means that in general this requirement is not met. A solution to this problem is to use two detectors arranged in a Hanbury-Brown-Twiss configuration, as illustrated in 4.7.

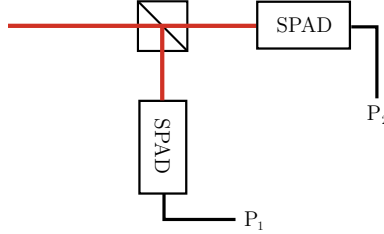


Figure 4.7: Hanbury Brown Twiss interferometer. A detector is placed at each output arm of a 50:50 beam splitter. In this experiment the photon counts, P_1 and P_2 , on single-photon counters (SPADs) are cross-correlated.

Labeling the output arms of the beamsplitter 1 and 2, $g^{(2)}$ can now be written

$$g^{(2)}(\tau) = \frac{\langle n_1(t)n_2(t+\tau) \rangle}{\langle n_1(t) \rangle \langle n_2(t) \rangle}. \quad (4.7)$$

In comparison with figure 4.7, n_1 and n_2 in equation 4.7 correspond to the photocount distributions P_1 and P_2 on single-photon detectors 1 and 2 respectively. In this experiment it is convenient to discretise the photocount distributions in time windows corresponding to the pulse repetition rate of the source. P_1 and P_2 therefore correspond to arrays of equal length, N , where each element is the number of photon counts recorded per experimental realisation. The Wiener-Khinchin theorem [92], which is analogous to the convolution theorem [93], provides a convenient way to calculate the cross-correlation between these two arrays. The required cross-correlation is reduced to a calculation of the Fourier transforms of the photocount signals P_1 and P_2 , and gives

$$g^{(2)}(\tau) = \frac{\mathcal{F}^{-1}(\mathcal{F}(P_1)\mathcal{F}^*(P_2))}{(\sum_N P_1 \sum_N P_2)/N}, \quad (4.8)$$

Equation 4.8 was used to calculate $g^{(2)}$ in this experiment.

It is important to consider the effect that a finite background signal has when

measuring $g^{(2)}$. In the presence of background light the value measured, $\tilde{g}^{(2)}(\tau)$, is given by [94]

$$\tilde{g}^{(2)}(\tau) = \left(1 + \frac{B}{S}\right)^{-2} (g^{(2)}(\tau) - 1) + 1, \quad (4.9)$$

where B/S is the ratio of the background light level to the true signal light being measured, and $g^{(2)}(\tau)$ is the value that would be measured in the absence of any background light. Note that it has been assumed that the background light is uncorrelated with the signal light, and that the background light has Poissonian photon statistics. The function given in equation 4.9 is plotted in figure 4.8 for a single photon signal, i.e. for $g^{(2)}(\tau) = 0$. It can be seen that even relatively small background light levels can significantly reduce the observed suppression in $g^{(2)}$. The values of $g^{(2)}$ presented in this thesis have been corrected for the finite background level against which measurements were performed.

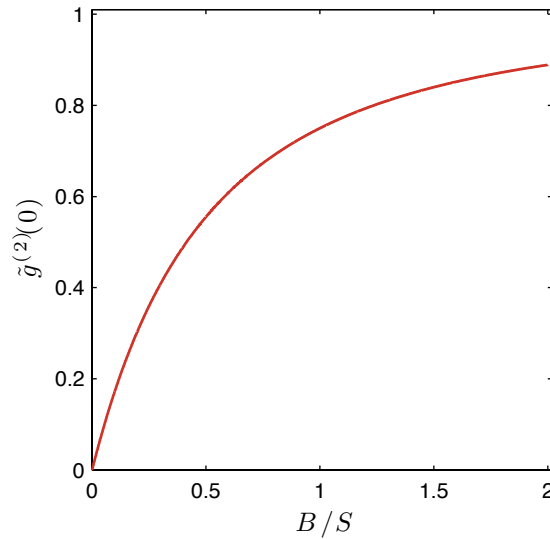


Figure 4.8: Variation of the measured value of the second order correlation function, $\tilde{g}^{(2)}(0)$, in the presence of a background signal. As the ratio of the background signal to the single photon signal increases, the observed suppression in $g^{(2)}(0)$ rapidly decreases.

Chapter 5

Microscopic dipole trap

In the previous chapter it was shown that approximately 2×10^5 atoms can be loaded into the MOT in 1 s giving a peak atomic density of the order $1 \times 10^{10} \text{ cm}^{-3}$. The peak density corresponds to an average interatomic spacing of roughly $3 \text{ }\mu\text{m}$. Since the waist of the probe beam is $1.2 \text{ }\mu\text{m}$, it is clear that the probe field overlaps very poorly with the atoms in the MOT. In order to maximise the coupling between the probe beam and the atomic sample, the spatial density distribution of the atoms needs to be more closely matched with the spatial mode of the probe beam. This requires strong spatial confinement of the atoms which is achieved using a red-detuned optical dipole trap. In this chapter the principles of forming an optical trap from a strongly focused laser beam will be discussed. The techniques used to align the trap with respect to the excitation beams and to characterise the properties of the trap are also given.

5.1 Theory

The key concepts of dipole trapping can be understood using the results of section 3.1, where the response of a two-level atom in a classical electromagnetic field was considered. The notation used below follows this section. Dipole potentials occur due to the dispersive atom-light interaction. The dipole potential, U , is given by [95]

$$U = -\frac{1}{2}\langle \text{Re}(\mathbf{d}) \cdot \mathbf{E} \rangle, \quad (5.1)$$

where the brackets represent a time average over the quickly oscillating electric field and dipole moment. The real part of the dipole moment is related to the real part of the susceptibility through equation 3.1. Taking the real part of the susceptibility from equation 3.5, in the limit of large detunings of the laser field it can be shown that the dipole potential is given by

$$U(\mathbf{r}) = \frac{3\pi c^2}{2\omega_{21}^3} \frac{\Gamma_{21}}{\Delta} I(\mathbf{r}). \quad (5.2)$$

Here $\Delta = \omega - \omega_{21}$ is the detuning of the trapping light from the atomic resonance frequency, where ω is the frequency of the trap light. The spatial variation of the dipole potential arises from its dependence on the local intensity $I(\mathbf{r})$. The gradient of the dipole potential results in a force on the atoms.

The associated scattering rate of the trap light is given by $\Gamma_{\text{scatt}} = \Gamma_{21}\rho_{22}$. The population of the excited state, ρ_{22} , can be found from the Liouville equation [65]. In the limit of large Δ it can then be shown that

$$\Gamma_{\text{scatt}}(\mathbf{r}) = \frac{3\pi c^2}{2\hbar\omega_{21}^3} \left(\frac{\Gamma_{21}}{\Delta}\right)^2 I(\mathbf{r}). \quad (5.3)$$

It can be seen that for a given intensity the dipole potential scales as $1/\Delta$, whereas the scattering rate scales as $1/\Delta^2$. Heating of atoms due to scattering of photons can therefore be made negligible using a far off-resonance trap [96]. The sign of the detuning determines whether atoms are trapped in the high intensity or low intensity region of the optical field. A red detuned trapping beam with a wavelength of 910 nm is used in this experiment. Atoms are therefore trapped in the high intensity region of the field. Note that the expressions above only apply when the rotating wave approximation is valid. When calculating the properties of the dipole trap used in this experiment the rotating wave approximation was not taken since the light field is far-detuned from the atomic transition frequency.

For a multi-level atom such as Rb the principles of dipole trapping described above still hold. However, the dipole potential becomes state dependent [95].

With a red-detuned trap, the common way to form a minimum in the dipole potential is to focus the trapping beam. For a Gaussian trapping beam propagating along z , the resulting potential is of the form [97]

$$U(r, z) = U_0 \frac{w_0^2}{w^2(z)} \exp\left(\frac{-2r^2}{w^2(z)}\right), \quad (5.4)$$

where the $1/e^2$ radius of the beam is given by

$$w(z) = w_0 \sqrt{1 + \left(\frac{z}{z_R}\right)^2}, \quad (5.5)$$

and the trap depth, U_0 , in this work can be found from

$$U_0 = \frac{3\pi c^2}{2} \left(\frac{1}{3} \frac{\Gamma_{D1}}{\omega_{D1}^3 \Delta_{D1}} + \frac{2}{3} \frac{\Gamma_{D2}}{\omega_{D2}^3 \Delta_{D2}} \right) \times \frac{2P}{\pi w_0^2}. \quad (5.6)$$

Here w_0 is the waist of the trapping beam, z_R is its Rayleigh range, P is the power of the beam, and $\Delta_{D1,D2}$ refer to the detuning of the trap light from the D1 and D2 resonance frequencies, $\omega_{D1,D2}$, respectively. For the trap wavelength used in the following experiments the contribution of both the D1 and D2 lines must be taken into account to obtain accurate estimates of the properties of the trap.

An important property of the trapped atomic cloud is its size. The size of a thermal cloud in a harmonic trapping potential is related to its temperature, T , according to [95]

$$\sigma_r = \sqrt{\frac{k_B T w_0^2}{4U_0}}, \quad (5.7)$$

and,

$$\sigma_z = \sqrt{\frac{k_B T z_R^2}{2U_0}}. \quad (5.8)$$

Here σ_i is the standard deviation of the Gaussian density distribution in direction i , and m is the mass of the ^{87}Rb atom. The harmonic potential is a suitable approximation to the Gaussian potential in equation 5.4 provided

that $k_B T \ll U_0$ [95]. The dependence of the size of the cloud on the waist of the trapping beam highlights the necessity of tight focusing in this work.

5.2 Trap loading and optimisation

The optimum experimental parameters for loading the MOT, discussed in section 4.2.2, do not necessarily correspond to the optimum conditions for loading atoms into the dipole trap. To maximise the optical depth of the atomic cloud its density needs to be maximised. It is therefore important to load as many atoms as possible from the MOT into the dipole trap, whilst keeping the temperature of the cloud as low as possible. As will be discussed in this section, the number of atoms loaded into the dipole trap is limited by the small waist of the trapping beam and the low density of the MOT. A description of the home-built laser system which provides the light for the dipole trap can be found in section A.1.

5.2.1 Rough alignment

As mentioned previously it is desirable to match the cloud size with the waist of the probe beam to achieve strong atom-light coupling. Equations 5.7 and 5.8 provide an estimate of the size of an atomic cloud in a dipole trap of waist w_0 , at a temperature T . Assuming a trap depth of 0.6 mK and an atom temperature of 0.1 mK, a trap beam with a waist of $5 \mu\text{m}$ gives a cloud with $\sigma_r = 1 \mu\text{m}$ and $\sigma_z = 25 \mu\text{m}$. The radial extent of the cloud is comparable to the waist of the probe beam in this case. A waist of around $5 \mu\text{m}$ for the trapping beam is therefore required in this experiment. However, overlapping the co-propagating probe and dipole trap beams which both have microscopic waists is challenging.

The initial alignment of the beams proceeded as follows. The probe beam was aligned through the aspheric lens pair in the vacuum chamber using methods described in [47]. The alignment procedure involved setting the spot size on the input aspheric lens to give the desired beam waist, whilst also adjusting the convergence of the incoming beam so that it matched the divergence of the outgoing beam. Matching the convergence of the incoming

and outgoing probe beam allowed the position of its focus to be centered between the lenses.

The next step was to align the dipole trap beam such that it overlapped the probe beam. The dipole trap beam originates from a separate optical fiber to the probe beam, as shown in figure 4.1. The two beams are combined on a dichroic mirror before entering the vacuum chamber and passing through the aspheric lenses. The beams were overlapped radially to within several microns by imaging them at two positions separated by a distance of approximately 5 m. However overlapping the foci of the beams longitudinally was more difficult since the beams could not be imaged in the focal plane. The desired waist of $5 \mu\text{m}$ for the dipole trap beam constrains its spot size on the input aspheric lens. The main method of tuning the longitudinal position of the focus of a beam is to change its convergence on the input lens. However, for a fixed distance between the source and the lens, changing the beam convergence also changes its spot size on the lens. This results in a variation of the focused beam waist. Zemax software was used to study the interdependence of the beam properties. The variation of the effective focal

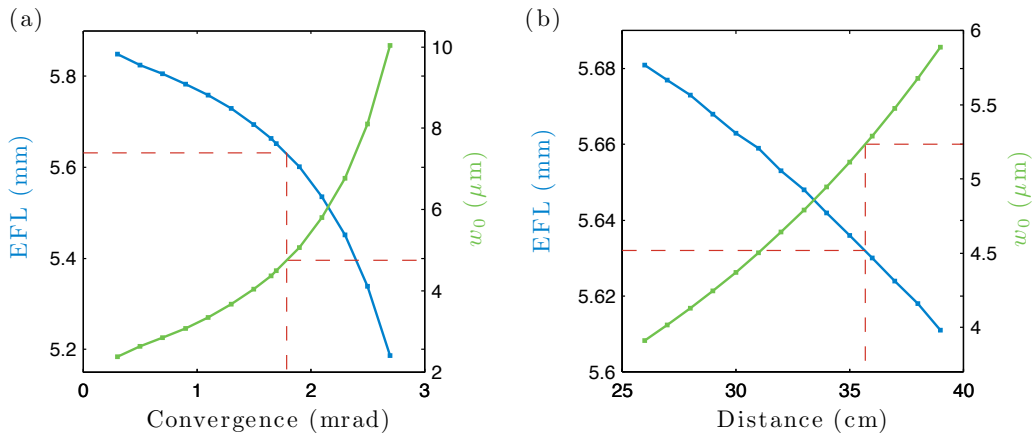


Figure 5.1: Zemax calculations to determine the sensitivity of the effective focal length (EFL) of the input aspheric lens on the properties of the input beam. (a) Dependence of the EFL and waist of the focused beam on the convergence of the incoming beam. The distance between the source and input aspheric lens is fixed. (b) Dependence on the distance between the source and the input aspheric lens for a fixed convergence of the input beam.

length (EFL) and the waist of the dipole trap light with beam convergence is illustrated in figure 5.1 (a). Note that the distance between the source of the dipole trap light and the input aspheric lens is fixed. For changes in the beam convergence of only 1 mrad, the EFL can be scanned over a distance of over 200 μm . The EFL is less sensitive to changes in the distance between the source and the input aspheric lens for a fixed beam convergence. This is shown in figure 5.1 (b). For example, a change in the EFL of 100 μm is only possible when displacing the source by more than 15 cm. The red dashed lines in figure 5.1 show the convergence and source to lens distance required to obtain an EFL matching that of the probe beam, along with the resulting trap waist. Using the values predicted by Zemax, the beam convergence and the source to lens distance were set to roughly overlap the beams. Given the measured convergence of the beam and its estimated spot size on the input aspheric lens, the waist of the dipole trap beam is estimated to be $5.1 \pm 0.2 \mu\text{m}$. Note that this value applies after the fine alignment of the dipole trap beam described later in section 5.2.3.

5.2.2 Trap loading

Following the rough alignment of the trap beam, the loading of atoms into the dipole trap from the MOT is studied. The timing sequence for loading the dipole trap is shown in figure 5.2. The MOT is first loaded, followed by a molasses stage. The dipole trap light is turned on part way through the MOT load stage. As will be discussed shortly, having the dipole trap on permanently while loading the MOT is detrimental. Following the molasses stage there is a depump period where the repump light is extinguished. The depump stage pumps atoms into the $5s^2S_{1/2}(F = 1)$ ground state. This has been shown to be an important step when loading dipole traps as it suppresses atom loss mechanisms such as hyperfine changing collisions and light-assisted collisions [98]. The atoms are later repumped into the $5s^2S_{1/2}(F = 2)$ state in preparation for excitation by the probe beam. This is done with repump light originating from the same optical fiber as the probe beam. The stages labeled “hold” ensure that mechanical shutters used to block certain beams have sufficient time to open/close. Note that the quadrupole coils for the

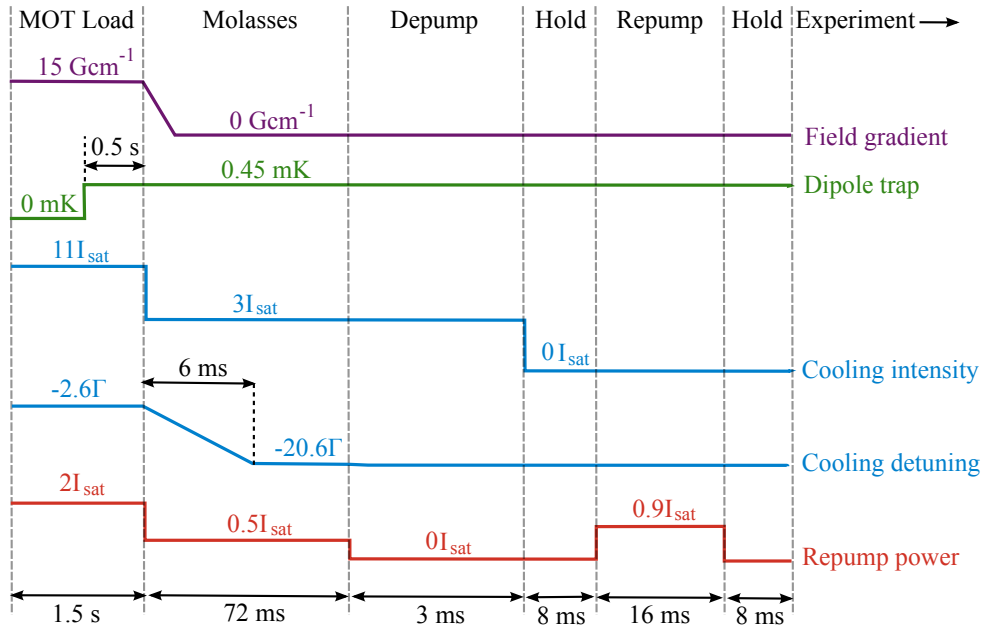


Figure 5.2: Timing sequence for loading the dipole trap. The MOT loading and molasses stages are followed by a depump period where atoms are pumped into the ground state. The atoms are later repumped ready for probe excitation.

MOT are turned off slowly (over a few ms) at the beginning of the molasses stage. This is done to avoid vibrations arising from movement of the coils as the current through them is switched. When current runs through the MOT coils they experience an attractive force which flexes the structure in which they are mounted.

The atoms in the dipole trap are imaged using methods similar to those described for the MOT in section 4.2. Following a time of flight period of $10 \mu\text{s}$ where the atoms are released from the trap, the MOT beams are turned on. The on-axis fluorescence from the atoms is then collected onto a SPAD. An example of the fluorescence signal obtained can be seen in figure 5.7 (b). The photon count on the SPAD is converted into an atom number using the estimated detection efficiencies and scattering rate of the imaging light. Due to the small numbers of atoms loaded into the trap it was not possible to collect sufficient off-axis fluorescence to image the cloud on a CCD camera. Note that the loading of the dipole trap was optimised for a cross-trap configuration as this was the arrangement originally planned (see

appendix A.2). However, the optimum parameters for loading of the axial trap only were found to be roughly the same.

The experimental parameters during the molasses stage were optimised to maximise the number of atoms loaded into the crossed dipole trap. The loading is not improved by adjusting the experimental parameters during the MOT load stage. This is presumably because optimal MOT loading

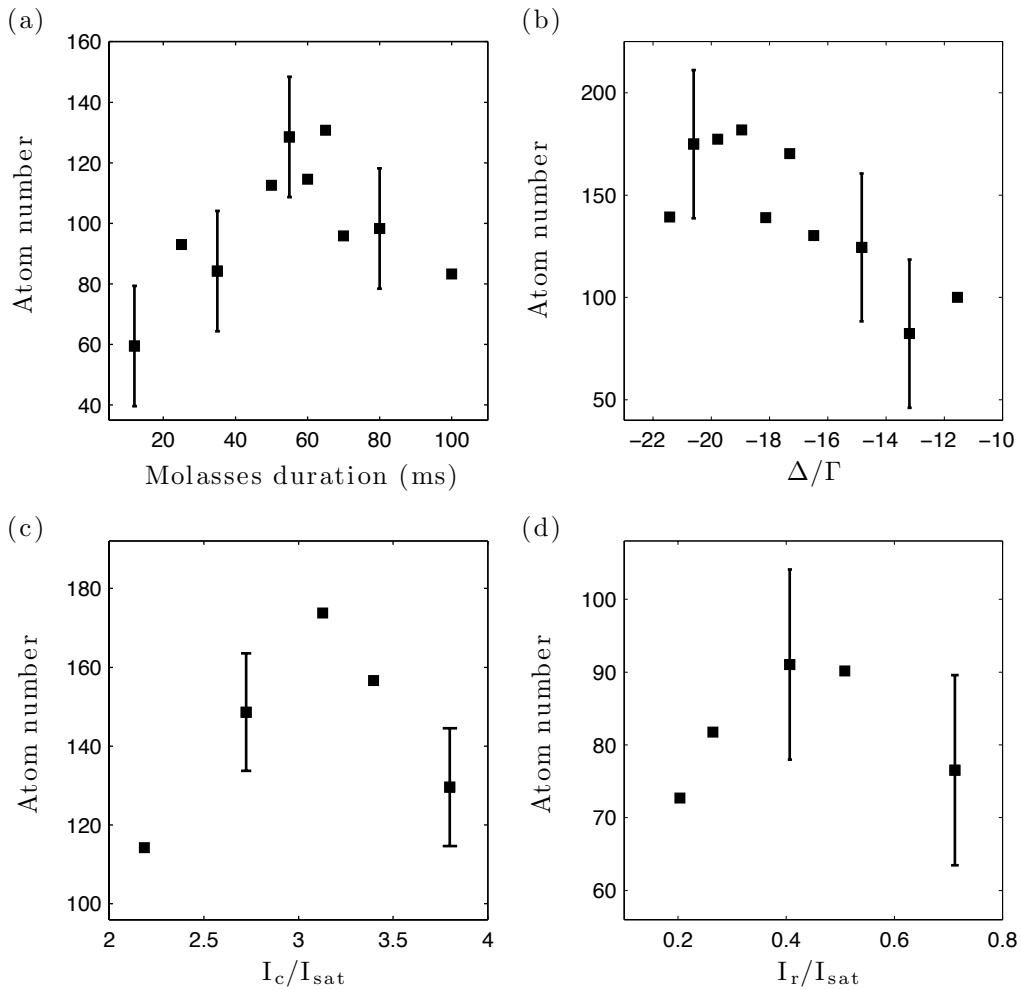


Figure 5.3: Optimising the number of atoms loaded into the crossed dipole trap. The atom number in the dipole trap is studied as a function of various experimental parameters during the molasses stage. (a) Dependence on the duration of the molasses phase. (b) Dependence on the detuning of the cooling light, Δ . (c) Dependence on the intensity of the cooling light. (d) Dependence on the intensity of the repump light.

gives the best starting point for loading the dipole trap. Studies of the dipole trap loading are illustrated in figure 5.3. It can be seen that the optimum molasses duration is around 60 ms. This is much longer than the molasses duration required to minimise the atom temperature in the MOT. The increased duration could reflect the time scale over which atoms are transferred from the MOT into the dipole trap. It can also be seen that the cooling light needs to be much further detuned to maximise the atom number compared with when loading the MOT. This is probably due to the fact that light assisted collisions are suppressed at these large detunings [98]. The sensitivity of the atom number on the intensity of the cooling light also reflects this. Sufficient cooling light is required for efficient cooling of the atoms into the trap, but high cooling intensities increase the loss rate [98].

It is also important to consider the optimum time during the experimental cycle at which to turn the dipole trap on. In figure 5.4 (a) the atom number in the dipole trap is studied as a function of its overlap time with the MOT. The duration of the MOT load prior to the trap beam being turned on is

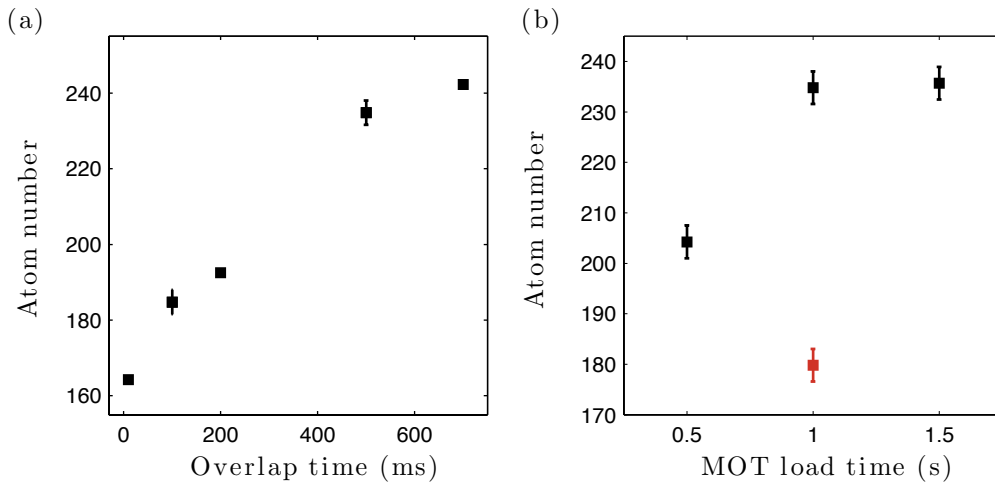


Figure 5.4: Dependence of atom number in the dipole trap on its overlap time with the MOT loading stage. (a) Effect of changing the overlap time of the dipole trap and MOT following a fixed MOT load time of 1 s. (b) Effect of changing the MOT load time preceding a fixed overlap time of 500 ms with the dipole trap. The red data point corresponds to the case where the dipole trap is on permanently i.e. during the entire MOT load.

fixed at 1 s. It can be seen that the atom number increases with the overlap time. For overlap times beyond 500 ms the atom number does not increase significantly. In figure 5.4 (b) the variation of the atom number as a function of the MOT load time is plotted. Following the MOT load there is a period of 500 ms where the dipole trap is overlapped with the MOT. Despite the fact that the atom number in the MOT saturates after a loading time of roughly 6 s, extending the MOT load time beyond 1 s does not lead to an increase in the number of dipole trapped atoms. This is probably because the density of the atoms in the region of the dipole trap does not increase beyond this time. Turning the dipole trap on during the entire MOT load (red data point) significantly reduces the number of atoms loaded. This is probably because the Stark shifts produced by the trap light interfere with laser cooling in the MOT. Alternation of the MOT and dipole trap beams could potentially improve the trap loading [99].

Over 200 atoms can be loaded into the crossed-dipole trap. The number of atoms that can be loaded into the axial trap alone with the same experimental parameters is roughly 50% of the cross-trap number. Therefore there are typically around 100 atoms loaded into the axial dipole trap. Due to systematic errors the fractional uncertainty on the atom number in the data presented is approximately 50%. In addition it can be seen that the statistical uncertainty on the atom numbers is large. The large fluctuations in the number of atoms loaded into the dipole trap is attributed to instability of the MOT. In chapter 4.2 it was pointed out that the planar MOT beams create an interference pattern due to the small angle at which they intersect. As a result, the atom cloud moves as it follows the fringes of high intensity. If the waist of the dipole trap beam happens to be in a low intensity fringe, it can be expected that the efficiency of dipole trap loading is reduced.

The number of atoms loaded into the dipole trap is probably limited by the density of the cloud in the MOT. The small waist of the dipole trap beam means that there is poor overlap with the density distribution of the MOT. In principle compression of the cloud could be achieved by increasing the gradient of the quadrupole field [100]. However, this was not feasible in the current experiment as the electrical currents required for a compressed MOT phase were too high.

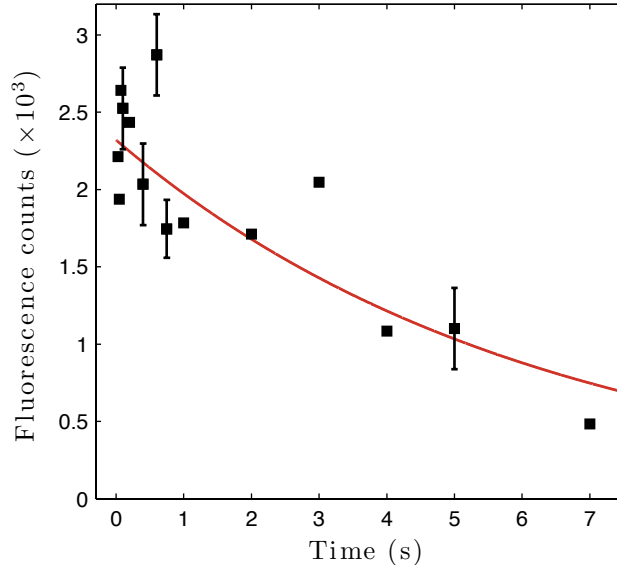


Figure 5.5: Lifetime of atoms in the dipole trap. From the fit the $1/e$ lifetime is 6 ± 1 s.

The lifetime of the atoms in the dipole trap was measured by varying the time for which they were held before imaging. The lifetime curve is shown in figure 5.5. The data has been fit assuming an exponential decay giving a $1/e$ lifetime of 6 ± 1 s. The trap lifetime is much longer than the time scales over which experiments are performed.

5.2.3 Fine alignment

The rough alignment of the probe and dipole trap beams discussed in section 5.2.1 provides a starting point for more precise overlap of the beams. An atomic signal is used to give a more precise measure of their alignment. The absorption of the probe beam by the atomic cloud is the quantity of most interest, since this provides a measure of the optical depth of the medium. In section 3.2.2 the importance of achieving a high optical depth for efficient photon storage was discussed.

An electron-multiplying CCD camera was used to image the dipole trapped atoms. Fluorescence was collected along the aspheric lens axis of the vacuum chamber (see figure 4.1). Figure 5.6 shows an image of the MOT and the dipole trap taken using the CCD camera. The probe beam was overlapped

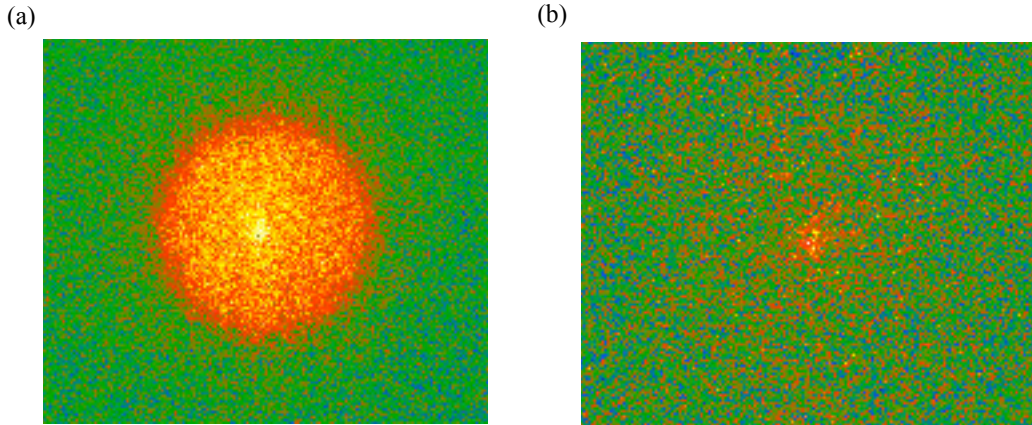


Figure 5.6: (a) Fluorescence from atoms in the MOT. (b) Fluorescence from atoms in the dipole trap. In both cases the fluorescence is collected along the aspheric lens axis.

with the fluorescence signal from the dipole trapped atoms, providing a further diagnostic of the radial alignment of the trap and probe beams.

Initially there was no evidence of absorption of the probe beam by the dipole trapped atoms. It was therefore difficult to use this as a diagnostic of the beam overlap. Since a fluorescence signal from the atoms was available, another diagnostic was developed to exploit this. The method involves imaging the atoms without any repump light. Recall that after the depumping stage the atoms are in the $F = 1$ ground state. Repump light originating from the same optical fiber as the probe beam is then applied, pumping atoms into the $F = 2$ ground state. Applying imaging light without any repump light means that only the atoms which have been repumped fluoresce. The amount of fluorescence obtained relative to the case where the atoms are imaged *with* repump light therefore gives a diagnostic of the beam overlap. The level scheme for the sequence is shown in figure 5.7 (a). The alignment of the trap and probe beams is adjusted to maximise the fluorescence signal. This is done using successively smaller repump intensities to increase the sensitivity of the method. An example of the fluorescence signal obtained on a SPAD is shown in figure 5.7 (b). Note that the atoms are imaged in free-flight. The decay in the fluorescence signal with imaging time occurs as atoms move out of the aspheric lens axis. Figure 5.7 (c) illustrates the method used to con-

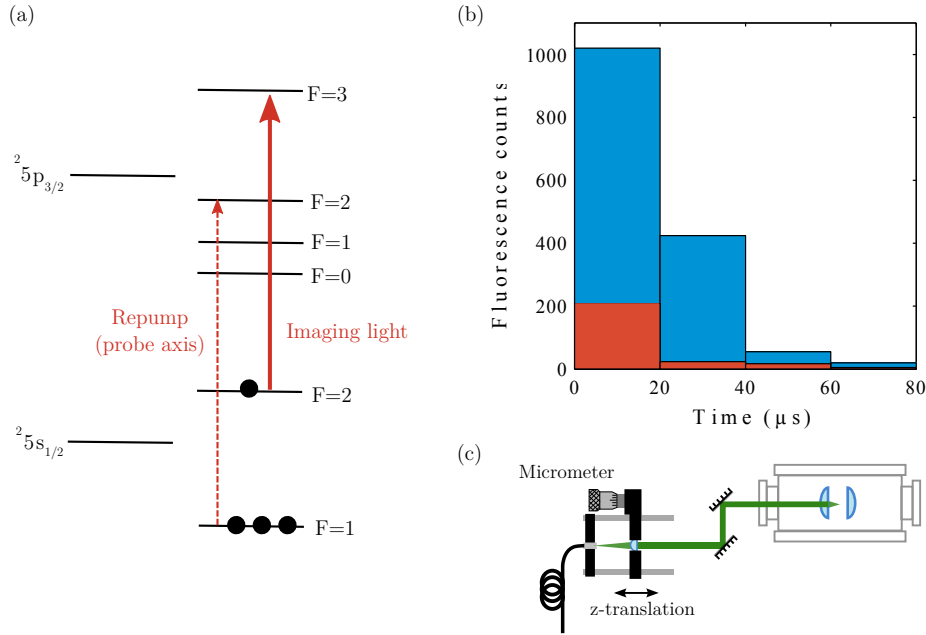


Figure 5.7: Fluorescence signal as a diagnostic of dipole trap alignment. (a) Repump light originating from the probe fiber is used to pump atoms from the $F = 1$ ground state into the $F = 2$ ground state. The atoms are then imaged without any repump light. (b) Fluorescence signal collected on a SPAD for the case where the atoms are imaged with (blue) and without (red) repump light. The non-zero fluorescence signal when the atoms are imaged without repump light comes from atoms repumped prior to imaging. (c) Cage system used to weakly focus and align the dipole trap beam. The convergence of the beam can be varied with micrometer adjustment of the position of the focusing lens.

control the alignment of the dipole trap beam. The trap light originates from an optical fiber and is weakly focused by an aspheric lens housed in a cage mount. A micrometer adjustment allows the position of the focusing lens, and hence the beam convergence to be precisely varied. Changing the beam convergence varies the longitudinal position of the trap waist. Two mirrors after the cage mount allow the beam to be aligned through the aspheric lens pair in the vacuum chamber.

After following the procedures described above, a small probe absorption signal was visible. To optimise this signal, the longitudinal position of the dipole trap was varied by changing its beam convergence. The variation of probe absorption with the position of the dipole trap focusing lens is

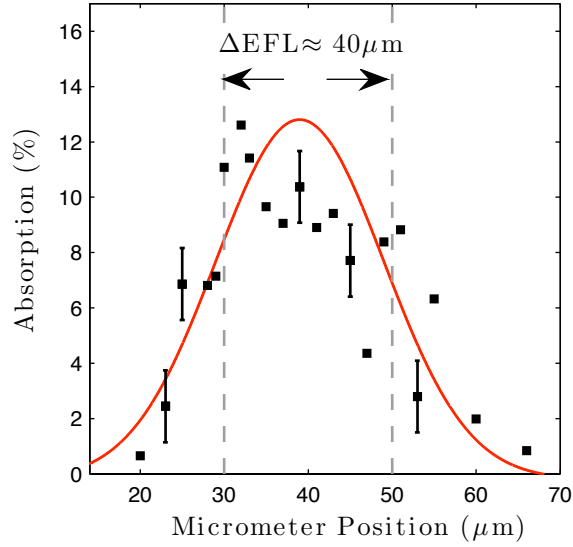


Figure 5.8: Variation in probe absorption with position of dipole trap focusing lens. The red curve is a guide to the eye (Gaussian with standard deviation $10 \mu\text{m}$). From the measured dipole trap beam convergences at the two marked positions (dashed lines), Zemax was used to estimate the corresponding EFL of the focused spot inside the vacuum chamber. The change in beam convergence of roughly 0.18 mrad between the two points translates to a change in the EFL of approximately $40 \mu\text{m}$.

plotted in figure 5.8. Note that to avoid inhomogeneous Stark shifts, the atoms were released from the trap when measuring the probe absorption. However, the probe absorption signal decays very rapidly (see figure 5.11) as the atoms move out of the probe beam. As a result the absorption signal cannot be optimised in real-time. It is necessary to perform many cycles of the experiment to obtain a signal with a reasonable signal to noise level.

It can be seen that the maximum level of absorption of the probe beam is only around 10 %. To improve the probe absorption a method of real-time optimisation is required.

5.3 Trap modulation

It is desirable to perform experiments when the atoms have been released from the dipole trap. As mentioned in the previous section, the trap causes

broadening of the atomic transition lineshapes since atoms experience a position dependent Stark shift (see section A.3). The centers of the lineshapes are also strongly shifted. However since the waist of the probe beam is very small, when the atoms are released from the trap they leave the excitation region very quickly. In order to increase the experimental integration time per shot, the trap is rapidly modulated between an off-state and an on-state, similar to the procedure demonstrated in [101]. Experiments are performed during the trap-off states where the trapping light has been mostly extinguished. When the dipole trap light comes back on the atoms are then re-trapped. The use of bottle beam traps using blue-detuned trapping light can provide an alternative to releasing the atoms from the trap [102].

5.3.1 Sequence

A schematic of a typical trap modulation sequence is shown in figure 5.9 (a). For probe absorption measurements, the probe light comes on during the periods where the dipole trap is off. Experimental data is post-processed

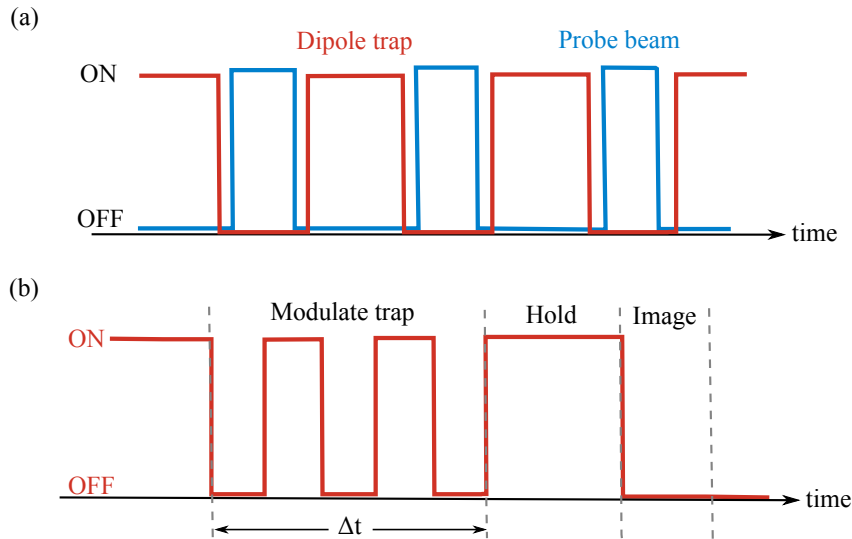


Figure 5.9: Dipole trap modulation sequences. (a) For probe absorption measurements the power of the dipole trap is modulated out of phase with the power of the probe beam. (b) Sequence used to measure losses associated with modulating the dipole trap.

so that only photon counts during the trap-off periods are counted. This is necessary since a small fraction of the dipole trap light reaches the SPADs.

The sequence used to study the losses associated with modulating the dipole trap is shown in figure 5.9 (b). The trap is modulated for a period of time before turning it back on for a few ms. During this “hold” time atoms which are no longer trapped leave the imaging region. The MOT beams are then turned on and fluorescence from the atoms is collected on a SPAD. In figure 5.10 (a) fluorescence counts from the atoms are plotted as a function of the trap modulation frequency. The trap is modulated for a duration of 1 ms. The modulation frequency must be high enough such that atoms do not leave the trapping region during the trap-off period. It can be seen that for trap frequencies below around 60 kHz a large fraction of the atoms are lost during the trap modulation period. Choosing a trap modulation frequency is a compromise between the atom loss observed at low frequencies, and the smaller time available during the trap-off period to do experiments at high modulation frequencies. The fluorescence counts from the atoms as a

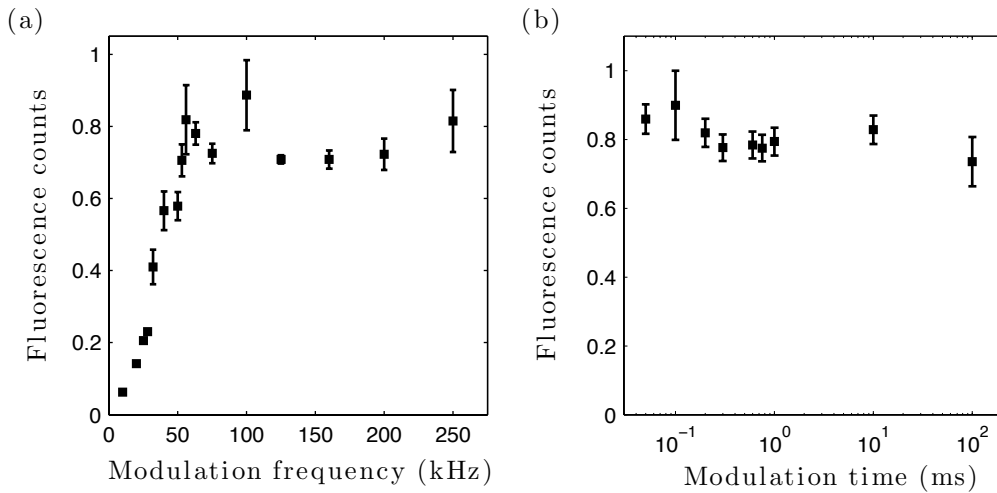


Figure 5.10: Characterising the loss of atoms when modulating the dipole trap. (a) Fluorescence signal from the atoms as a function of the trap modulation frequency for a fixed modulation duration of 1 ms. (b) Variation of the fluorescence signal with duration of trap modulation stage for a fixed modulation frequency of 200 kHz. The fluorescence signals are normalised to the case where no trap modulation occurs.

function of modulation time at a fixed trap modulation frequency of 200 kHz is plotted in figure 5.10 (b). It can be seen that even after 100 ms the fluorescence signal remains largely unchanged.

5.3.2 Probe absorption

The variation in probe absorption with trap modulation time will now be compared to the case where the atoms are released from the dipole trap completely. The results are shown in figure 5.11. The trap modulation period is $6 \mu\text{s}$, corresponding to a frequency of roughly 167 kHz. These trap modulation parameters are used throughout the remainder of this thesis. When releasing the atoms from the dipole trap (black data points) the probe absorption halves after roughly $30 \mu\text{s}$. The time over which experiments can be performed before the probe absorption begins to drop and the dipole trap must be re-loaded is on the order of $10 \mu\text{s}$. However, when modulating the

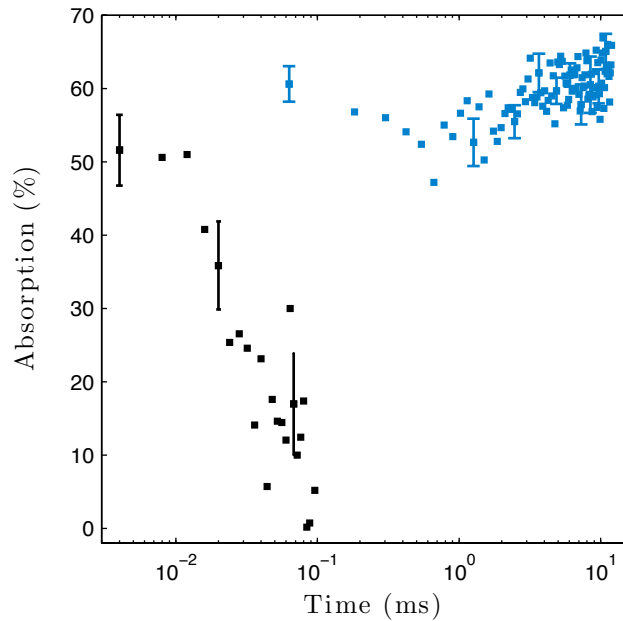


Figure 5.11: Comparison of absorption signal when the dipole trap is turned off completely (black points), with the absorption signal when the dipole trap is modulated (blue points). When the trap is turned off the probe absorption signal vanishes after roughly 0.1 ms. However when the dipole trap is modulated the absorption signal remains roughly constant over tens of ms.

dipole trap (blue data points) the probe absorption is constant over tens of ms. Therefore over three orders of magnitude more signal can be obtained per experimental cycle using the trap modulation technique. The variation of probe absorption with trap modulation time is strongly dependent on the power of the probe field. This is discussed in the next section. Note that the increase in the probe absorption relative to the values in figure 5.8 is due to an improvement in the trap alignment and its loading. These improvements were made as a result of real-time optimisation of the probe absorption signal, made possible by the trap modulation technique.

To maximise the coupling of the probe beam to the medium the atoms can be optically pumped into the $5s^2S_{1/2}(F = 2, m_F = 2)$ state. However, obtaining a diagnostic of the effectiveness of the optical pumping is difficult in this experiment. A standard method of measuring the fraction of optically pumped atoms is to magnetically trap them in the quadrupole field used for the MOT [47]. However, the maximum magnetic field gradient that can be generated in this experiment is roughly equal to the minimum value required to magnetically trap the atoms. In addition, it is not known whether the dipole trap is overlapped with the center of the quadrupole trap. Therefore

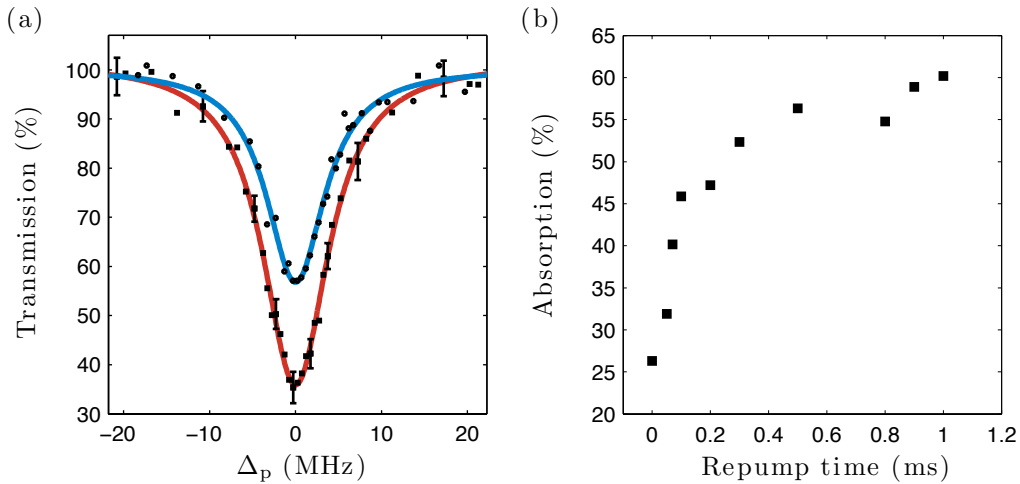


Figure 5.12: Probe absorption as a function of repumping parameters. (a) Probe absorption spectra for a quantisation field of 1 G (red) and with no quantisation field (blue). (b) Variation in probe absorption with duration of the repumping stage.

loading the magnetic trap is very difficult.

Given the optimised alignment of the dipole trap and probe beams, it is necessary to consider what other experimental parameters can be varied to maximise the optical depth of the medium. One stage of the experiment to consider is the repump period (see figure 5.2), which pumps atoms into the $5s^2S_{1/2}(F = 2)$ state prior to probe excitation. In figure 5.12 (a) probe absorption spectra are compared with and without an applied quantisation axis. The quantisation axis is turned on just before the repump stage and remains on for the rest of the experimental cycle. It can be seen that application of the quantisation axis leads to a significant increase in probe absorption. The increase is most likely due to optical pumping by the repump beam. In figure 5.12 (b) the probe absorption on resonance is plotted as a function of the duration of the repump stage. After a repump time of roughly 1 ms the probe absorption signal saturates. It can be seen that even when no repump light is applied there is some absorption ($\approx 25\%$). This suggests that the atoms aren't completely depumped prior to the repump stage.

An additional experimental parameter to consider is the depth of the dipole trap. Increasing the trap depth should lead to an increase in the loading rate of atoms [98]. However, the temperature of the atoms is also expected to

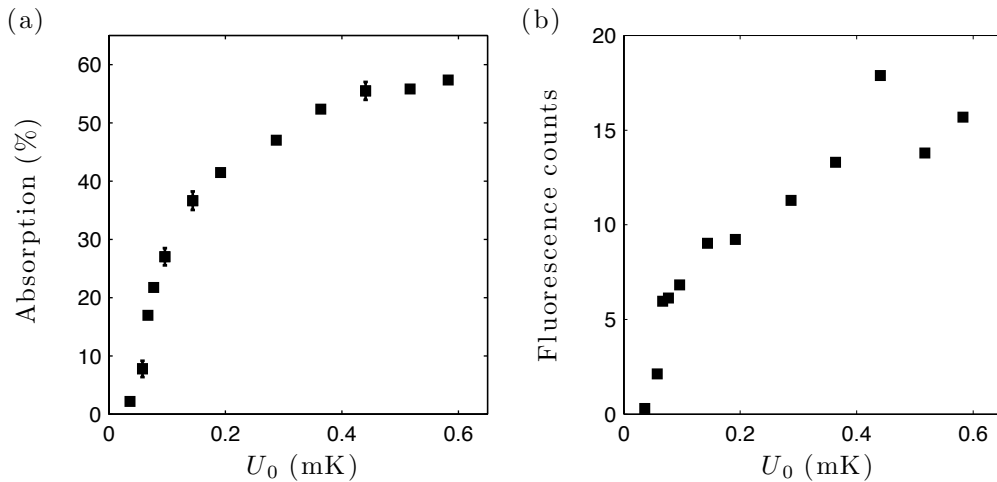


Figure 5.13: Probe absorption and fluorescence signal as a function of dipole trap depth. (a) Variation of probe absorption. (b) Variation of fluorescence signal from the atoms.

increase [98]. The variation of probe absorption with the depth of the dipole trap is plotted in figure 5.13 (a). The probe absorption initially increases very rapidly with trap depth before approaching saturation. In figure 5.13 (b) it can be seen that the corresponding fluorescence signal from the atoms also increases with trap depth. The increased absorption can therefore be attributed to an increase in the number of trapped atoms.

All of the experiments that will be discussed in the remainder of this thesis have been performed with a trap depth of roughly 0.45 mK unless stated otherwise.

5.3.3 Loss

The absorption of the probe beam as a function of the dipole trap modulation time shown in figure 5.11 was for a weak probe of approximately 1 pW, corresponding to $\approx 0.03I_{\text{sat}}$. For higher probe powers the absorption signal decays at a much faster rate. This is illustrated in figure 5.14, where the decay in absorption is shown for different probe powers. The decay in absorption occurs due to atom loss from the dipole trap, induced by the probe light. To escape from the trap an atoms total energy, i.e. kinetic plus potential, must exceed the trap depth. The decrease in atom number can be considered in terms of a density dependent loss and a density independent loss [103]. Possible mechanisms for density dependent loss include light-assisted collisions between atom-pairs in opposite parity states [104]. The density independent loss occurs due to radiative heating of individual atoms by the probe beam. The atom loss rate can be written as [98, 103]

$$\frac{dN(t)}{dt} = -\Gamma N(t) - \beta \frac{N(t)(N(t) - 1)}{2}. \quad (5.9)$$

Here N is the number of atoms, Γ is the one-body loss coefficient, and β is the two-body loss coefficient. The second term in equation 5.9 can give rise to very fast loss rates at short times. For now the second term will be ignored giving

$$N(t) = N_0 \exp(-\Gamma t), \quad (5.10)$$

where N_0 is the initial atom number.

In order to fit this function to the data in figure 5.14 it is assumed that the probe absorption is proportional to the atom number. From the fits to the experimental data, it is observed that the decay in probe absorption is reasonably well described by equation 5.10 at probe powers below around 17 pW. At higher probe powers the decay is much faster at short modulation times, as shown in the inset to figure 5.14 (c). The faster decay probably signifies the onset of density dependent losses. The one-body loss coefficient,

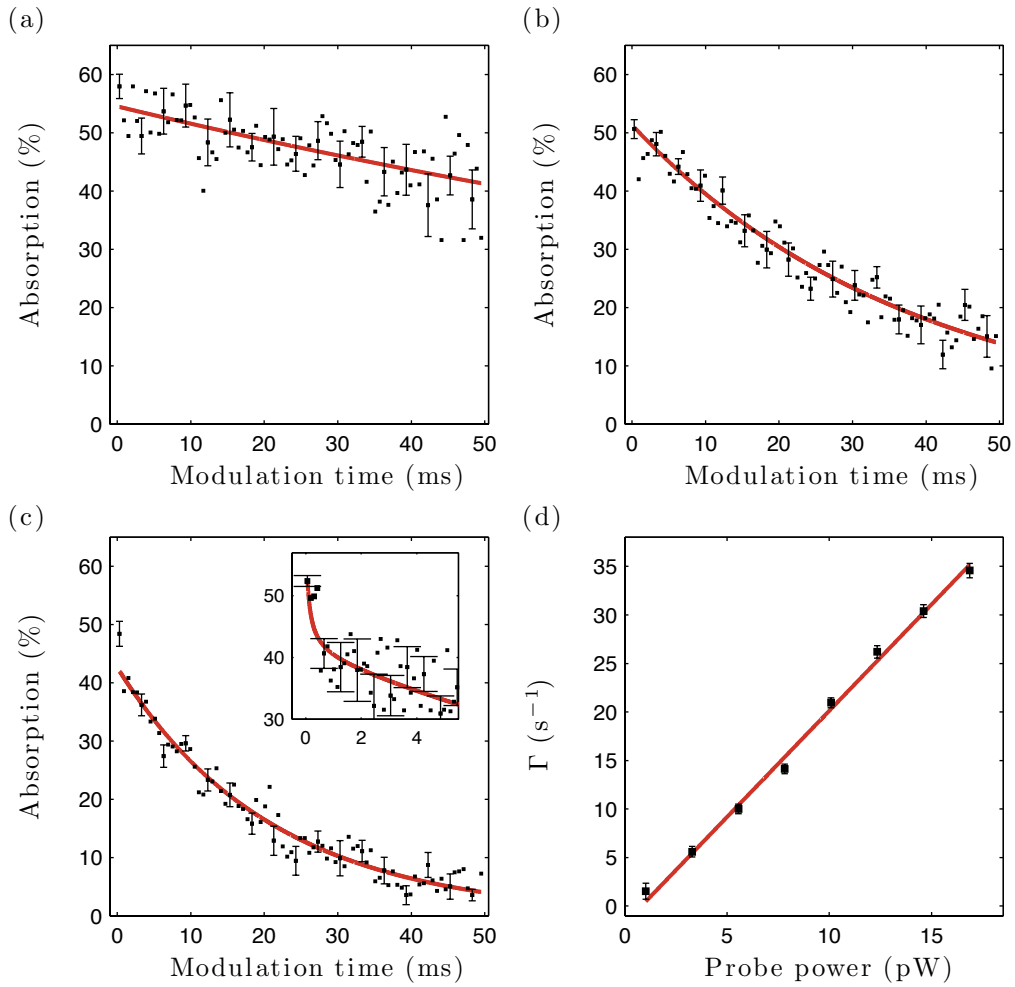


Figure 5.14: Decay in probe absorption signal over trap modulation time due to atom loss from the dipole trap. (a) Probe power of 3.3 pW ($0.087I_{\text{sat}}$). (b) Probe power of 12 pW ($0.32I_{\text{sat}}$). (c) Probe power of 21 pW ($0.56I_{\text{sat}}$). Inset: The short time behavior shows evidence of density dependent losses. (d) One-body loss coefficient, Γ , as a function of probe power.

Γ , has been extracted from the loss curves at different probe powers and is shown in figure 5.14 (d). The one-body loss coefficient varies approximately linearly over the range of probe powers shown.

An alternative explanation for the decay in probe absorption could be depumping of the atoms caused by the probe light. Since no repump light is applied during probe excitation it is possible that the atoms are depumped into the ground hyperfine state where the probe beam is no longer resonant. To verify that atom loss is in fact responsible for the decay in the absorption signal, the fluorescence from the atoms after a variable period of probe excitation was studied (using a sequence similar to 5.9 (b)). The fluorescence signal is shown in figure 5.15, where the signal has been normalised to the case where no trap modulation or probe excitation occurs. A decay in the fluorescence signal is observed showing that there is a decay in the atom number remaining in the trap after the probe excitation period. If the atoms were simply depumped, and not expelled from the trap, the fluorescence signal would not decay significantly over the short time scales plotted. The

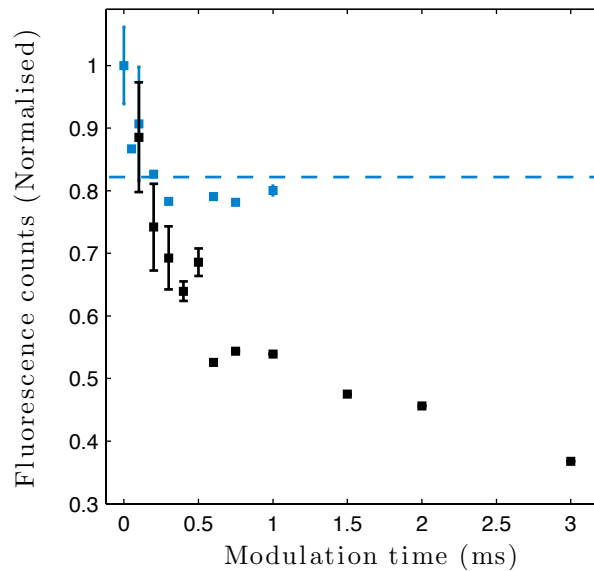


Figure 5.15: Fluorescence signal from atoms as a function of dipole trap modulation time when applying a probe beam (black), and when no probe beam is applied (blue). The black data points are for a probe power of roughly 20 pW. The dotted line is the approximate long-time (10 ms-100 ms) fluorescence signal in the absence of probe light.

fluorescence signal also provides further evidence of density dependent loss at short modulation times where there is a more rapid decay in the signal. The time scale of around 0.5 ms of this decay is similar to that shown in the inset of figure 5.14 (c).

5.4 Atom temperature

There are several methods available to measure the temperature of the atoms in the dipole trap. A time of flight measurement, which was used to measure the atom temperature in the MOT, could be performed. Alternatively given the waist of the trapping beam and the trap depth, the temperature can be inferred from the spatial extent of the trapped cloud using equations 5.7 and 5.8. Both of these methods require direct imaging of the atomic cloud which is difficult in this experiment due to the small atom number in the dipole trap. As mentioned previously it is only possible to collect fluorescence from the atoms using the aspheric lenses in the vacuum chamber.

The “release and recapture” technique [105] of measuring atom temperatures involves releasing the atomic cloud from the dipole trap for a period of time, before recapturing a fraction of the atoms by turning the dipole trap back on. The release and recapture procedure is illustrated in figure 5.16 (a). After preparing the atoms in the dipole trap, the trap is turned off for a time Δt . The trap is then turned back on for 50 ms and fluorescence from the re-captured atoms is collected on a SPAD. Figure 5.16 (b) illustrates the principle of the measurement. Following its release, an atom with kinetic energy, K , moves in free-space by a distance which depends on its velocity, and the release time. When the dipole trap is turned back on the atom experiences a potential, U , at its new position. Only atoms whose total energy, $E = U + K$, is less than the trap depth can be recaptured. Increasing the time the dipole trap is turned off results in fewer re-captured atoms and therefore a smaller fluorescence signal.

The variation of the recaptured fraction of atoms with release time allows the temperature of the atomic cloud to be determined. In order to extract the temperature a Monte-Carlo model is used to simulate the release and

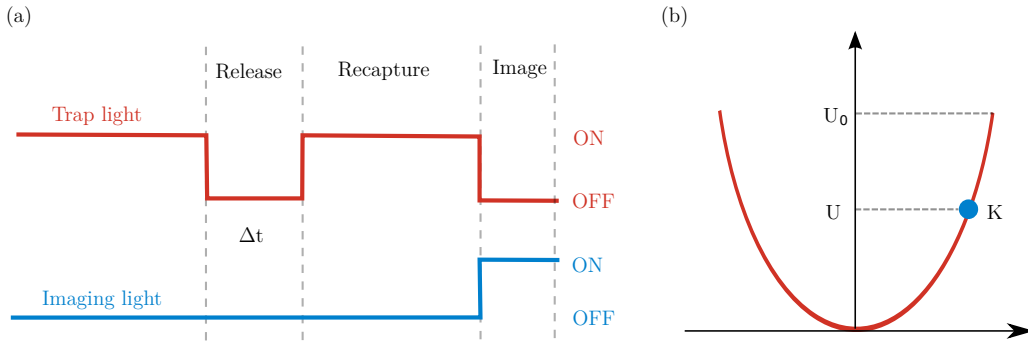


Figure 5.16: Release and recapture procedure. (a) Atoms are released for a variable amount of time before being recaptured in the dipole trap and imaged. (b) To be successfully recaptured the total energy of an atom, $E = U + K$, must be less than the trap depth, U_0 .

recapture process. The model used follows the method described in [106]. Given an initial estimate of the atom temperature, the standard deviation of the spatial distribution and velocity distribution of the atoms can be calculated by assuming a Boltzmann distribution. A random distribution of atomic velocities and initial positions in the trap is generated using these standard deviations. For a release time of Δt the final position of an atom is calculated from its velocity. The trap potential at the atoms new position is then calculated. The total energy of the atom is compared to the trap depth to determine whether it is recaptured. The model is repeated for different release times. The temperature of the atoms is adjusted to fit the experimental data.

The results of the release and recapture method are shown in figure 5.17. Measurements are shown for two different trap depths along with the fit from the Monte-Carlo model (red lines). The temperature of the atomic cloud increases with the trap depth as expected [98]. The temperatures obtained correspond to roughly a tenth of the trap depth. For the typical trap depth of 0.45 mK used in this experiment, the temperature of the cloud has been measured to be $49 \pm 3 \mu\text{K}$.

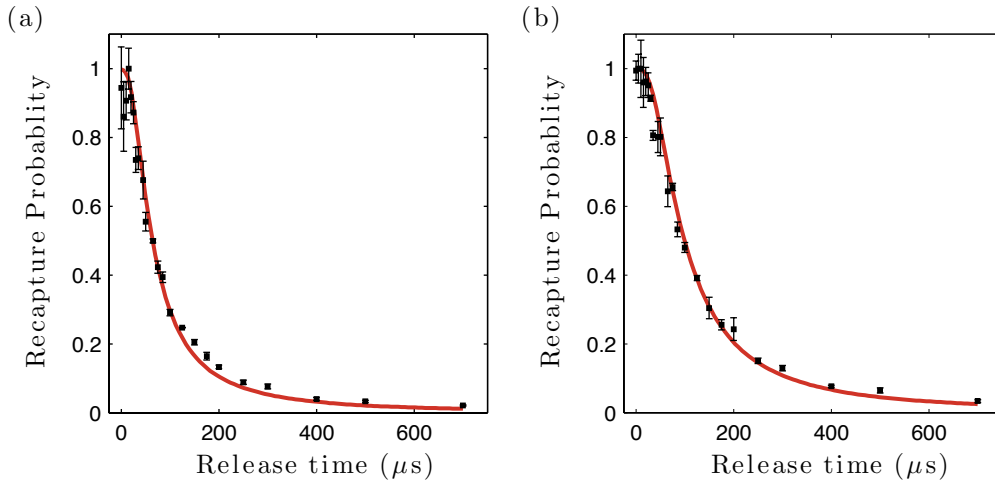


Figure 5.17: Release and recapture results. (a) $U_0 = 0.45$ mK. From the fit the temperature is 49 ± 3 μK . (b) $U_0 = 0.23$ mK. From the fit the temperature is 22 ± 2 μK .

5.4.1 Experimental geometry

Using the measured temperature of the atomic cloud and the waist of the dipole trap beam, the size of the atomic cloud is calculated using equations 5.7 and 5.8 to be roughly $\sigma_z = 21$ μm , $\sigma_r = 0.8$ μm . The peak density of the cloud is roughly 4×10^{11} cm^{-3} , which is an increase of more than an order of magnitude when compared with the atomic density in the MOT. For a blockade radius of 7 μm (typical in this experiment for the $60\text{s}_{1/2}$ state) the cloud can support 3 blockade spheres in a chain within σ_z of the center. This is illustrated schematically in figure 5.18.

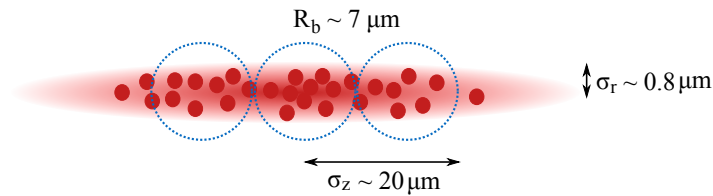


Figure 5.18: Schematic of the experimental geometry. The typical value of R_b for the experiments in this thesis is 7 μm . Since R_b is larger than both the waist of the probe beam and the radial extent of the cloud, the system is essentially one dimensional.

The location and the number of Rydberg excitations depends on the excitation region, defined by the overlap between the probe and coupling fields. Since the waist of the probe beam ($1.2 \mu\text{m}$) is much less than that of the coupling beam ($18 \mu\text{m}$), the probe field defines where the Rydberg excitations are created in the cloud. The cloud is essentially one dimensional when R_b is larger than σ_r . However, the number of Rydberg excitations allowed along z is not well defined due to the Gaussian profile of the probe beam and the atomic cloud. For low probe powers Rydberg excitations are more likely to be created in the center of the cloud where the density is largest. However, increasing the power of the probe beam probably increases the probability of atoms in the wings of the cloud being excited. Note that the Rayleigh range of the probe beam is $5.8 \mu\text{m}$.

In chapter 7 measurements of the photon statistics of the probe field leaving the cloud will be presented. This gives some insight into the number of Rydberg excitations that were created in the medium.

Chapter 6

EIT

So far measurements involving the interaction of the dipole trapped atoms with a single probe field have been considered. As discussed in section 3.2.1, electromagnetically induced transparency (EIT) can be used to make the medium transparent to the probe field. When strongly interacting Rydberg states are used in EIT, the response of the medium can be highly non-linear to changes in the probe intensity due to the dipole blockade effect [20, 27, 107]. The atom-atom interactions mediate effective photon-photon interactions [108] which have recently been observed by measuring photon correlations of the transmitted probe field [20]. EIT therefore provides a method of mapping the strong interactions between atoms onto an optical field which has passed through the sample.

In this chapter evidence of dipole blockade in EIT spectra is presented. The difficulties of observing an associated modification of the photon statistics of the probe field are discussed. Also, spectra where an additional microwave field is coupled to the 3-level EIT system are presented. These are used to calibrate the microwave frequency and intensity.

6.1 Experimental procedure

The excitation scheme and pulse sequence used to measure EIT spectra is shown in figure 6.1. Following the notation of chapter 3, level $|3\rangle$ is a Rydberg state. For all of the experiments described in this chapter the coupling light

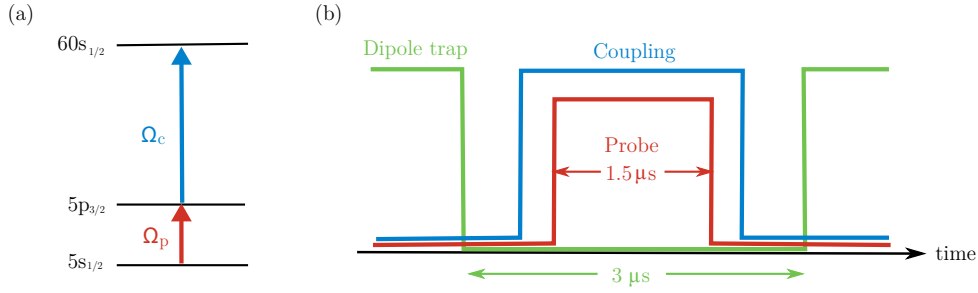


Figure 6.1: Pulse sequence used to measure EIT spectra. (a) The probe beam is coupled to the $60s_{1/2}$ Rydberg state in a ladder scheme. (b) The probe and coupling beams are pulsed on during the $3 \mu\text{s}$ period when the dipole trap is off.

is tuned to the $60s_{1/2}$ state. As with the probe absorption measurements, the excitation light is pulsed out of phase with the dipole trap light. The width of the probe pulse used is $1.5 \mu\text{s}$. This is chosen to be sufficiently long that such that the bandwidth is less than the width of the EIT window. The coupling light is turned on before the probe pulse, and turned off after the probe pulse has been extinguished. As with the probe absorption measurements, photon counts are only binned during the periods where the dipole trap is off, with the rest of the counts ignored.

6.2 Weak probe

The natural starting point when measuring Rydberg EIT spectra is to work in a regime where dipole-dipole interactions are negligible. This can be done by reducing the principal quantum number of the Rydberg state. Alternatively a low probe power can be used where there is negligible population of the Rydberg state.

EIT spectra obtained in the weak probe regime are used to calibrate the Rabi frequency of the coupling laser, Ω_c . The theoretical lineshape used to fit the spectra is obtained by combining equation 3.2 with the imaginary part of the susceptibility, taken from equation 3.7. The method used is the same as that in reference [47]. The fit parameters include Ω_c , Δ_c , Δ_p , γ_{31} , and γ_{21} . Figure 6.2 (a) shows a probe absorption spectrum in the absence of any coupling light. When coupling light is added in figure 6.2 (b) a narrow transparency

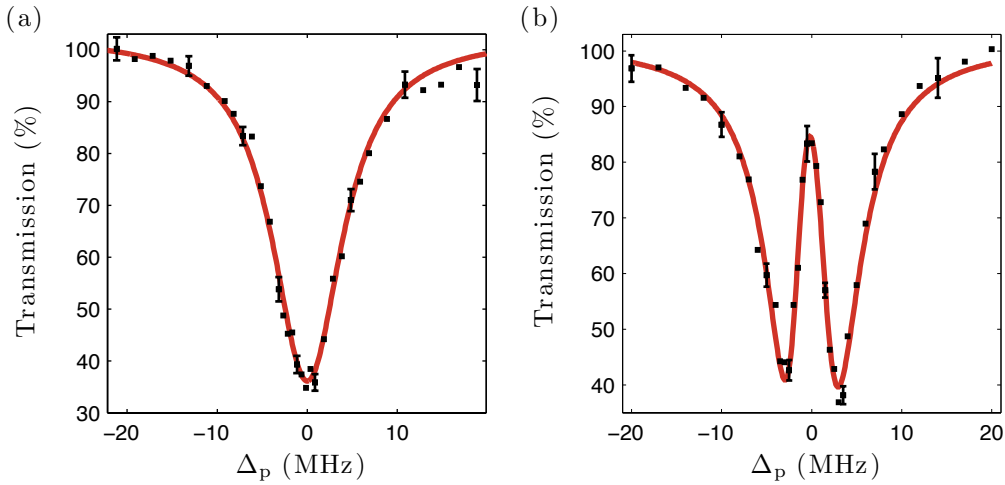


Figure 6.2: Probe absorption and EIT spectra for a weak probe with $\Omega_p/2\pi = 0.9$ MHz ($0.04I_{\text{sat}}$). (a) Probe only absorption spectrum. (b) EIT spectrum with $\Omega_c/2\pi = 5.6 \pm 0.1$ MHz, and $\Delta_c/2\pi = 0.5 \pm 0.2$ MHz.

window appears on resonance. Perfect transparency is not achieved due to the decoherence between the Rydberg state and ground state, γ_{31} . From the fit to the data $\gamma_{31}/2\pi = 0.46 \pm 0.07$ MHz. Since the $60s_{1/2}$ state has a long lifetime of $103.5 \mu\text{s}$ (at 300 K) [109], γ_{31} is dominated by the two-photon linewidth. It can be seen that the EIT spectrum is not completely symmetric. This is due to a small detuning of the coupling laser from two-photon resonance. This is partially compensated by applying a small DC electric field across the atomic cloud to Stark-shift the Rydberg state.

The group velocity of the probe light under EIT conditions can be estimated using the fit parameters obtained from the corresponding EIT spectrum. Since the transmission is given by $T = \exp(-k\chi_I l)$, an estimate of the length of the cloud is required to obtain the imaginary part of the susceptibility. The dimensions of the atomic cloud are discussed in section 5.4.1. Using the imaginary component of the susceptibility, the real part of the susceptibility, χ_R , can be calculated using equation 3.7. Equation 3.11 can then be used to calculate the group velocity. The group velocity is estimated to be of the order $1 \times 10^3 \text{ ms}^{-1}$ for typical experimental parameters used when performing EIT. The group velocity can also be calculated for an arbitrary value of Ω_c using equation 3.12. This is useful when calculating the group velocity during

photon storage, where Ω_c is very small and therefore resolving EIT spectra is difficult.

6.3 Strong probe

The response of a medium undergoing EIT in the regime of dipole blockade can be extremely non-linear when increasing the power of the probe field [20, 27, 107]. Generalising equation 3.1, the non-linear response of a medium is governed by the power-law [11]

$$\mathbf{P} = \epsilon_0(\chi^{(1)}\mathbf{E} + \chi^{(2)}\mathbf{E}^2 + \chi^{(3)}\mathbf{E}^3 + \dots), \quad (6.1)$$

where the polarisation induced in the medium now depends on higher order components of the electric field. Taking into account the non-linear susceptibility terms, we can define an effective susceptibility given by $\chi_{\text{eff}} = \chi^{(1)} + \chi^{(2)}E + \chi^{(3)}E^2$. For most materials the higher order susceptibility terms are small [11]. Therefore in general the contribution of the non-linear terms in equation 6.1 only becomes significant for large E . However, results shown in reference [47] show that very large values of the third-order susceptibility, $\chi^{(3)}$, are possible in Rydberg media for modest electric fields. Even stronger non-linearities occurring at the single photon level were demonstrated in [20]. The third-order susceptibility also gives rise to an intensity dependent refractive index, which can lead to self-defocusing of the probe beam for repulsive atomic interactions [110]. Note that inversion symmetry must be broken for the second-order susceptibility to be non-zero [11]. Therefore $\chi^{(2)} = 0$ in general for atomic clouds.

To demonstrate this non-linearity, EIT transmission spectra are plotted in figure 6.3 for two different probe powers. For a weak probe field (blue) there is a large transparency window on resonance. However when the power of the probe field is increased (red) the transparency on resonance is reduced significantly. In the case of high probe powers it is not valid to fit the spectrum using the susceptibility from equation 3.7 as this neglects the effects of population transfer to the Rydberg state and interatomic interactions. The line through the data points is purely a guide to the eye.

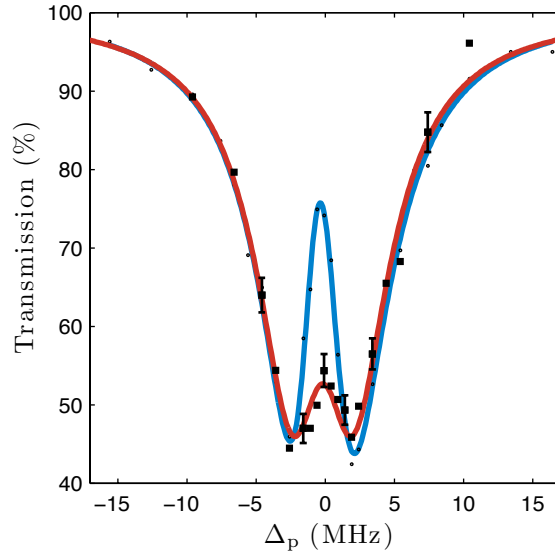


Figure 6.3: Suppression of transmission on EIT resonance for a strong probe beam. For a weak probe beam (blue) with $\Omega_p/2\pi \approx 0.9$ MHz ($0.04I_{\text{sat}}$) there is a large fraction of transmitted probe light. When increasing the power of the probe beam (red) to $\Omega_p/2\pi \approx 4.5$ MHz ($1.1I_{\text{sat}}$) there is a suppression of the transmitted light. From the weak probe data $\Omega_c/2\pi = 4.3 \pm 0.1$ MHz, and $\Delta_{\text{EIT}}/2\pi = 2.2 \pm 0.1$ MHz

The suppression of the transparency is evidence of dipole blockade [27]. In each blockade sphere only a single Rydberg excitation is allowed. As a result the excitation light is not resonant with the two-photon transition for the remaining fraction of atoms, and the probe field is therefore scattered [27, 110, 111]. With increasing probe power the probability of creating Rydberg excitations increases, as does the probability of having multiple probe photons in the same blockade sphere [111]. The observed transparency is therefore reduced. In reference [27] it was shown that the optical response is *cooperative* in nature, as the strength of the non-linearity depends on the atomic density. This is a consequence of the fact that the non-linearity is due to dipole-dipole interactions between the atoms. The non-linear response is therefore not only governed by the electric field of the probe.

Recall equation 2.4, which relates the blockade radius to the interaction strength and the linewidth of the Rydberg transition. In the case of EIT, for the probe beam to be transmitted its frequency must lie within the trans-

parency window. The blockade radius can therefore be written [24, 110]

$$R_o = \left(\frac{C_6}{\hbar\Delta_{\text{EIT}}} \right)^{\frac{1}{6}}, \quad (6.2)$$

where $C_6 = -140 \text{ GHz } \mu\text{m}^6$ for 60s60s interactions [112], and Δ_{EIT} is the FWHM of the transparency window. Here R_o represents the optical blockade radius, relevant for conditions of EIT. For $\Delta_{\text{EIT}}/2\pi = 1 \text{ MHz}$ the blockade radius is $R_o \approx 7 \mu\text{m}$.

The transparency on resonance can be studied for a range of different probe powers in order to extract the value of $\chi^{(3)}$ [47]. However at the probe powers where suppression is observed there is also loss of atoms from the dipole trap due to heating (see section 5.3.3). Measuring high resolution EIT spectra at these powers is therefore difficult in this experiment.

In principle the suppression of the transparency on resonance should be accompanied by antibunching of the probe photons [111]. Observation of this effect would provide direct evidence of photon interactions in the medium. In the extreme case where a single superatom with a high optical depth undergoes EIT, a regular train of single photons should leave the sample, with all other probe photons being scattered. This is equivalent to the “photon-blockade” effect, first proposed and demonstrated in cavity QED experiments [17, 18]. More recently this effect has been demonstrated in free-space using Rydberg atoms [20]. Effectively the medium behaves as a filter for single photons.

The modification of the photon statistics of the probe field are difficult to observe in this experiment. This is due to low optical depth of the atomic cloud, whose effects are two-fold. Firstly, there is a large fraction of unscattered probe photons which contaminate the probe photons which have undergone EIT. Secondly, the temporal separation of the probe photons leaving the medium is small. Equation 3.15 can be used to relate the time taken for a photon undergoing EIT to propagate over a distance of one blockade radius, to the optical depth per blockade sphere. Due to the low optical depth of the medium this time is very small (of the order of 10 ns) and therefore correlation measurements would have to be performed with a very high (around 1 ns) timing resolution. Consequently the time taken to perform $g^{(2)}$

measurements would be very large. For these reasons the photon statistics of the probe field leaving the medium were not measured. A partial solution to these problems is to store the probe photons in the medium to isolate the signal from background photons. This is discussed in the next chapter.

6.4 Microwave dressing

The modification of EIT spectra when adding an additional microwave field coupling to a fourth atomic level will now be examined. The purpose of these measurements is to calibrate the microwave power and frequency for experiments described in chapter 8. Rydberg atoms couple very strongly to microwave fields due to the strong dipole moments of microwave transitions between adjacent Rydberg states. Rydberg EIT spectra are therefore very sensitive to microwave fields [113]. Dressing Rydberg states with a microwave field provides a method of controlling the interaction strength between atoms [51, 52].

To measure EIT spectra with microwave coupling, microwave pulses of $1.6 \mu\text{s}$ duration are applied in phase with the probe and coupling fields. The experimental sequence is shown in figure 6.4. The microwaves couple the $60s_{1/2}$ and $59p_{3/2}$ states for all of the data presented in this section. The linear polarisa-

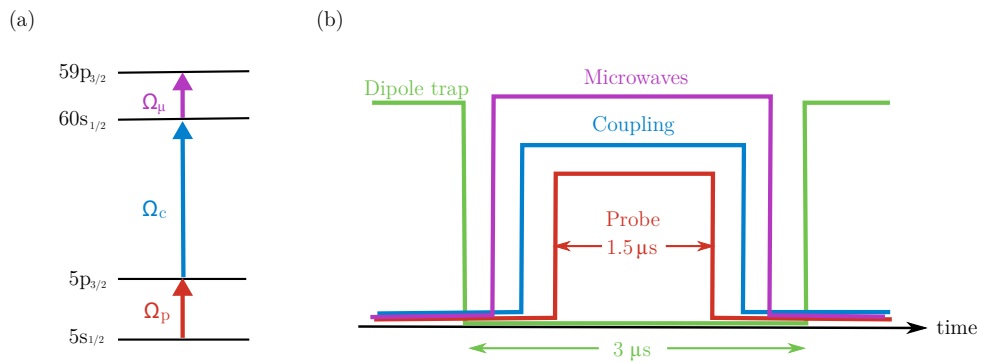


Figure 6.4: Pulse sequence used for studying EIT spectra with microwave coupling. (a) The $60s_{1/2}$ Rydberg state is coupled to the $59p_{3/2}$ state with a microwave field. (b) The microwave field is pulsed on during the periods where the dipole trap is off.

tion of the microwaves is oriented along the quantisation axis such that the microwaves drive π -transitions. The data is fit using the expression for the four-level susceptibility given by equation 3.21. The additional fit parameters compared with the 3-level EIT spectra are Ω_μ , Δ_μ , and γ_{41} . The typical values of $\gamma_{41}/2\pi$ obtained from the fits are in the range 0.1 MHz-1.1 MHz.

The approximate resonance frequency for the $60s_{1/2}$ to $59p_{3/2}$ transition is found by studying EIT spectra at different microwave frequencies. The microwave pulses typically used in the experiments described in chapter 8 have

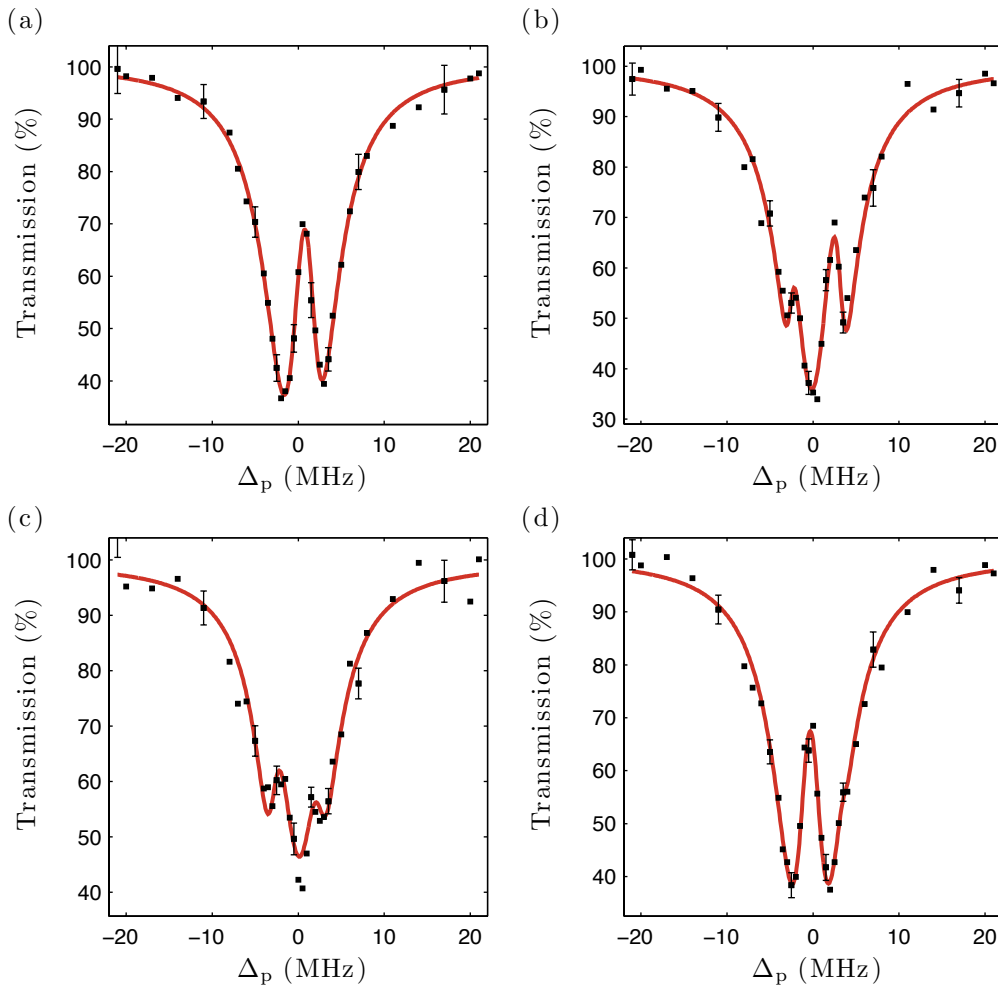


Figure 6.5: Variation of EIT spectra with frequency of applied microwave field. (a) No microwave field applied. (b) Microwave field of frequency 18.518 GHz. (c) Microwave field of frequency 18.524 GHz. (d) Microwave field of frequency 18.530 GHz.

a duration of 150 ns. The inverse of this pulse duration gives a corresponding bandwidth of around 7 MHz. Therefore the resonance frequency only needs to be determined to within a precision of a few MHz. Figure 6.5 shows spectra taken at a fixed microwave power, for a variety of microwave frequencies. The value of the microwave detuning, Δ_μ , was extracted from the fit at each microwave frequency. However, it was found that these values were not reliable. For the fits to converge the free parameters that were used included Ω_μ , Δ_μ , γ_{41} , Δ_c and Δ_p . The values of Δ_μ obtained were probably not sensible due to the large number of free parameters. However, the variation in the shape of the spectra as the microwave frequency is varied provides some insight into the approximate resonance frequency. For example, when increasing the microwave frequency in going from figure 6.5 (b) to figure 6.5 (c) the spectrum becomes more symmetric. However when the microwave frequency is increased further in figure 6.5 (d), there is very little perturbation caused by the microwave field relative to the EIT spectrum in 6.5 (a). The resonance frequency was therefore taken to be roughly 18.524 GHz for this transition. Note that this differs from the value of 18.513 GHz calculated using quantum defects [114] by J. D. Pritchard. This difference is probably due to energy level shifts caused by the external fields present in the vacuum chamber.

To calibrate the microwave Rabi frequency the frequency of the microwaves was fixed while their power was varied. Figures 6.6 (a)-(c) show spectra taken for increasing microwave power. The effect of the microwaves is to split the EIT transmission peak. For microwave Rabi frequencies that are many times the coupling Rabi frequency, it is not possible to determine Ω_μ from the spectra since the splitting becomes too great. Although the microwave Rabi frequency can only be extracted for a limited range of powers, the spectra are much more sensitive to the microwave power compared with the microwave detuning. In figure 6.6 (d) the microwave electric field is plotted as a function of the nominal power from the microwave source. The dependence is approximately linear as expected.

The large number of free parameters required to fit the spectra suggests that the 4-level model used is not completely accurate. This could be due to imperfect polarisation of the microwaves. The microwave Rabi frequency is very

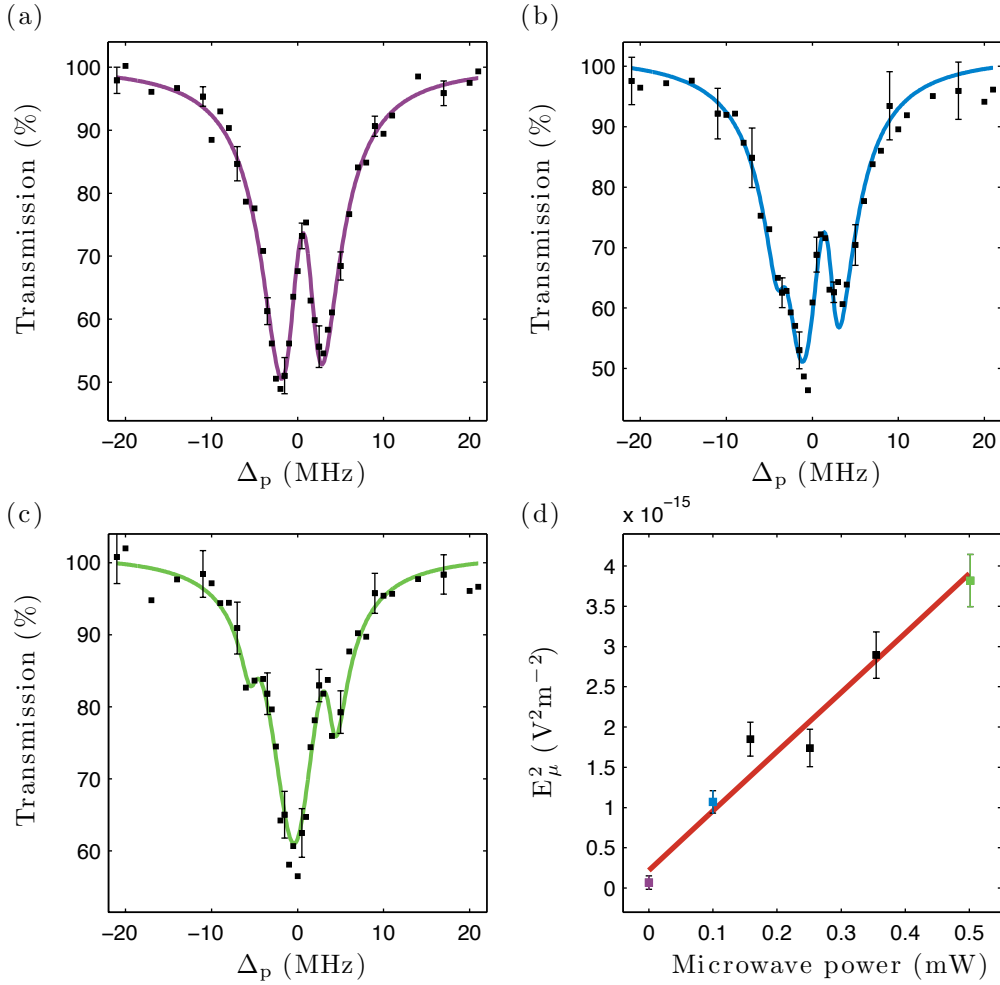


Figure 6.6: Variation of EIT spectra with power of applied microwave field. In each case $\Omega_c = 4.2 \pm 0.1$ MHz. (a) Control experiment where there is no microwave field applied. From fit $\Omega_\mu = 0.7 \pm 0.7$ MHz. (b) $\Omega_\mu = 4.3 \pm 0.4$ MHz. (c) $\Omega_\mu = 8.1 \pm 0.5$ MHz. (d) The microwave electric field extracted from the fitted spectra as a function of the nominal power from the microwave source.

sensitive to the position of the antenna. This suggests that the microwaves form an interference pattern due to reflections within or around the vacuum chamber. The reflections could account for the microwaves driving imperfect π -transitions which would invalidate the 4-level model. Also the optical pumping of the atoms prior to Rydberg excitation is imperfect. Again this means that the microwave field is driving multiple transitions.

Chapter 7

Photon storage

In section 6.3 evidence of dipole blockade is presented in EIT spectra taken at different probe powers. One of the aims of this experiment is to observe an associated modification of the probe photon statistics due to dipole blockade. However, the low optical depth of the atomic cloud means that in practice this is very difficult to observe.

Rather than measuring the photon statistics of the probe field undergoing EIT, the field is stored using the principles described in section 3.2.2. After a finite storage time, the photon statistics of the retrieved field are then studied [21]. The retrieved field is separated temporally from probe photons which are not successfully stored, giving a larger signal to noise ratio compared with a measurement on the field undergoing EIT. As will be discussed later in chapter 8, storing the probe photons also has additional advantages. For example it allows the interactions between neighboring Rydberg polaritons to be studied, and it also allows the state of the stored photons to be controlled.

7.1 Experimental procedure

As discussed in section 3.2.2, to store photons from a probe field undergoing EIT the intensity of the coupling field must be lowered towards zero. The experimental sequence used is shown in figure 7.1. The probe field is stored by reducing the intensity of the coupling field over a time of roughly 100 ns. At this time photons from the probe field are stored as Rydberg polaritons.

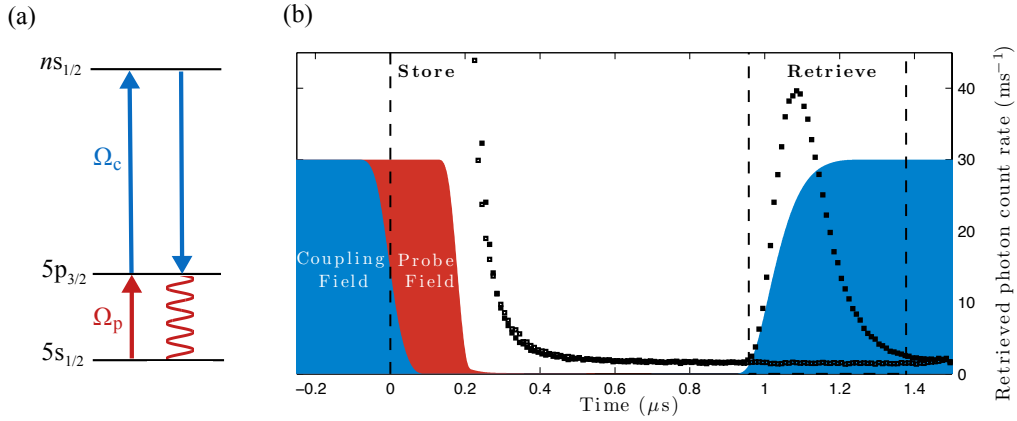


Figure 7.1: Experimental procedure for the storage and retrieval of probe photons. (a) The 3-level atomic scheme. (b) Pulse timing sequence. At $0 \mu\text{s}$ the intensity of the coupling field (blue) is lowered and photons from the probe field (red) are stored. Typically the probe pulse has a total duration of $1.6 \mu\text{s}$. After a storage time of roughly 900 ns the coupling field is turned back on. The retrieved field (black squares) appears as a pulse, in this case with a FWHM of $120 \pm 20 \text{ ns}$. The background signal without atoms (black circles) is also shown. The dashed lines around the retrieved signal show the time window over which data is extracted. The relative heights of the pulses are not to scale.

After a finite storage time the coupling field is turned back on to read out the polariton field. The field retrieved along the probe propagation direction is collected in a multi-mode optical fiber. This experimental cycle is repeated every $6 \mu\text{s}$, following the trap modulation technique described in section 5.3. The retrieved signal (black squares) is taken in the window bounded by the dashed lines. The number of retrieved photons is corrected for the finite background count level (black circles). The background level is the signal obtained when no atoms are loaded into the dipole trap.

In section 5.3.3 it was shown that the drop in probe absorption over the dipole trap modulation time was dependent on the probe power. At high probe powers large loss rates of atoms from the trap are observed. One would therefore expect a similar variation in the storage efficiency over the trap modulation time. Figure 7.2 shows the retrieved photon signal as a function of trap modulation time for different probe powers. For the relatively low probe powers in figure 7.2 (a), it can be seen that the retrieved signal

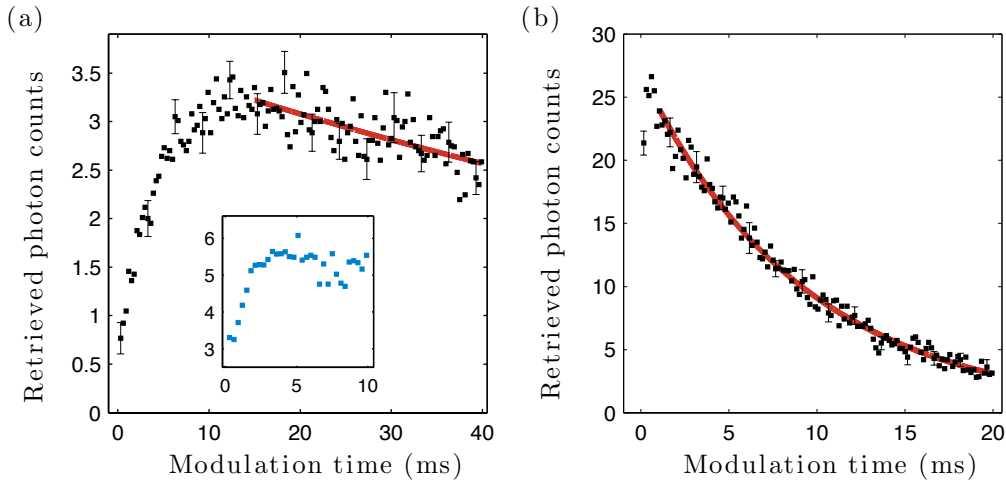


Figure 7.2: Variation in retrieved photon signal over trap modulation time. (a) Relatively weak probe with power ≈ 1 pW ($0.03I_{\text{sat}}$). The decay rate over the fitted region (red line) is $\Gamma = 9 \pm 1$ s $^{-1}$. Inset: Higher probe power ≈ 3 pW ($0.08I_{\text{sat}}$). The rate of increase of the retrieved photon signal at short modulation times is larger in this case. (b) Strong probe with power ≈ 20 pW ($0.5I_{\text{sat}}$). The fit gives $\Gamma = 108 \pm 1$ s $^{-1}$.

initially increases at short modulation times before dropping at longer times. It is not understood why the retrieved signal increases at short modulation times. The rate of increase of the number of stored photons becomes larger at higher probe powers, as shown in the inset of 7.2 (a), which could suggest that the mechanism is associated with heating of the cloud. Recalling figure 5.14, similar responses have not been observed when studying the probe absorption as a function of modulation time. Therefore the increase in the retrieved photon signal cannot be attributed to an increased optical depth of the medium. For the data taken at a higher probe power in figure 7.2 (b), the storage efficiency drops much more rapidly. It is therefore important when comparing measurements at different probe powers to account for the temporal variation in the retrieved signal. Sufficiently short measurement times were used over which the retrieved signal did not decrease significantly. The data in figure 7.2 is fitted to a function of the form of equation 5.10 in the regions with a red line. It is instructive to compare the one-body loss coefficient, Γ , of the retrieved photon signals to those of the probe absorption

signals in figure 5.14. For a probe power of around 20 pW the retrieved photon signal decays with $\Gamma \approx 110 \text{ s}^{-1}$ whereas the probe absorption signal decays with $\Gamma \approx 40 \text{ s}^{-1}$. The retrieved photon signal therefore decays much more quickly. This suggests that the reduction in the optical depth of the cloud is not completely responsible for the decay of the retrieval signal. The faster decay could be due to increased sensitivity to heating of the cloud and to loss of atoms. This seems reasonable since heating would lead to increased motional dephasing. In addition, atom loss would also reduce the directionality of the read-out [76].

7.2 Optimisation

The ultimate limit on the efficiency of the photon storage process is the finite optical depth of the medium [75]. This was discussed briefly in section 3.2.2. Given a fixed optical depth there are a number of experimental parameters that can be adjusted to optimise the storage efficiency. The experimental procedure will be considered in two parts, photon storage followed by photon retrieval.

The storage efficiency, η_{store} , is defined in this work as

$$\eta_{\text{store}} = \frac{\bar{n}_{\text{store}}}{\bar{n}}, \quad (7.1)$$

where \bar{n} is the mean photon number of the incident probe pulses, and \bar{n}_{store} is the mean number of stored photons. This definition is reserved for the regime where there are no saturation effects such as dipole blockade. Here the response of the medium is expected to be linear in \bar{n} . As will be shown shortly, given a fixed \bar{n} , \bar{n}_{store} depends strongly on a few key experimental parameters. Note that the mean quantities correspond to the average values per store/retrieve cycle. These are obtained by averaging over many, typically several tens of thousands, store/retrieve cycles.

The retrieval efficiency, η_{ret} , is defined as

$$\eta_{\text{ret}} = \frac{\bar{n}_{\text{ret}}}{\bar{n}_{\text{store}}}, \quad (7.2)$$

where \bar{n}_{ret} is the mean number of photons retrieved per store/ retrieve cycle. As discussed in section 3.2.2, the retrieval efficiency is limited by dephasing of the spin wave. Since the lifetime of Rydberg states is very long the main source of dephasing occurs due to the motion of the atoms during the storage interval. The lifetime of the spin wave has not been measured, but given the temperature of the atomic cloud it is expected to be limited to roughly $3 \mu\text{s}$ due to motional dephasing (calculated using equation 3.19).

Taking a fixed probe power, and therefore \bar{n} , \bar{n}_{ret} is now studied as a function of various experimental parameters. In figure 7.3 the mean number of photons retrieved per store/retrieve cycle is plotted as a function of the width of the probe pulse for three different values of \bar{n} . The width of the probe pulse is varied about its centre. For small probe pulse widths the bandwidth of the pulse exceeds the width of the EIT window, which for this data is approximately $\Delta_{\text{EIT}}/2\pi = 1 \text{ MHz}$. Frequency components of the probe pulse outside the EIT window are absorbed and therefore not stored [12]. For longer probe pulses the bandwidth is reduced and therefore more photons are stored. Due

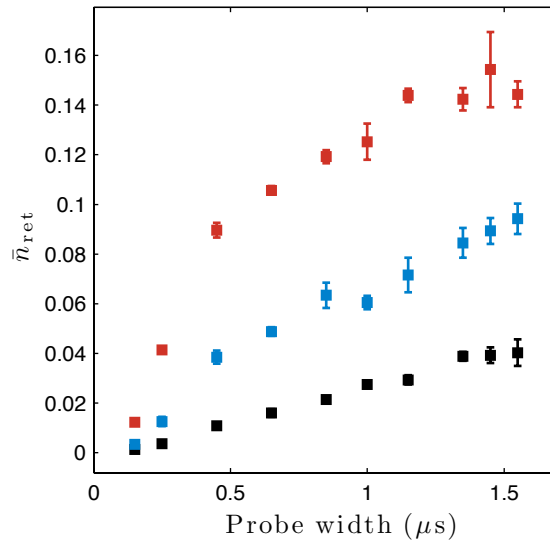


Figure 7.3: Mean number of retrieved photons per store/ retrieve cycle, \bar{n}_{ret} , as a function of the width of the probe pulse. The data sets correspond to probe powers of approximately 1 pW (black), 3 pW (blue), and 10 pW (red). For the maximum probe width of $1.6 \mu\text{s}$ these powers correspond to roughly $\bar{n} = 6$ (black), $\bar{n} = 18$ (blue), and $\bar{n} = 60$ (red).

to the finite time period where the dipole trap is off, the maximum width of the probe pulse that can be used is limited. In the following experiments the width of the probe pulse is typically $1.6 \mu\text{s}$. The bandwidth of the probe pulse could be reduced further by using a smoother pulse shape instead of the square pulse used in this experiment. For large probe powers (red data) the number of retrieved photons saturates for long probe pulses. This occurs because the storage efficiency is no longer limited by the bandwidth of the probe pulse.

The storage efficiency also depends on the peak Rabi frequency of the coupling laser. For large values of Ω_c the group velocity of the probe pulse is not as strongly reduced and therefore it is not compressed as much inside the medium (equation 3.12). For small values of Ω_c the bandwidth of the EIT window is reduced (equation 3.10) and therefore more frequency components of the probe pulse are absorbed. The dependence of the number of retrieved photons on Ω_c is shown in figure 7.4 (a). The storage efficiency peaks at around $\Omega_c/2\pi = 4 \text{ MHz}$. The shape of the retrieved pulse also varies with Ω_c as shown in figure 7.4 (b). This reflects the speed at which the field is retrieved from the medium. For small values of Ω_c (red), where the group

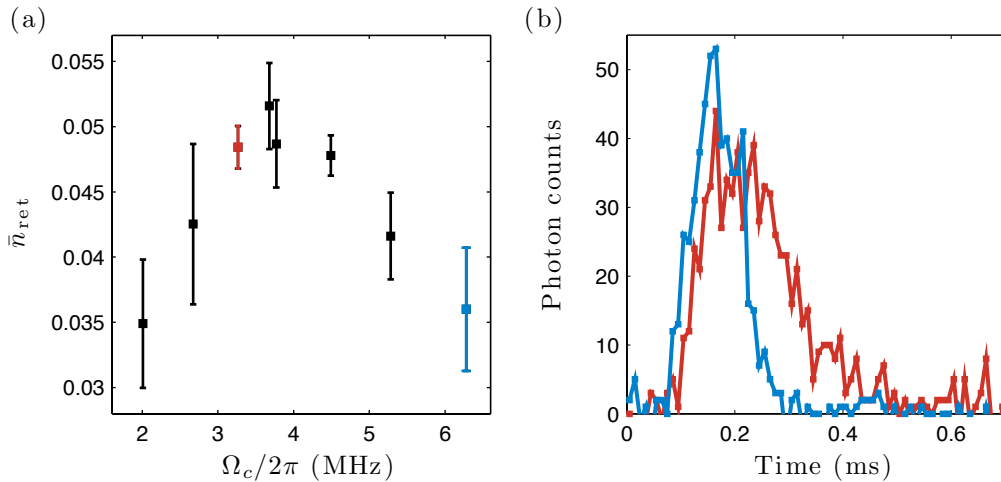


Figure 7.4: Dependence of the storage and retrieval process on the Rabi frequency of the coupling laser. The probe pulse has a width of $1.6 \mu\text{s}$ and $\bar{n} = 22$. (a) Mean number of retrieved photons as a function of Ω_c . (b) Retrieved photon pulse for two different values of Ω_c .

velocity of the light is small, the retrieved field is stretched as it leaves the medium. At larger values of Ω_c (blue) the field is retrieved more quickly and therefore the width of the pulse is smaller.

Another important parameter to consider when optimising the storage efficiency is the probe detuning, Δ_p . Figure 7.5 shows EIT spectra and the

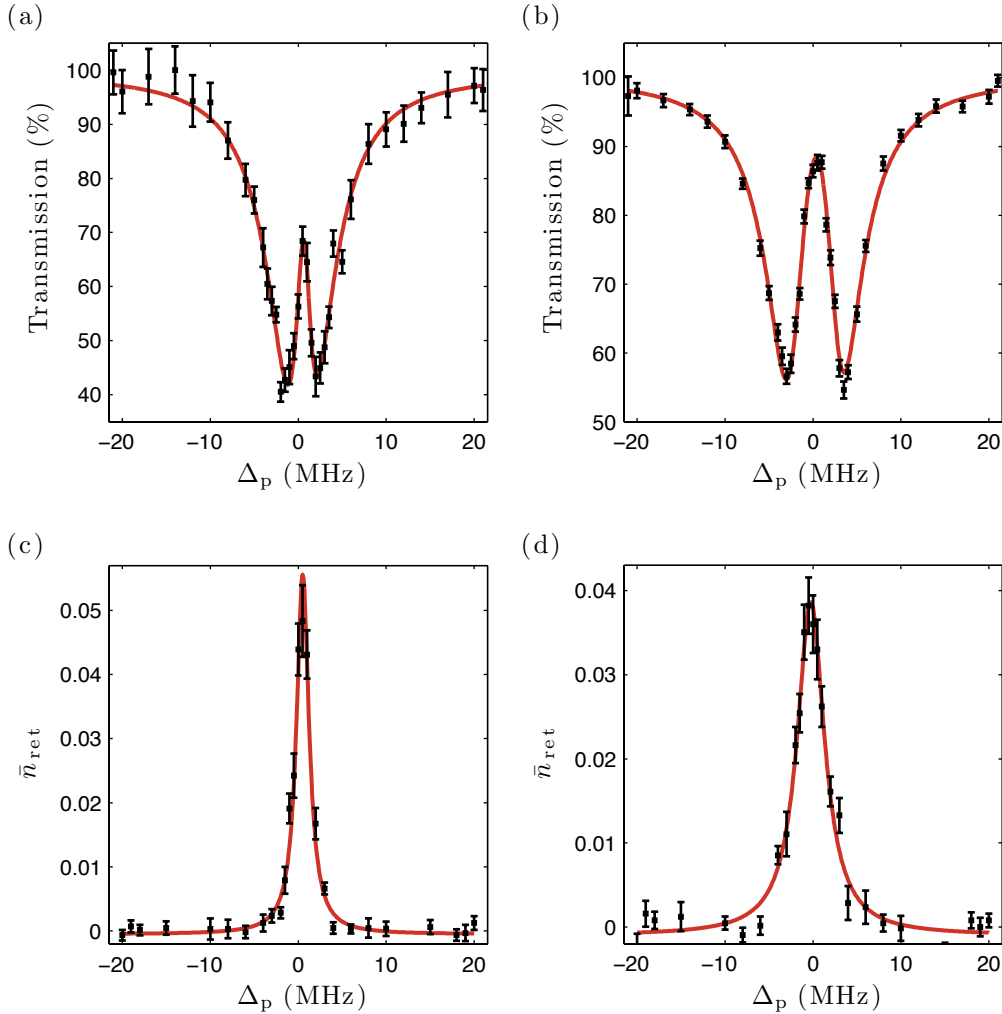


Figure 7.5: Dependence of storage bandwidth, Δ_{store} , on Ω_c . (a) EIT spectrum with $\Omega_c/2\pi = 3.0 \pm 0.1$ MHz, and $\Delta_{\text{EIT}}/2\pi = 1.6 \pm 0.2$ MHz. (b) EIT spectrum with $\Omega_c/2\pi = 6.3 \pm 0.1$ MHz, and $\Delta_{\text{EIT}}/2\pi = 3.8 \pm 0.1$ MHz. (c) Storage bandwidth for the same experimental parameters as (a). From the fit $\Delta_{\text{store}}/2\pi = 1.7 \pm 0.1$ MHz. (d) Storage bandwidth for the same experimental parameters as (b). From the fit $\Delta_{\text{store}}/2\pi = 3.8 \pm 0.3$ MHz. Note that Δ_{store} and Δ_{EIT} are full widths at half-maximum.

corresponding bandwidth of the storage process for two different values of Ω_c . As expected the optimum probe detuning coincides with the maximum transparency on the EIT resonance. The bandwidth of the storage process is dependent on Ω_c since this determines the width of the EIT resonance, Δ_{EIT} . It can be seen from figure 7.5 that the storage bandwidth, Δ_{store} , directly corresponds to the width of the EIT window.

The dependence of the storage efficiency on the optical depth of the cloud has not been explicitly studied in this experiment. However large drops in the number of retrieved photons have been observed over long measurement times. This seems to be accompanied by a significant reduction in the probe absorption and is attributed to poor dipole trap loading due to movement of the MOT (as discussed in section 5.2).

7.3 Saturation

In the regime of dipole blockade there should be a limit on the number of photons that can be stored inside the medium since each blockade sphere can only support a single Rydberg excitation. A simple method of modeling this saturation is illustrated in figure 7.6. The probe light is initially considered to be a coherent state. Therefore the probe pulses have a Poissonian distribution of photon numbers (see section 4.3.1). Consider an atomic medium which can contain a maximum of \mathcal{N} blockade spheres. Photon numbers which are greater than the number of blockade spheres, \mathcal{N} , cannot be stored due to the blockade condition. Instead these photon numbers create \mathcal{N} Rydberg excitations, the maximum allowed. This effectively changes the initial coherent state of the probe light to a truncated coherent state, with an excess of photons at $n = \mathcal{N}$. In order to accurately model the experiment the storage efficiency and the retrieval efficiency must be taken into account. These are defined in section 7.2. The finite storage efficiency effectively attenuates the initial mean photon number of the probe pulses by a factor η_{store} . This means that higher probe powers are needed to saturate the medium compared to the case where the storage process is perfect. The finite retrieval efficiency, η_{ret} , means that the number of photons retrieved from the medium is less than the number of photons stored. Note that all

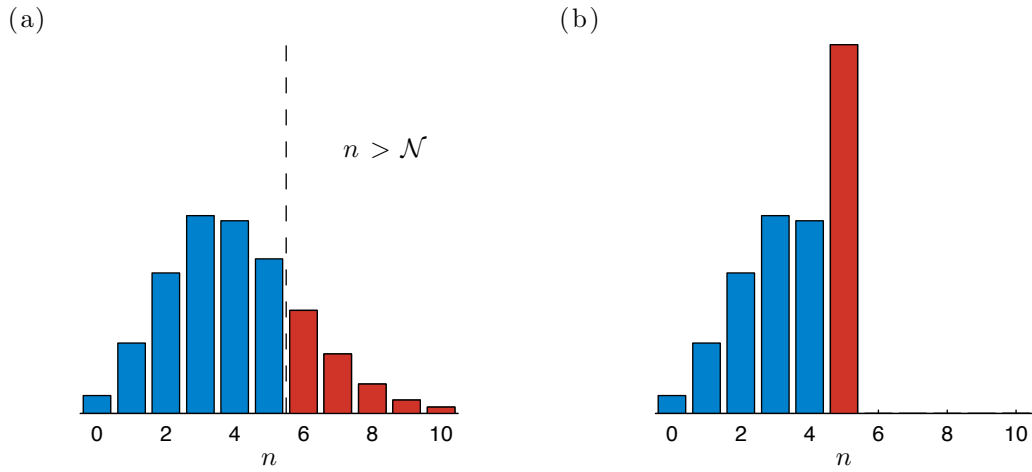


Figure 7.6: Modification of the photon number distribution of the probe field in the regime of dipole blockade. (a) Initial Poisson distribution of photon numbers in probe field with $\bar{n} = 4$. Photon numbers higher than the maximum number of blockade spheres, $\mathcal{N} = 5$, are highlighted. (b) Stored photon number distribution. Photon numbers greater than \mathcal{N} are mapped back onto $n = \mathcal{N}$.

of the experimentally obtained values of \bar{n}_{ret} in this chapter are corrected for the finite detection efficiency.

The model is implemented using a Monte-Carlo technique. A photon number in each incident probe pulse is randomly generated from a Poisson distribution with mean \bar{n} . For each probe pulse containing n photons, a random number of photons are stored using a binomial distribution with a probability of success of η_{store} . The number of photons stored is then compared to the maximum number of blockade spheres \mathcal{N} and modified accordingly, as illustrated in figure 7.6. The number of photons retrieved is generated using a binomial distribution with a probability of success, η_{ret} . The results of the model are illustrated in figure 7.7 for different values of η_{store} and \mathcal{N} . The retrieval efficiency is fixed at $\eta_{\text{ret}} = 100\%$ for simplicity. As expected, larger values of \bar{n} are required to observe the saturation in the number of stored photons as η_{store} is reduced. As \mathcal{N} is increased the number of retrieved photons saturates at correspondingly higher values.

The experimental observation of saturation in the number of stored photons is presented in figure 7.8. The number of retrieved photons is studied as a

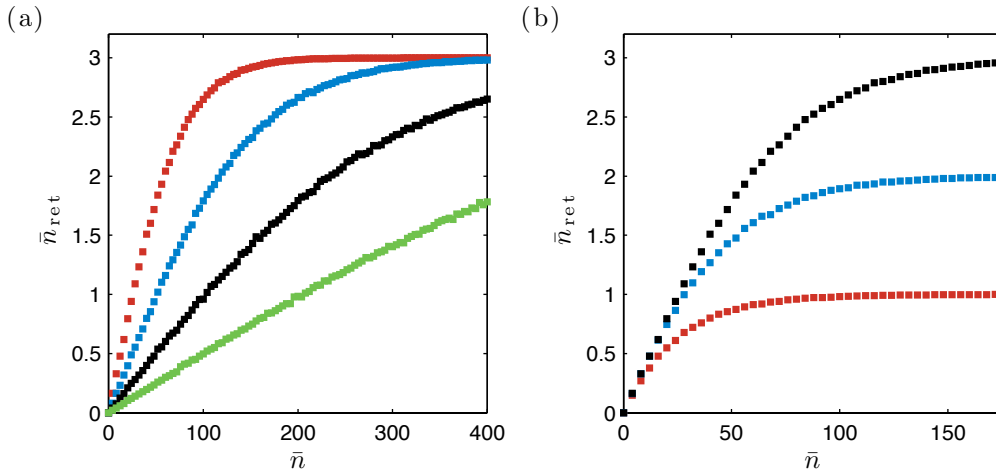


Figure 7.7: Results of Monte-Carlo model simulating saturation in the number of photons stored. (a) Mean number of retrieved photons, \bar{n}_{ret} , as a function of mean photon number of probe input pulse, \bar{n} , for different storage efficiencies. The different points correspond to storage efficiencies of $\eta_{\text{store}} = 4\%$ (red), 2% (blue), 1% (black), and 0.5% (green). The number of blockade spheres is fixed at $\mathcal{N} = 3$. (b) Dependence on the number of blockade spheres for $\mathcal{N} = 3$ (black), 2 (blue), and 1 (red). The storage efficiency is fixed at $\eta_{\text{store}} = 4\%$. In both cases $\eta_{\text{ret}} = 100\%$.

function of the incident probe power for different Rydberg states. Varying the Rydberg state changes the size of the blockade radius. Note that each dataset has been processed over a fixed modulation time during which the retrieved signal does not drop as the probe power is increased. This avoids an apparent saturation appearing which is not a consequence of dipole blockade, but which is rather due to loss and heating of the atoms. It can be seen that \bar{n}_{ret} saturates at lower values as the principal quantum number of the Rydberg state is increased. This is expected since the blockade radius scales as $n^{11/6}$, and therefore fewer photons can be stored inside the medium as n is increased. For $n = 60$ (blue points) the experimental data has been fit using the Monte-Carlo model with $\mathcal{N} = 4$, and the storage and retrieval efficiencies as free parameters. This choice of \mathcal{N} is justified in the following chapter. From the fit $\eta_{\text{store}} = 6 \times 10^{-2}$, and $\eta_{\text{ret}} = 3 \times 10^{-2}$. Note that the accuracy of these values is not clear. It will be shown in the next section that other quantitative predictions of the model do not agree with experimental measurements. The storage and retrieval efficiencies obtained are very low.

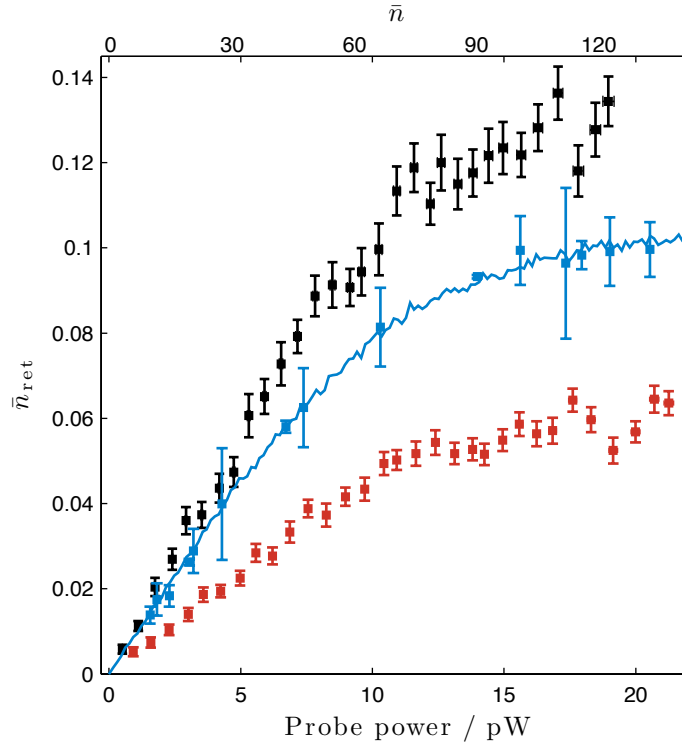


Figure 7.8: Mean number of retrieved photons per store/ retrieve cycle, \bar{n}_{ret} , as a function of probe power. The retrieved signal saturates at different values for different Rydberg states. The different data sets correspond to the Rydberg states $46s_{1/2}$ (black), $60s_{1/2}$ (blue), and $80s_{1/2}$ (red). The fit to the data for $60s_{1/2}$ has been generated from the Monte-Carlo model with $\mathcal{N} = 4$. From the fit $\eta_{\text{store}} = 6 \times 10^{-2}$, and $\eta_{\text{ret}} = 3 \times 10^{-2}$.

Although the storage efficiency is ultimately limited by the low optical depth of the atomic cloud, the storage process is far from optimised. For example, the temporal variation of the coupling field during the writing stage could be adjusted for optimum storage [75]. The storage efficiency has probably been slightly underestimated since part of the probe pulse does not overlap with the coupling field (see figure 7.1), and therefore does not contribute to the storage process. The retrieval efficiency is probably significantly reduced by motional dephasing of the spin waves which reduces the directionality of the read-out. The storage time is approximately 900 ns, which is a significant fraction of the estimated spin-wave lifetime of $2 \mu\text{s}$. As will become clear in the next chapter, the storage time cannot be reduced significantly since

for some experiments the stored photons are coupled to a microwave field. The directionality of the emission also depends on the number of atoms per blockade sphere (see section 3.2.2). Since there are only roughly 10-20 atoms per blockade sphere for $n = 60$, the directionality of the emission is probably poor even in the absence of motional dephasing [8].

7.4 Photon statistics

The observed saturation in the number of stored photons provides further evidence that dipole blockade effects are significant in the system under consideration. Recently it has been shown that dipole blockade can be exploited in photon storage experiments to produce a highly efficient single photon source [19]. In order to study the effect of dipole blockade on the statistics of the probe photons, $g^{(2)}$ is measured for the retrieved field. This involves performing intensity correlation measurements on the retrieved field using a Hanbury Brown Twiss interferometer, as described in section 4.3.2. In general the entire retrieved pulse is binned over the region highlighted in figure 7.1, giving a detected photon number on each SPAD for every store/retrieve cycle. The quantity that is of interest in most cases is therefore $g^{(2)}(0)$ since $g^{(2)}(\tau \neq 0)$ corresponds to photon correlations between different experiments. In principle the different store/retrieve experiments should be uncorrelated. It would be interesting to study photon correlations within each retrieved pulse, however this requires more signal and therefore longer data accumulation times. This is not feasible with the current experimental setup.

7.4.1 Predictions of Monte-Carlo model

It is instructive to study the dependence of $g^{(2)}(0)$ on key experimental parameters predicted by the Monte-Carlo model introduced earlier in this chapter. For each retrieved photon signal generated by the model, a 50:50 beam splitter in a Hanbury-Brown-Twiss interferometer is simulated using a binomial distribution with a probability of success of 0.5. The number of photons at each output of the beam-splitter is then cross-correlated over all store/

retrieve cycles according to equation 4.8.

In figure 7.9 (a) the dependence of $g^{(2)}(0)$ on the number of blockade spheres, \mathcal{N} , is plotted. As \mathcal{N} is increased $g^{(2)}(0)$ becomes larger since more excitations can be supported inside the medium. Due to the finite storage efficiency $g^{(2)}(0)$ also depends on the mean photon number of the incident probe pulse. At large probe powers where the number of excitations in the medium has saturated (black points), the value of $g^{(2)}(0)$ approaches that of a photon number state with \mathcal{N} excitations (see equation 4.6). However, for lower probe powers (blue points) the effect of the truncation of the coherent state is not as dramatic and the distribution of stored photons inside the medium is closer to Poissonian. Therefore $g^{(2)}(0)$ is larger in this case. In figure 7.9 (b) the dependence of $g^{(2)}(0)$ on the mean photon number of the incident probe pulse is plotted for a fixed value of \mathcal{N} . Note that the variation of $g^{(2)}(0)$ with storage efficiency for a fixed probe power follows a similar trend. The value of $g^{(2)}(0)$ initially drops as the mean photon number of the probe

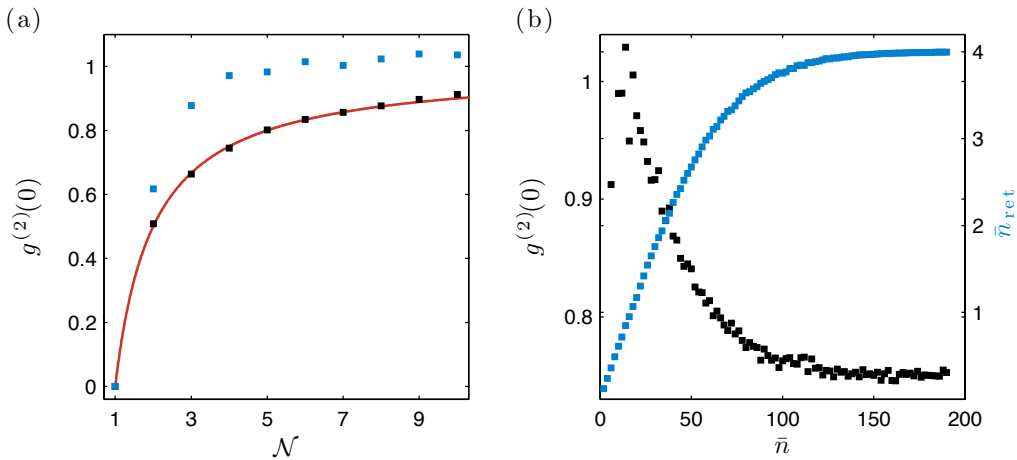


Figure 7.9: $g^{(2)}(0)$ predicted by Monte-Carlo model. (a) Dependence on number of blockade spheres, \mathcal{N} . The variation of $g^{(2)}(0)$ is plotted for mean probe photon numbers of 200 (black) and 20 (blue). The red line corresponds to a photon number state with \mathcal{N} excitations. The storage efficiency used in the calculation is $\eta_{\text{store}} = 6\%$. (b) Dependence of $g^{(2)}(0)$ on the mean photon number of the probe pulse, \bar{n} (black). The mean number of retrieved photons, \bar{n}_{ret} , is also plotted (blue). The number of blockade spheres and the storage efficiency used in the calculation are $\mathcal{N} = 4$ and $\eta_{\text{store}} = 6\%$ respectively. For simplicity, $\eta_{\text{ret}} = 100\%$.

pulse increases, before leveling off when the medium becomes saturated.

7.4.2 Observation of quantum states of light

Experimental measurements of the photon statistics of the retrieved field will now be presented. All of the $g^{(2)}$ measurements have been corrected for the finite background signal shown in figure 7.1, using equation 4.9, unless stated otherwise. Each $g^{(2)}$ measurement typically uses data accumulated from around 1×10^7 store/retrieve cycles. Figure 7.10 (a) shows $g^{(2)}$ as a function of time delay between the two single-photon detectors for the $80s$ Rydberg state. The entire retrieved field has been binned, as highlighted in figure 7.1. Each bar in figure 7.10 (a) is therefore $6 \mu\text{s}$ in width, corresponding to the repetition rate of the experiment. The strong suppression of $g^{(2)}$ at $\tau = 0$ is a signature of dipole blockade [19, 20], and provides evidence of strong photon-photon interactions [108]. In the absence of photon interactions $g^{(2)}$ should be 1. It can be seen that $g^{(2)}(\tau \neq 0)$ is greater than one indicating bunching of the retrieved field. The reason for this is discussed shortly. The variation of $g^{(2)}(0)$ with principal quantum number, n , is plotted in figure

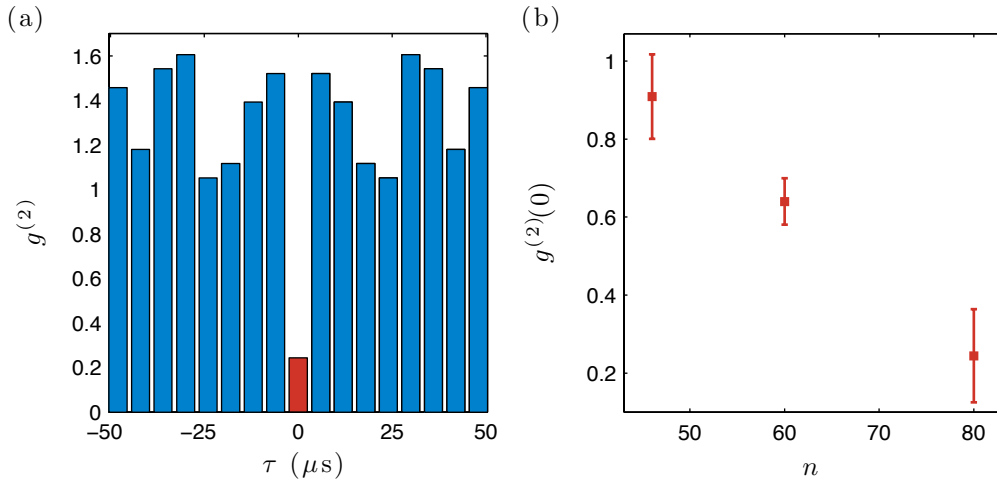


Figure 7.10: Measurements of $g^{(2)}$, where the entire retrieved field has been binned. (a) $g^{(2)}$ of the retrieved field as a function of time delay, τ . For this data set photons were stored in the $80s_{1/2}$ Rydberg state. (b) $g^{(2)}(0)$ of the retrieved field for storage in different $ns_{1/2}$ Rydberg states.

7.10 (b). As n is increased the blockade radius becomes larger and therefore the number of photons that can be stored inside the medium is reduced. Consequently $g^{(2)}(0)$ falls with increasing n . The fact that $g^{(2)}(0)$ does not fall to zero shows that multiple excitations can be stored inside the medium for the Rydberg states studied.

The data presented in figure 7.8 shows that in order to reach the regime where the number of stored photons approaches saturation, $\bar{n} \gtrsim 100$. However, working at these probe powers is accompanied by large decay rates in the storage efficiency as shown in figure 7.2. This means there is less time available per experimental cycle to accumulate data. As a compromise the $g^{(2)}$ data in figure 7.10 was measured at a probe power of approximately 4 pW ($\bar{n} \approx 28$). In figure 7.11 (a), $g^{(2)}(0)$ is plotted for different probe powers for the 60s Rydberg state. It can be seen that there is no significant variation in $g^{(2)}(0)$ when in the saturated and non-saturated regimes, contradicting the results of the Monte-Carlo model presented in figure 7.9 (b). The discrepancy could be due to the fact that the Gaussian density distribution of the medium and the tight focusing of the probe beam have been ignored. As a consequence of both of these factors, it is more likely to store photons in the

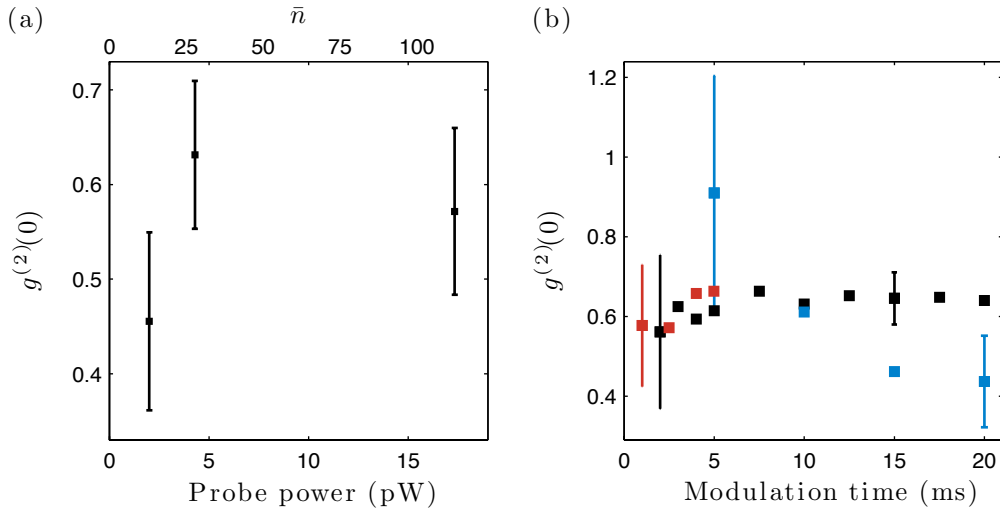


Figure 7.11: Dependence of $g^{(2)}(0)$ on probe power for the 60s Rydberg state. (a) Variation of $g^{(2)}(0)$ when in the saturated and non-saturated regimes. (b) Variation of $g^{(2)}(0)$ with trap modulation time for $\bar{n} = 13$ (blue), $\bar{n} = 28$ (black), and $\bar{n} = 112$ (red).

center of the cloud rather than at the edges. This could mean that for low probe powers \mathcal{N} is effectively reduced, and therefore there is still significant truncation of the initial coherent state, resulting in a suppression of $g^{(2)}(0)$. One would expect that for a sufficiently weak probe pulse, e.g. where $\bar{n} \ll 1$, $g^{(2)}(0)$ would not be suppressed since dipole blockade would have no effect on the photon statistics. However, it was not possible to study this regime due to its inherently low signal to noise.

Assuming that $\mathcal{N} = 4$ for the $n = 60$ Rydberg state, the Monte-Carlo model predicts that $g^{(2)}(0) = 0.75$ in the saturated regime. This is significantly larger than the measured values shown in figure 7.11 (a). For the $80s_{1/2}$ Rydberg state the blockade radius should increase by a factor of approximately 1.7. For $\mathcal{N} = 2$ the model predicts that $g^{(2)}(0) = 0.5$, which is again significantly larger than the measured value of $g^{(2)}(0) = 0.24 \pm 0.12$. The model therefore fails to accurately predict the modification of the photon statistics due to dipole blockade. This could be due to the fact that the model does not take into account polariton correlations within the medium [20, 107]. Since each Rydberg excitation must be separated by R_o , one would expect this restriction to reduce the probability of storing multiple photons inside the cloud. In other words, the probability of storing two photons is not simply the probability of storing one photon squared. The polariton correlations would be expected to reduce the values of $g^{(2)}(0)$ relative to those obtained from the model [107]. In addition the interaction between neighboring polaritons during the storage interval has been neglected. These have been observed to cause dephasing when multiple polaritons are written into a sample [115]. Dephasing would make it more likely to retrieve single stored photons than multiple stored photons, which would again reduce $g^{(2)}(0)$. The effects of dephasing are discussed in more detail in the next chapter.

In figure 7.11 (b) $g^{(2)}(0)$ is plotted as a function of the trap modulation time for different probe powers. For the medium power (black) and high power (red) data $g^{(2)}(0)$ remains roughly constant over the time ranges considered. For the low power data (blue), $g^{(2)}(0)$ seems to decrease at short modulation times. This behavior is not understood. However the error bars on the data at short modulation times are quite large, therefore it is difficult to draw any reliable conclusions.

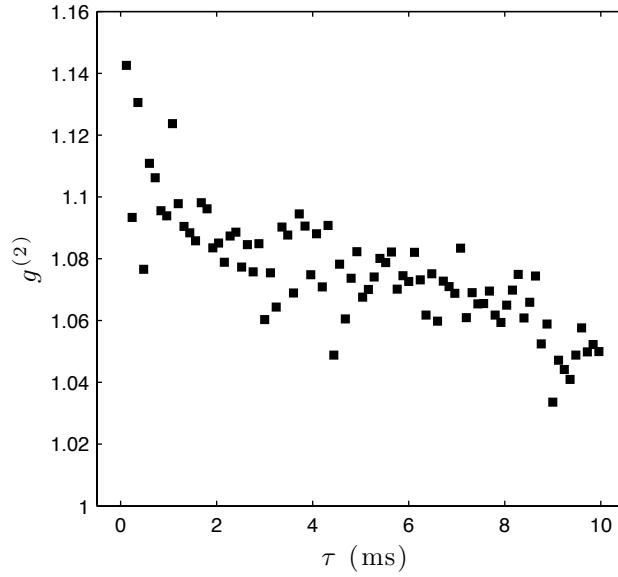


Figure 7.12: Variation of $g^{(2)}$ away from $\tau = 0$. As τ increases $g^{(2)}$ falls steadily.

In figure 7.10 (a) it was seen that for cross-correlations performed between different retrieved pulses, i.e. for $\tau \neq 0$, $g^{(2)}$ was greater than 1. This indicates bunching of the retrieved photon signal. This most likely arises due to the variation in the retrieved signal with trap modulation time as shown in figure 7.2. The variation of $g^{(2)}$ away from $\tau = 0$ is studied more closely in figure 7.12. Each point is an average of twenty store/retrieve cycles. It can be seen that as the time delay increases $g^{(2)}$ falls steadily. The stronger bunching at short time delays could be because of the large variation in the retrieved signal at short modulation times (see figure 7.2(a)). Note that $g^{(2)}$ never falls to 1 since the retrieved signal is constantly varying, even at long modulation times.

7.4.3 Preliminary evidence for a photon number dependent group delay

So far when calculating $g^{(2)}$ the entire retrieved pulse has been binned. However, since the Rydberg excitations must be separated by a distance $R \geq R_o$, one may expect this to be evident in the temporal photon correlations within each retrieved pulse. To examine this $g^{(2)}(0)$ is calculated for different regions

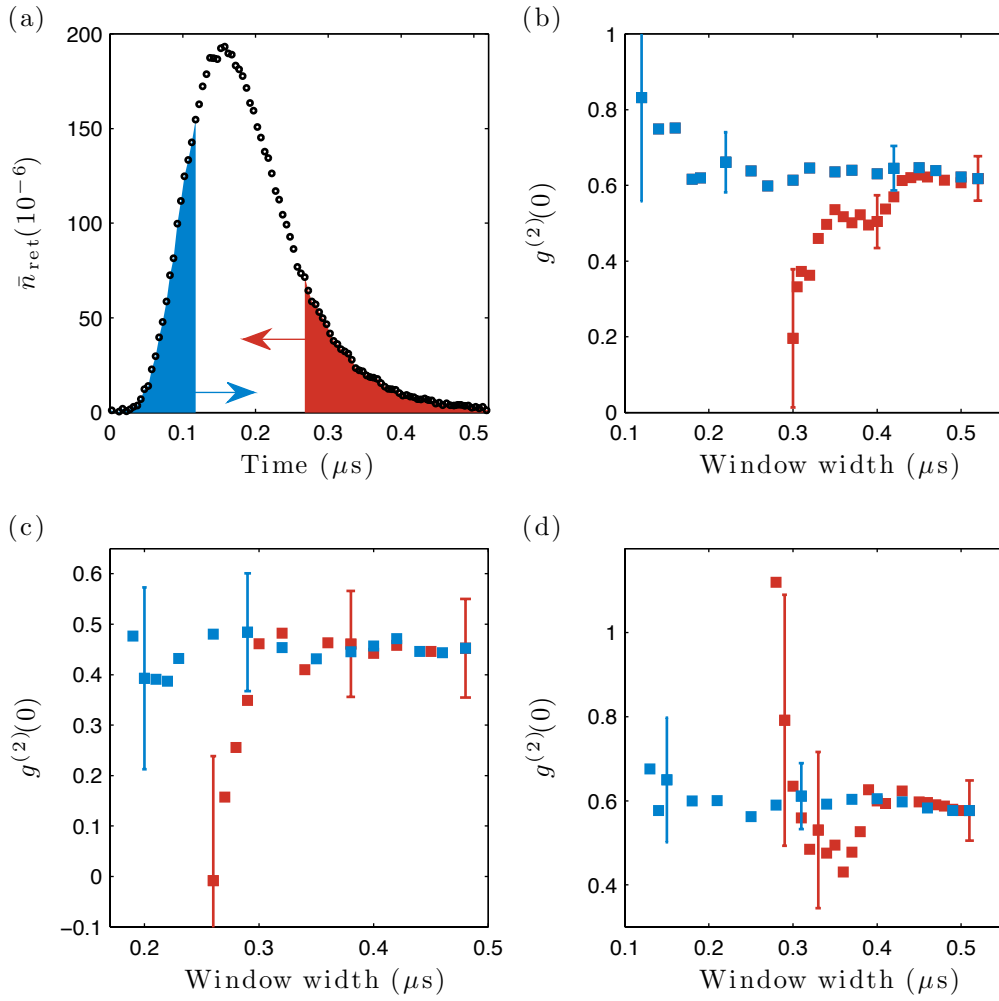


Figure 7.13: Variation of $g^{(2)}(0)$ across the retrieved pulse. (a) Illustration of the analysis windows over which photons from the retrieved pulse are correlated. The red window extends from the trailing edge of the pulse towards the left, whereas the blue window extends from the leading edge of the pulse to the right. The variation of $g^{(2)}(0)$ for different probe powers as the width of the analysis windows are varied is plotted in (b)-(d). (b) $\bar{n} = 28$. (c) $\bar{n} = 13$. (d) $\bar{n} = 112$.

of the retrieved pulse. The results are shown in figure 7.13.

In figure 7.13 (a) examples of the analysis windows over which the retrieved pulse is studied are highlighted. All photon counts outside a given analysis window are ignored. The width of the window is varied, starting from one edge of the pulse and moving towards the other edge. The windowing process is considered starting from both sides of the pulse, shown by the separate

blue and red regions.

In figure 7.13 (b) $g^{(2)}(0)$ is plotted for different window widths for a mean photon number of approximately $\bar{n} = 28$ per probe pulse. First the case where the width of the analysis window is extended starting from the trailing edge of the retrieved pulse (red data points) will be considered. It can be seen that the variation of $g^{(2)}(0)$ exhibits a step-like structure, decreasing quickly as the width of the analysis window is reduced. However, when extending the window width starting from the leading edge of the pulse (blue data points), the variation in $g^{(2)}(0)$ is remarkably different. In this case $g^{(2)}(0)$ remains roughly constant before increasing for small window widths.

In figures 7.13 (c) and (d) the analysis procedure is repeated for weaker and stronger probe powers respectively. The variation in $g^{(2)}(0)$ in these cases is very different, highlighting the potential importance of the stored photon number distribution on the observed effect.

To gain some insight into the origin of the observed variation in $g^{(2)}(0)$ we must consider the effect of dipole blockade on the group delay of the probe light. Due to the collective nature of the Rydberg excitations, modes with different photon numbers experience different group delays. This is because the optical depth experienced by each photon depends on the number of photons in the medium. A single photon which collectively excites N atoms drives the Rydberg transition with a Rabi frequency enhanced by a factor of \sqrt{N} compared to the case of single atom excitation [62]. The optical depth, and therefore the group index, is enhanced by a factor of N . However when two Rydberg excitations are created, the two probe photons must be separated during propagation by a distance R_o . Therefore each photon collectively excites a smaller number of atoms, meaning that the enhancement of the optical depth is not as large. This can be modeled phenomenologically by taking Gaussian mode functions of the form [116]

$$f(t, n) = \frac{1}{\sqrt{\pi}(5-n)\sigma} \exp\left(-\frac{(t - (5-n)\tau - \tau_0)^2}{2((5-n)\sigma)^2}\right). \quad (7.3)$$

Here n is the photon number of the mode, σ is a width parameter such that $(5-n)\sigma$ is the standard deviation of the mode, τ is a parameter controlling the time delay between different modes, and τ_0 is a time offset used for fitting

purposes. It is assumed that only modes containing up to four photons contribute (due to dipole blockade). The propagating light field is taken to be in a mixed state containing these four modes. It is also assumed that the time separation and width of the modes is linear in n . This is equivalent to assuming that the medium has a uniform density distribution.

Equation 7.3 is used to generate retrieved pulse shapes, from which the variation of $g^{(2)}(0)$ across the pulse can be calculated. Using σ , τ , and τ_0 as free parameters, the pulse shape and variation of $g^{(2)}(0)$ are simultaneously fit to the experimental data. In addition, fit parameters representing the weight of each mode, $P(n)$, are allowed to vary. These weights determine the relative contribution of each mode to the shape of the retrieved pulse. In figure 7.14 (a) the retrieved pulse for $\bar{n} = 28$ is fitted. Each of the four modes which sum to give the fit are also plotted, along with their weights. It can be seen that the different shape and delay of each mode gives rise to the asymmetry of the retrieved pulse. In figure 7.14 (b) the values of $g^{(2)}(0)$ predicted by the model (red and blue lines) are plotted. It can be seen that

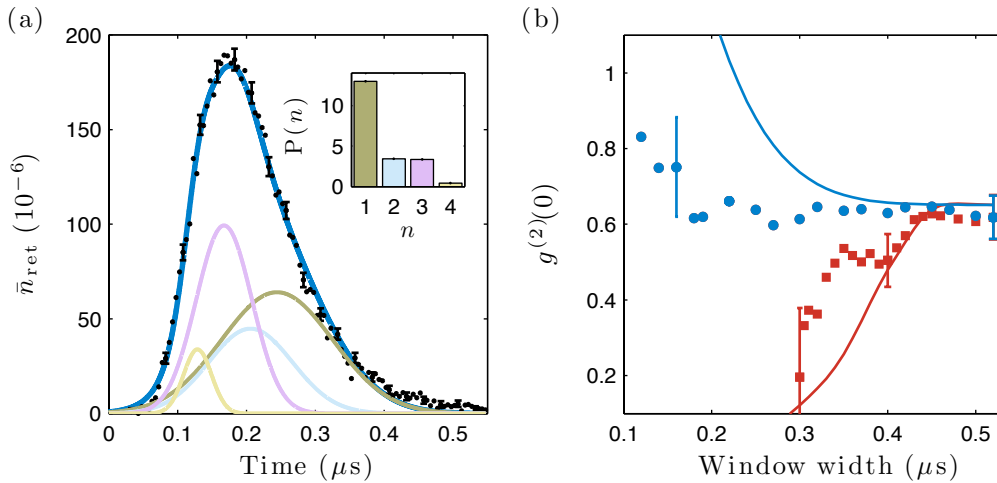


Figure 7.14: Retrieved pulse shape and variation of $g^{(2)}(0)$ across the pulse, fitted using a model which assumes a photon number dependent group delay. (a) The fit to the retrieved pulse (dark blue line) is formed from the sum of four modes with different photon numbers. Inset: The weight $P(n)$ of each mode used in the fit. (b) The variation of $g^{(2)}(0)$ predicted by the model (blue and red lines). Note that the same fit parameters are used in (a) and (b).

while the model reproduces some of the qualitative features of the data, there is a large discrepancy between the experimental results and the predictions of the model. This is most likely due to the fact that in obtaining equation 7.3 it was assumed that the density distribution of the medium is uniform. The fact that the probe beam has a short Rayleigh range and therefore a non-uniform Rabi frequency across the sample has also been ignored. Both of these simplifying assumptions probably significantly contribute to the large discrepancies observed. A more sophisticated model is therefore required to confirm the observation of the described effects.

The hypothesis of a photon number dependent group delay was proposed after private discussions with C. Ates, S. Bettelli, T. Fernholz, and I. Lesanovsky [116]. It is worth mentioning that photon number dependent group delays have previously been predicted [117] and observed [118] for a system where an ensemble of three-level atoms is strongly coupled to a cavity.

Chapter 8

Coherent control of Rydberg polaritons

The preceding chapter demonstrated the storage and retrieval of photons from a cold atomic gas. As a consequence of dipole blockade, a limit on the maximum number of stored photons was observed. The retrieved field was shown to be antibunched, as demonstrated in [19]. The partial suppression of $g^{(2)}(0)$ measured for Rydberg states in the range $46 \leq n \leq 80$ is consistent with a sample that can support more than one excitation.

It has been proposed that the read-out of multiple photons from an atomic cloud can be suppressed through dephasing of the spin-waves [119, 120]. This involves introducing long-range interactions, for example resonant dipole-dipole interactions, between neighboring excitations. This chapter presents experiments where the states of stored photons are coherently controlled using a microwave field. Photons initially stored in the $60s_{1/2}$ Rydberg state are coupled to a neighboring $n'p_{3/2}$ Rydberg state. Polariton-polariton interactions are observed as a result of the microwave coupling, leading to a modification of the photon statistics of the retrieved field.

8.1 Coherent evolution of polariton state

In the regime of dipole blockade a single Rydberg excitation is shared between all atoms within the corresponding blockade sphere (see section 2.3). Conse-

quently, during the storage process each photon is mapped into a polariton in the collective state [8, 24]

$$|s\rangle = \frac{1}{\sqrt{N}} \sum_{j=1}^N e^{i\phi_j} |s^j\rangle, \quad (8.1)$$

where $|s^j\rangle = |1_1 1_2 \cdots s_j \cdots 1_N\rangle$, N is the number of atoms per blockade sphere, and $\phi_j = \Delta\mathbf{k} \cdot \mathbf{r}_j$. Here s represents an $ns_{1/2}$ Rydberg excitation, and 1 corresponds to the ground state. As discussed in section 3.2.2, the phase factors ϕ_j are responsible for the directionality of the retrieved field. The effective wave vector of the spin-wave is $\Delta\mathbf{k}$, and \mathbf{r}_j is the position of atom j .

The state of each polariton can be controlled by applying a field resonant with a neighboring Rydberg state. For example, a microwave field resonant with the state $n'p_{3/2}$, as illustrated in figure 8.1 (a), couples $|s\rangle$ to

$$|p\rangle = \frac{1}{\sqrt{N}} \sum_{j=1}^N e^{i\phi_j} |p^j\rangle. \quad (8.2)$$

Here $|p^j\rangle = |1_1 1_2 \cdots p_j \cdots 1_N\rangle$, where p denotes an $n'p_{3/2}$ Rydberg excitation. The $p_{3/2}$ state is used in all experiments described in this chapter. This is because one eigenstate of the resonant dipole-dipole interaction potential for the $p_{1/2}$ state has zero interaction energy [52]. Figure 8.1 (b) illustrates the experimental procedure for photon storage and the subsequent state control of the Rydberg polaritons. The procedure is identical to that shown in figure 7.1 (b) except that now a microwave pulse is applied during the storage interval.

The retrieved field now depends on the final state of the polaritons after the state evolution driven by the microwave field. First we will consider \mathcal{N} independent polaritons, in the absence of any dephasing mechanisms. The microwave field coherently couples the two polariton states $|s\rangle$ and $|p\rangle$. Each polariton can therefore be considered an effective two level system, analogous to a spin- $\frac{1}{2}$ particle. Similar to the case of a two-level atom undergoing Rabi oscillations described in section 3.1.1, the state evolution is determined by the rotation angle, Θ . Here the rotation angle is given by $\Theta = \Omega_\mu t$, where Ω_μ is the Rabi frequency of the microwaves and t is the duration of the

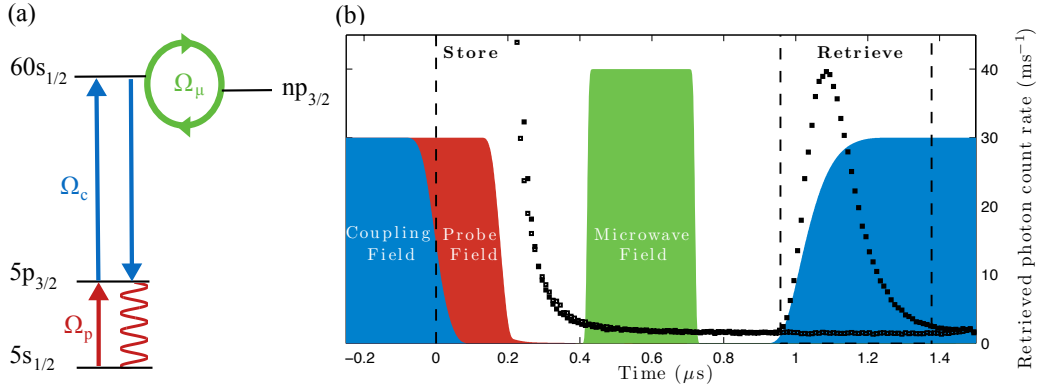


Figure 8.1: Quantum state control of stored photons. (a) The level scheme used to couple photons stored in the $60s_{1/2}$ Rydberg state to a neighboring $n'p_{3/2}$ Rydberg state with a microwave field. (b) Experimental pulse sequence. A microwave pulse of duration 150 ns - 300 ns is applied during the storage interval. Other than the additional microwave field, the sequence is identical to that in figure 7.1 (b).

microwave pulse. There is however an important distinction between the Rabi oscillations of \mathcal{N} Rydberg polaritons in this experiment, and those of a single two-level atom driven by optical frequency radiation. This arises due to the long wavelength of the microwave driving field (typically around 1.5 cm), which is much larger than the extent of the atomic cloud (of the order of $40 \mu\text{m}$). A consequence of this is that the phase structure of each polariton is conserved. In addition, the microwave field does not resolve individual polaritons. Instead, it collectively addresses the whole sample. Therefore under microwave coupling an \mathcal{N} -particle Dicke state is formed. Prior to the microwave pulse the collective polariton state is $|s_1 s_2 \dots s_{\mathcal{N}}\rangle$, which can be written $|J = \mathcal{N}/2, M = -\mathcal{N}/2\rangle$. The evolution from this state to the Dicke state $|J, M'\rangle$ is given by the Wigner rotation matrix \mathcal{D} [121]. To find the retrieval probability, P , the final state is set equal to the initial state in the Wigner rotation matrix. The retrieval probability oscillates as a function of Θ according to [21]

$$P = \left[\cos^2 \left(\frac{\Theta}{2} \right) \right]^{\mathcal{N}}. \quad (8.3)$$

It has been assumed that population can only be read from the initial state, $|s_1 s_2 \dots s_{\mathcal{N}}\rangle$. The justification for this follows from considering the interaction

between neighboring polaritons, which have been ignored so far. Coupling $|s\rangle$ to $|p\rangle$ introduces resonant dipole-dipole interactions between polaritons [51, 119]. The interaction energy is given by

$$V_{\text{dd}}(R_o) = \frac{d^2}{4\pi\epsilon_0 R_o^3}, \quad (8.4)$$

where d is the electric dipole moment of the Rydberg transition, and R_o is the blockade radius associated with the optical excitation during the polariton formation (see equation 6.2). Since resonant dipole-dipole interactions have a longer range than the van der Waals interactions responsible for the separation of the polaritons, application of the microwave field can introduce polariton-polariton interactions. These interactions are expected to disturb the phase structure of each polariton [119, 120]. Due to the finite time (typically of order 200 ns - 350 ns) between the microwave pulse and the read-out stage, Dicke states with a p component should dephase due to dipole-dipole interactions between the polaritons. Therefore only the initial state can be retrieved from the sample in the phase matched direction.

Equation 8.3 does not take into account dephasing of the polariton modes occurring *during* the microwave pulse, i.e. during the evolution between $|s\rangle$ and $|p\rangle$. This would reduce the retrieval probability and therefore the amplitude of the Rabi oscillations. This is discussed further in section 8.3.

8.2 Weakly-Interacting Regime

An obvious starting point in observing Rabi oscillations between the states $|s\rangle$ and $|p\rangle$ is to work in a regime where the interaction between neighboring polaritons is weak. From equation 8.4 it can be seen that given the initial $60s_{1/2}$ Rydberg state and therefore fixed R_o , the only controllable parameter is d , the dipole moment between the microwave coupled states. Since the dipole moment between adjacent Rydberg states scales as Δn^{-2} , the interaction strength can be tuned through the choice of the $n'p_{3/2}$ Rydberg state. This choice was limited in practice by the range of microwave frequencies that could propagate through the waveguide used. Microwaves at 56.3 GHz were used to couple the $60s_{1/2}$ state to the $58p_{3/2}$ state. The dipole moment for this transition is $\sqrt{2/9} \times 468 ea_0$ (all dipole moments are calculated using

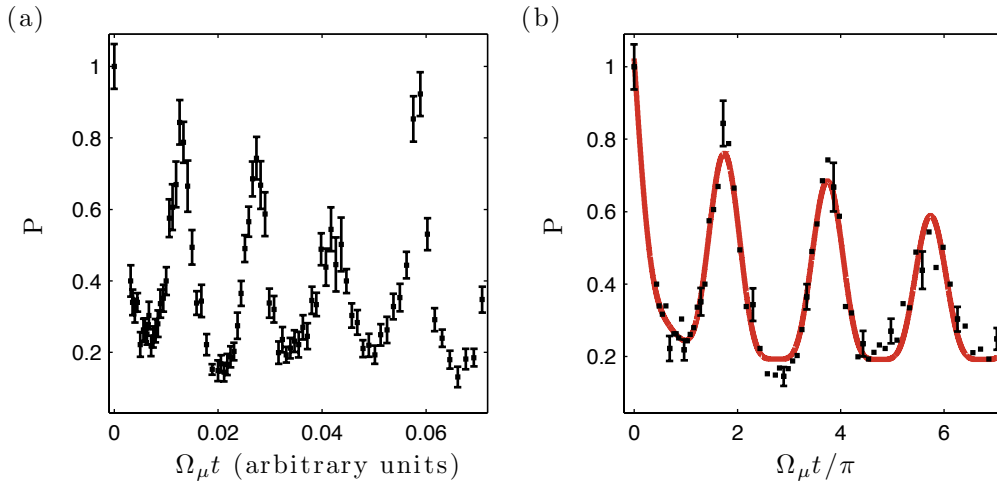


Figure 8.2: Rabi oscillations of polaritons between the $60s_{1/2}$ and $58p_{3/2}$ Rydberg states. (a) Unfitted data. The microwave Rabi frequency increases linearly from left to right, with the microwave pulse duration fixed. The retrieval probability, P , is normalised to the case where no microwave field is applied i.e. $P(\Omega_\mu t = 0) = 1$. (b) The first three oscillations are fit to the function given by equation 8.5. The fit is used to calibrate the rotation angle $\Theta = \Omega_\mu t$. The mean number of retrieved polaritons is a fit parameter, with $\mathcal{N} = 2.4 \pm 0.2$ for this data set.

the Numerov method by J. D. Pritchard [47]). Figure 8.2 (a) shows Rabi oscillations between these states. In order to map out the Rabi oscillations the microwave power is varied, keeping the duration of the microwave pulse fixed at 150 ns. In principle the duration of the microwave pulse could be varied, leaving the microwave power fixed. However, this cannot be done with sufficiently high resolution with the microwave generator used. The measured retrieval probability, P , is given by the number of retrieved photons normalised to the case where no microwave field is applied.

In figure 8.2 (b) the data is fit phenomenologically to the function

$$P = C_0 + C_1 \left[\cos^2 \left(\frac{C_2 x + C_3}{2} \right) \right]^{C_4} \times [1 + \tanh(C_5(x - C_6))] + C_7 \exp(-C_8 x). \quad (8.5)$$

The second term is equivalent to equation 8.3 combined with a tanh envelope.

There are eight free parameters denoted C_i , with the independent variable x proportional to the rotation angle. The fit parameter C_4 is equal to the number of *retrieved* polaritons. This will be denoted \mathcal{N} in the remainder of this thesis. Since the data is accumulated over many experimental realisations this represents the mean value. From the fit $\mathcal{N} = 2.4 \pm 0.2$. Unless stated otherwise this function is used to fit Rabi oscillation data throughout this thesis.

Since $\mathcal{N} > 1$, the data provides evidence for the collective nature of the Rabi oscillations predicted by equation 8.3. The dipole-dipole interactions between the polaritons after application of the microwave pulse, prior to read-out, must therefore be significant. If this was not the case then the $|s_1 s_2 \dots s_{\mathcal{N}}\rangle$ state would not be preferentially retrieved (see section 8.1). However, the fact that most of the Rabi oscillations have a high visibility suggests that the interactions do not lead to significant dephasing *during* the period of microwave coupling. In other words, it is possible to return to the state $|s_1 s_2 \dots s_{\mathcal{N}}\rangle$ with high fidelity.

It can be seen that the retrieval probability does not fall to 0 at the troughs of the oscillations. This is not fully understood, although it could be because light is collected from a large solid angle by the lens in the vacuum chamber. Light that is not in the phase-matched mode could therefore be partially collected.

The role of the interaction between polaritons *during* the period of microwave coupling will now be examined.

8.3 Strongly-Interacting Regime

To increase the resonant dipole-dipole interaction strength between polaritons, a closer-lying $n'p_{3/2}$ Rydberg state is used. Microwaves at 18.5 GHz couple the $60s_{1/2}$ state to the $59p_{3/2}$ state. The dipole moment for this transition is $\sqrt{2/9} \times 3468 ea_0$. Since the resonant dipole-dipole interaction scales as d^2 , the interaction energy is roughly 55 times larger for this transition compared with the transition to the $58p_{3/2}$ state. Unless stated otherwise the $59p_{3/2}$ state is considered in the remainder of this chapter.

8.3.1 Interaction induced dephasing

Figure 8.3 shows Rabi oscillations for the case of microwave coupling to the $59p_{3/2}$ state. The Rabi oscillations exhibit remarkably different behavior to those shown in figure 8.2. It can be seen that the amplitude of the oscillations is strongly suppressed at small values of Ω_μ , while the oscillations revive at large Ω_μ . As will be discussed below, resonant dipole-dipole interactions between the polaritons *during* the period of microwave coupling are responsible for the strong suppression of the Rabi oscillations.

The behavior of the Rabi oscillations in figure 8.3 can be understood by introducing a second blockade scale associated with the microwave transition [51]

$$R_\mu = \left(\frac{C_3}{\hbar\Omega_\mu} \right)^{\frac{1}{3}}. \quad (8.6)$$

Here C_3 is the resonant dipole-dipole interaction coefficient. The microwave blockade radius, R_μ , gives the length scale over which resonant dipole-dipole

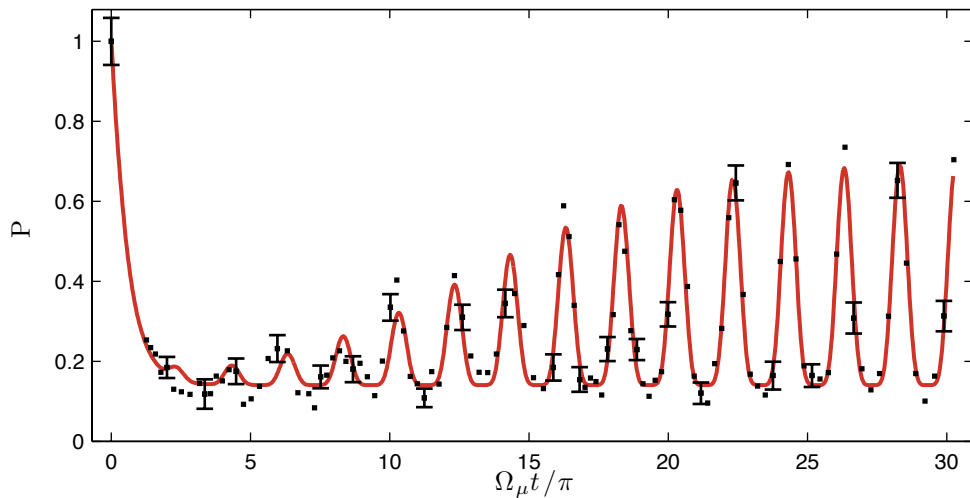


Figure 8.3: Rabi oscillations of polaritons between the $60s_{1/2}$ and $59p_{3/2}$ Rydberg states. The microwave pulse duration is 300 ns. The amplitude of the Rabi oscillations is strongly suppressed at low Ω_μ due to interaction-induced dephasing of the polaritons. This occurs due to resonant energy exchange between the dipole-coupled states. At large Ω_μ the degeneracy between the dipole-coupled states is lifted and the microwave driving is large compared to the dipole-dipole interaction between polaritons. From the fit $\mathcal{N} = 2.8 \pm 0.2$.

interactions dominate the microwave driving. Varying Ω_μ changes the ratio R_μ/R_o .

The left hand side of figure 8.3 corresponds to $\hbar\Omega_\mu < V_{\text{dd}}$, i.e. $R_\mu > R_o$. In this regime there is strong dephasing of the polaritons due to dipole-dipole interactions. This is manifest as a fast exponential decay of the retrieval probability, followed by small amplitude Rabi oscillations for increasing Ω_μ .

The right hand side of figure 8.3 corresponds to $\hbar\Omega_\mu > V_{\text{dd}}$, i.e. $R_\mu < R_o$. In this regime the amplitude of the Rabi oscillations increases before saturating at large Ω_μ . The revival in the oscillations occurs because the dipole-dipole interactions only weakly perturb the microwave driving.

The interplay between the dipole-dipole interactions and the microwave driving can be more clearly understood by considering the interaction Hamiltonian for the system. Considering the polaritons as localised spin- $\frac{1}{2}$ particles separated by a distance R_o , the Hamiltonian can be written [21]

$$H = \frac{\Omega_\mu}{2} \sum_{i=1}^N \mu_i^z + V_{\text{dd}} \sum_{\langle ij \rangle} (\mu_i^+ \mu_j^- + \mu_i^- \mu_j^+ - 2\mu_i^z \mu_j^z). \quad (8.7)$$

Here $\mu^{z,\pm}$ is the dipole operator for $\Delta m = 0, \pm 1$ transitions, and i and j refer to nearest neighbor polaritons. The microwave field is assumed to drive π -transitions. The eigenvalues of this Hamiltonian for two polaritons as a function of their separation are plotted in figure 8.4. The calculations were performed using code written by J. D. Pritchard.

The dipole-dipole interaction term in equation 8.7 leads to mixing of the eigenvalues, which correspond to different angular momentum states. For weak driving, as in figure 8.4 (a), the eigenvalues are strongly mixed in the vicinity of R_o . This leads to excitation exchange between polaritons [122, 123]. However as Ω_μ is increased, for example as in 8.4 (b), the states are split and mixing occurs at smaller polariton separations. To understand the origin of the dephasing it is necessary to note that in reality the polaritons are not localised. The V_{dd} term in equation 8.7 should therefore be replaced by a sum over all interacting atom pairs from each polariton, $V_{\text{dd}}^{p,q}$. Since the separation, and therefore $V_{\text{dd}}^{p,q}$, of each atom pair is different, each pair has a different excitation exchange term. The net effect is that the phase structure

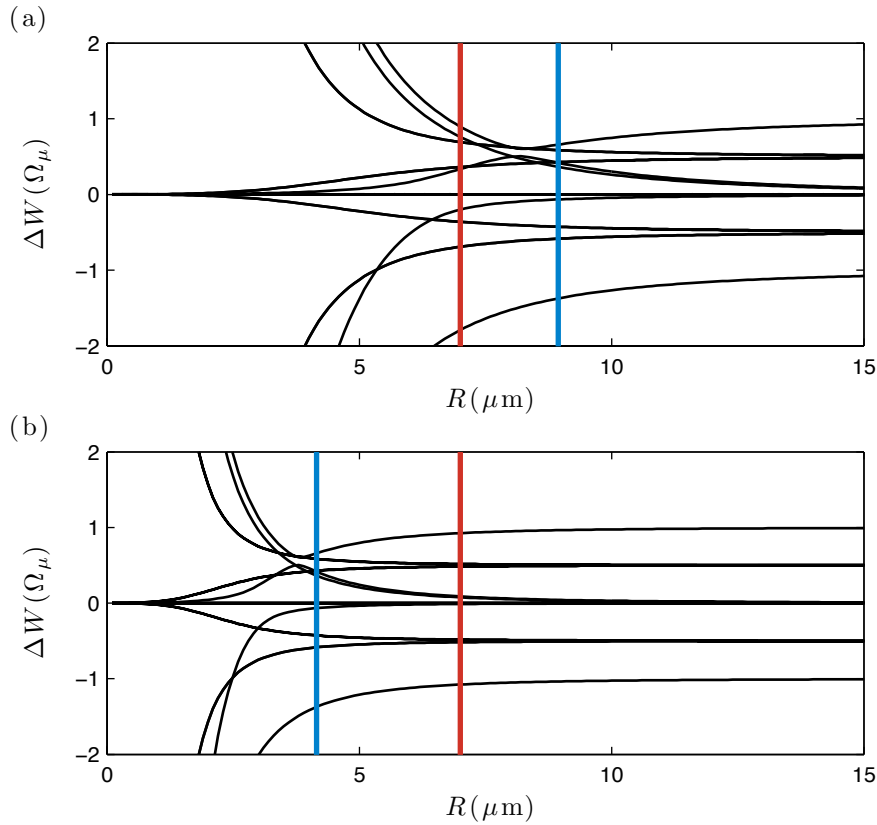


Figure 8.4: Eigenvalues of polariton Hamiltonian 8.7 for two polaritons separated by a distance R . (a) $\Omega_\mu/2\pi = 20$ MHz. (b) $\Omega_\mu/2\pi = 200$ MHz. The red line is located at $R = R_o$, and the blue line is located at $R = R_\mu$. Calculated by J. D. Pritchard.

of each polariton is not conserved and therefore the directionality of the read-out is degraded. This leads to the reduced retrieval probability in the dephasing regime. The retrieval probability does not reach 1 at large Ω_μ since the influence of the dipole-dipole interactions does not vanish completely.

8.3.2 Modification of photon statistics

It has been proposed that the dephasing induced by dipole-dipole interactions between polaritons can suppress the retrieval of states with more than one photon [119, 120]. This relies on the emission of multiple photon states being outside the phase matched mode. The number of polaritons created should follow the Poissonian distribution of the probe input pulse (with an

upper limit determined by the blockade condition). Dephasing can only occur when multiple polaritons are written into the sample. In some experimental realisations only one polariton will be formed. In these cases no interaction induced dephasing can occur, and ideally a single photon should be retrieved. If the dephasing process is effective in destroying the directionality of the read-out, then there should be an excess of single photons retrieved relative to multi-photon retrievals.

To see whether this is reflected in the collective read-out of the polaritons, the value of \mathcal{N} is studied for different ranges of Ω_μ . Each peak of the Rabi oscillations in figure 8.5 (a) is fit individually over a range defined by a sliding window to extract a value of \mathcal{N} . Note that the tanh envelope and the exponential term are dropped when fitting the individual peaks. The peak centered at roughly $\Omega_\mu t = 3\pi$ is not included since the exponentially decaying part of the fit to the entire data set still has a significant contribution in this range.

In figure 8.5 (b) it can be seen that the value of \mathcal{N} increases steadily with Ω_μ . The first Rabi oscillation gives a value of \mathcal{N} close to 1, supporting

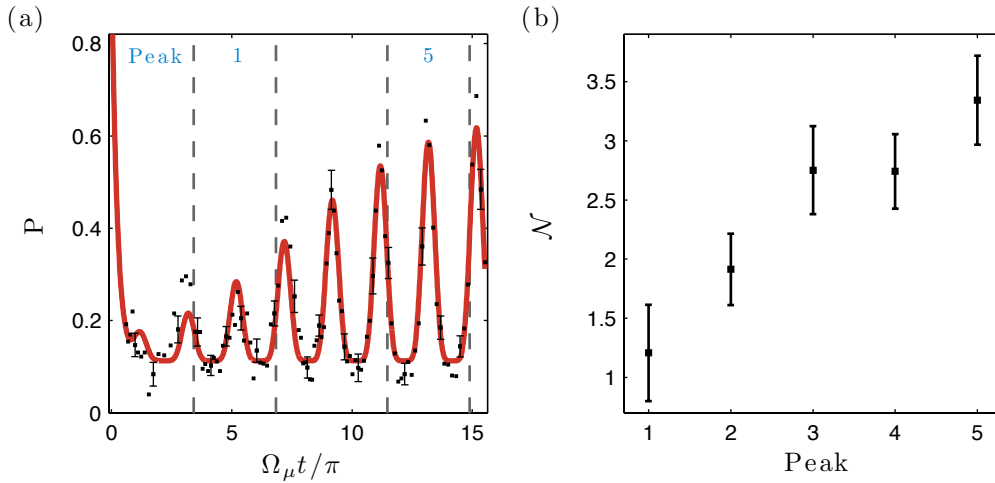


Figure 8.5: Variation of \mathcal{N} over different ranges of Ω_μ . (a) High resolution Rabi oscillation data using a microwave pulse length of 150 ns. Fitting the full data set gives $\mathcal{N} = 3.0 \pm 0.2$. The dashed vertical lines show the sliding window over which each peak is fitted individually. (b) Value of \mathcal{N} extracted from fit of each individual peak.

the hypothesis that only single excitations are retrieved in the dephasing regime. This is also reflected in the photon statistics of the retrieved field as discussed below. As Ω_μ is increased the dephasing of the polaritons is reduced and \mathcal{N} increases. The value of \mathcal{N} obtained in the regime of strong microwave driving should therefore reflect the mean number of polaritons in the sample. The maximum value of \mathcal{N} observed is around 3. This is realistic given the geometry of the system and the size of the blockade radius, R_o .

Since the microwave field has been shown to suppress the retrieved photon signal for $\hbar\Omega_\mu < V_{dd}$, it is interesting to examine whether there is an associated change in the photon statistics of the retrieved field. In the ideal case where only single excitations contribute to the read-out, $g^{(2)}(0)$ should be strongly suppressed [119]. To determine whether the retrieved photon signal shows enhanced anti-bunching, $g^{(2)}$ was measured in the regime of weak mi-

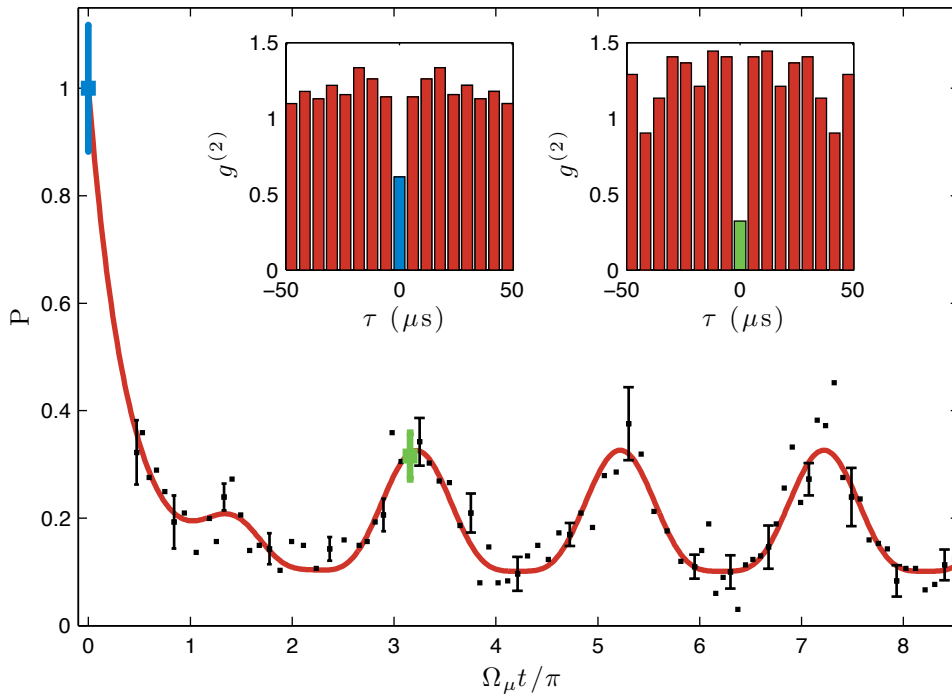


Figure 8.6: Measurement of $g^{(2)}$ of the retrieved field at two different points on the Rabi oscillation curve. When no microwave coupling is applied (blue), $g^{(2)}(0) = 0.62 \pm 0.06$. After weak microwave coupling (green), $g^{(2)}(0) = 0.32 \pm 0.18$. Dephasing of the polaritons due to interactions induced by the microwave field suppresses the retrieval of multiple photons.

crowave coupling. In figure 8.6, $g^{(2)}$ is plotted for two different points on the Rabi oscillation curve. When no microwave coupling is applied (blue point) $g^{(2)}(0) = 0.62 \pm 0.06$. After a weak microwave pulse is applied (green point), with a rotation angle corresponding to the peak of a Rabi oscillation, the value of $g^{(2)}(0)$ decreases. For the point highlighted $g^{(2)}(0) = 0.32 \pm 0.18$. The enhanced anti-bunching of the retrieved field therefore supports the theory that single Rydberg excitations are preferentially retrieved from the sample in the regime where interaction induced dephasing of the polaritons occurs.

A similar measurement was performed for microwaves driving the $60s_{1/2}$ to $58p_{3/2}$ transition. In this case after weak microwave coupling $g^{(2)}(0) = 0.51 \pm 0.13$. As expected $g^{(2)}(0)$ is not as strongly suppressed since the interaction between polaritons, and therefore the dephasing, is much weaker.

The variation of $g^{(2)}(0)$ with trap modulation time exhibits interesting behavior in the case where a microwave field is applied. Figure 8.7 (a) shows this variation for the case of no microwave coupling (black), microwave coupling to the $58p_{3/2}$ state (blue), and microwave coupling to the $59p_{3/2}$ state (red). Whereas the variation in $g^{(2)}(0)$ when no microwave field is applied is very small, when a microwave field is applied $g^{(2)}(0)$ clearly increases with

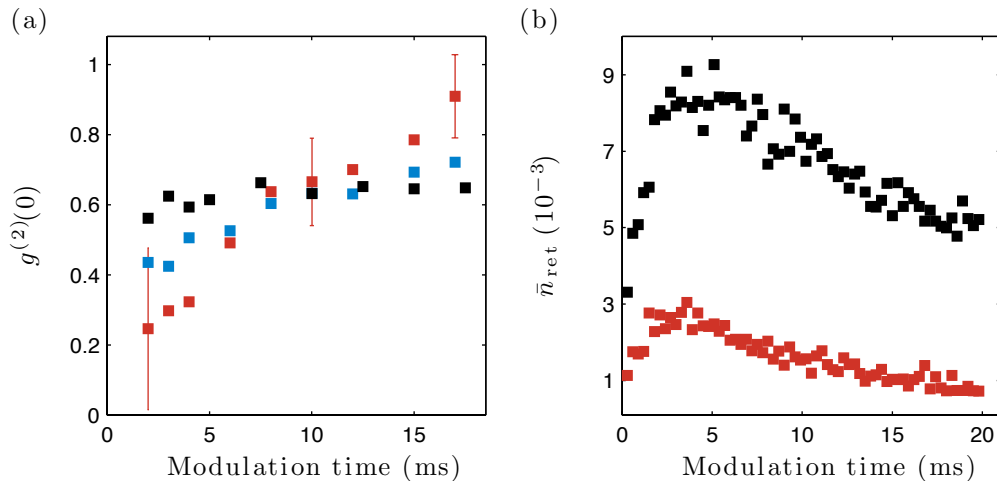


Figure 8.7: Variation in $g^{(2)}(0)$ with trap modulation time. (a) Variation in $g^{(2)}(0)$ for the case of no microwave coupling (black), microwave coupling to the $58p_{3/2}$ state (blue), and microwave coupling to the $59p_{3/2}$ state (red). (b) Variation in mean number of retrieved photons per store/ retrieve cycle, \bar{n}_{ret} , for no microwave coupling (black) and with microwave coupling to the $59p_{3/2}$ state (red).

trap modulation time. This increase is most pronounced for the case of microwave coupling to the $59p_{3/2}$ state. This behavior is not fully understood and further work is required to confirm its origin. However, some insight may be gained by examining the variation in the retrieved photon signal as a function of trap modulation time (also see section 7.1). This is plotted for the case of no microwave coupling (black) and with microwave coupling to the $59p_{3/2}$ state (red) in figure 8.7 (b). It can be seen that the variation in the retrieved signal in both cases is very similar. There is an offset between the signals due to the reduced retrieval probability in the dephasing regime under microwave coupling. The increase of $g^{(2)}(0)$ at short modulation times could be due to the increasing number of photons stored, meaning that there are fewer cases where there are single excitations in the cloud. The reason for the continued increase in $g^{(2)}(0)$ at longer modulation times is not clear. Note that the values of $g^{(2)}(0)$ after microwave coupling quoted above were taken for a trap modulation time of 4 ms.

It is interesting to examine whether there is a change in the retrieved pulse shape after microwave coupling compared to the case where no microwave field is applied. It was proposed in section 7.4.3 that the shape of the retrieved pulse is sensitive to the distribution of photon numbers retrieved from the sample. As the microwave field modifies the photon statistics of the retrieved field, one would expect an associated change in the retrieved pulse shape. In figure 8.8 (a) the retrieved pulses are fitted using equation 7.3 for the cases of no microwave coupling (blue), and with microwave coupling (red) during the storage interval. Note that the experimental data used corresponds to the same data points highlighted in figure 8.6. Each mode contributing to the pulse is also plotted for the case where microwave coupling has been applied. To examine the relative contribution of each mode to the retrieved pulses obtained with and without microwave coupling, the ratio of the weights of each mode are calculated. These are plotted in figure 8.8 (b). As expected the single photon mode, $n = 1$, remains unchanged after microwave coupling. The other modes are all significantly attenuated, with the attenuation increasing for modes with higher photon numbers. Note that these results are preliminary. As shown in section 7.4.3 the model does not reproduce the measured values of $g^{(2)}(0)$. Therefore the accuracy of the inferred photon

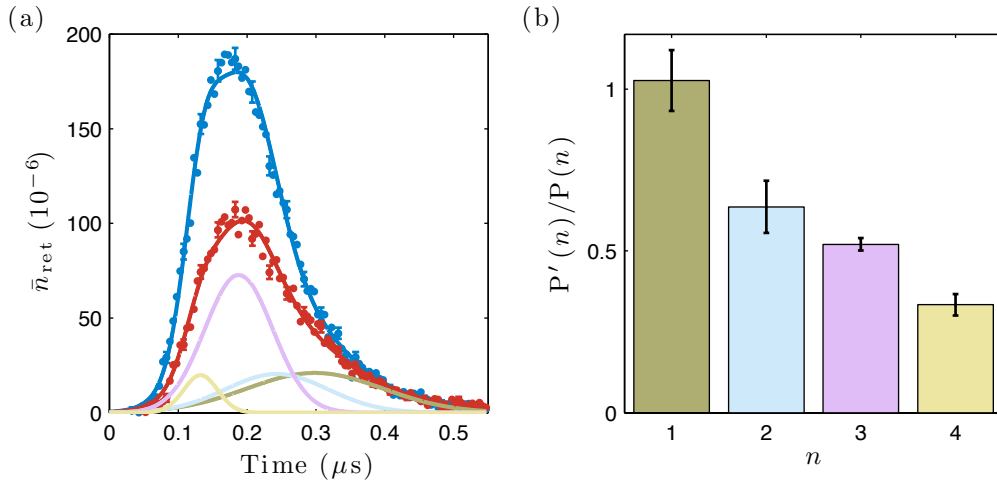


Figure 8.8: Modification of the shape of the retrieved pulse after microwave coupling. (a) Retrieved pulses when no microwave coupling is applied (blue), and with microwave coupling during the storage interval (red). The fits are obtained using equation 7.3. The different modes contributing to the retrieved pulse obtained with microwave coupling are also plotted. (b) For each mode the ratios of the weight parameters used in the fits of the data with and without microwave coupling are plotted. $P'(n)$ denotes the weights in the presence of microwave coupling, and $P(n)$ are the weights when no microwave field is applied.

number distributions is questionable.

8.3.3 Dependence on initial conditions and microwave pulse parameters

The response of the system when changing key experimental parameters will now be studied. This will provide further evidence to support the origin of the dephasing and also allows important parameters to be identified.

The effect of changing the duration of the microwave pulse will first be examined. Rabi oscillations for microwave pulse lengths of 150 ns (blue) and 300 ns (red) are shown in figure 8.9. A large phase shift of approximately π radians is observed between the two data sets. This phase shift is examined more closely in figure 8.10. Each peak of the Rabi oscillations is individually fitted for data sets taken with different microwave pulse lengths. The phase offset of each peak, which corresponds to C_3 in equation 8.5, is obtained

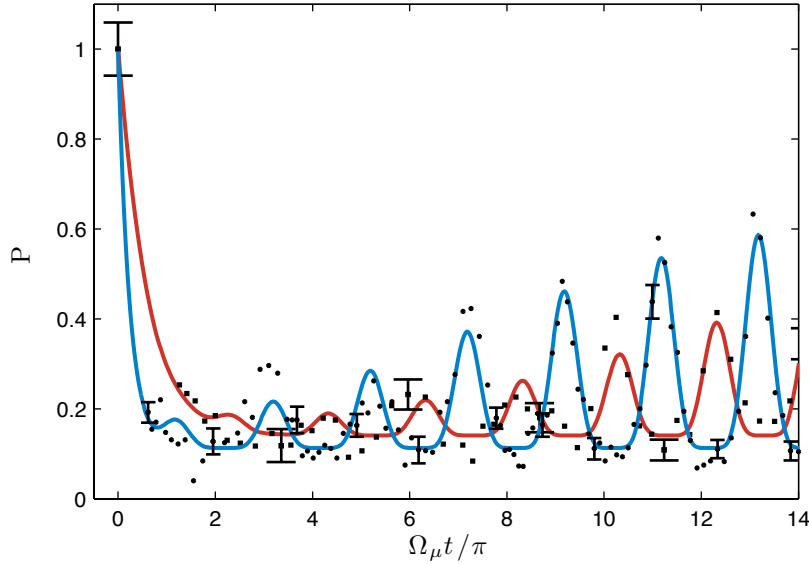


Figure 8.9: Effect of changing the duration of the microwave pulse. The blue (circles) and red (squares) lines correspond to microwave pulse durations of 150 ns and 300 ns respectively. There is a phase shift of approximately π radians between the two data sets.

by fixing the frequency term, C_2 , but allowing all other fit parameters to vary. The tanh envelope and the exponential term are dropped from the fit function. The phase offset gives the deviation from single-particle Rabi oscillations where the peaks are at integer multiples of 2π . In figures 8.10 (a)-(c) the phase offset seems to be largest for the initial peak, before dropping towards a steady value for later peaks. The offset could be caused by an effective detuning of the microwaves caused by the interaction between polaritons. Since the interactions have the largest effect at small Ω_μ this would account for the variation in the phase offset. The phase offset also increases with the duration of the microwave pulse. This behavior could be due to the dependence of the maximum blockade radius for the microwave transition, R_μ , on the duration of the microwave pulse. For very small values of Ω_μ , e.g. around the first peak in the Rabi oscillations, there will be an upper bound on R_μ due to the bandwidth of the microwave pulse (assuming this exceeds the dephasing rate of the microwave transition). This upper bound therefore depends on the duration of the microwave pulse. Since R_μ gives the range of the dipole-dipole interactions this could account for the

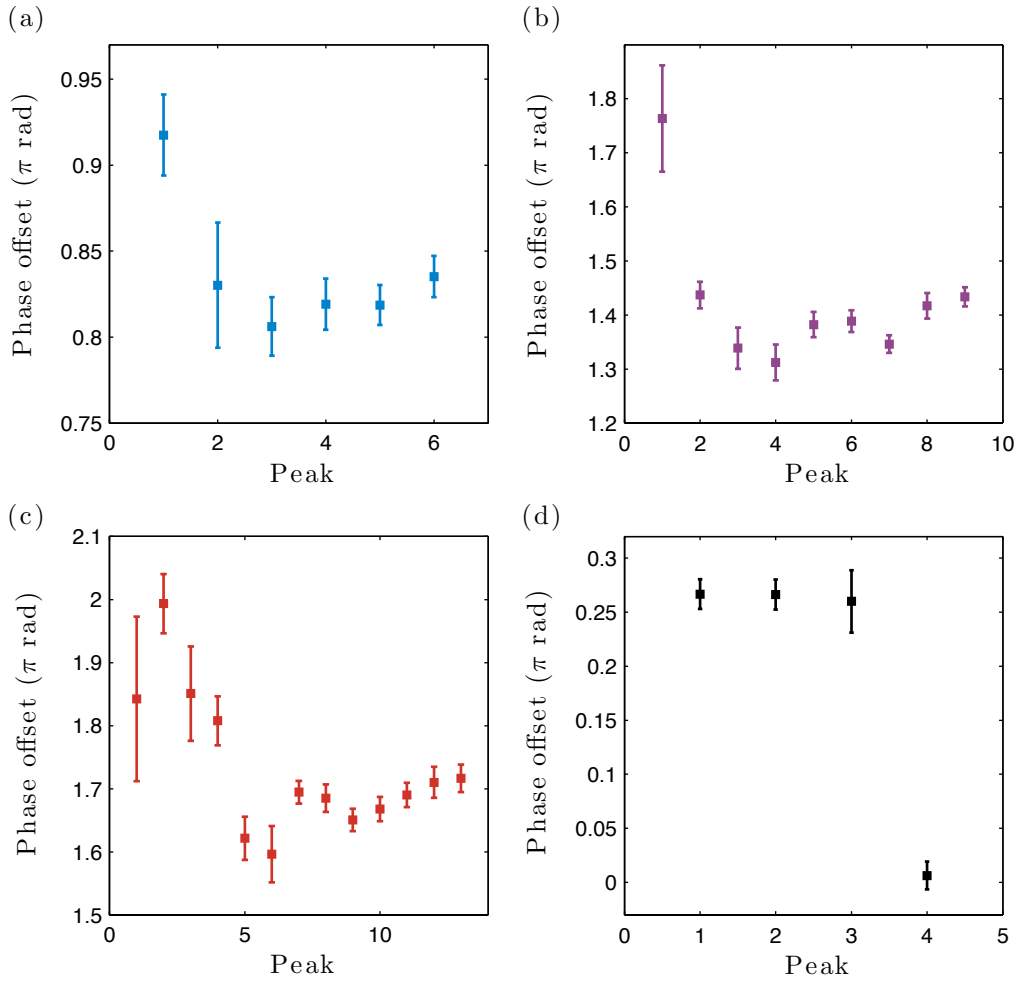


Figure 8.10: Phase shift of individual peaks of Rabi oscillations relative to single-particle oscillations. (a) Microwave pulse length, $t = 150$ ns. (b) $t = 225$ ns. (c) $t = 300$ ns. (d) Control experiment using microwave coupling on the $60s_{1/2}$ to $58p_{3/2}$ transition with $t = 150$ ns.

variation in phase shift with the duration of the microwave pulse. In figure 8.10 (d) where microwave coupling is applied on the weaker $60s_{1/2}$ to $58p_{3/2}$ transition, the phase offset is much smaller. This supports the hypothesis that interaction effects have a role in the observed phase shifts. However, further investigations are required to confirm the origin of these effects.

Another important parameter is the mean number of polaritons in the sample. This can be varied by changing the power of the probe beam. From equation 8.3, for the case of a single polariton i.e. $\mathcal{N} = 1$, the Rabi oscillations should revert to single-particle oscillations. In addition suppression of

the Rabi oscillations should not occur in this case since there are no polariton-polariton interactions. The effect of varying the number of polaritons therefore provides an important test of the origin of the many-body nature and dephasing of the Rabi oscillations. It should be noted that for all of the data presented so far the mean number of retrieved photons in the absence of microwave coupling is roughly $\bar{n}_{\text{ret}} \approx 0.05$. Comparing this value to the data in figure 7.8, it can be seen that the experiments so far have not been performed in the regime where the medium is saturated. In figure 8.11, Rabi oscillations are plotted for two different probe powers. The relative number

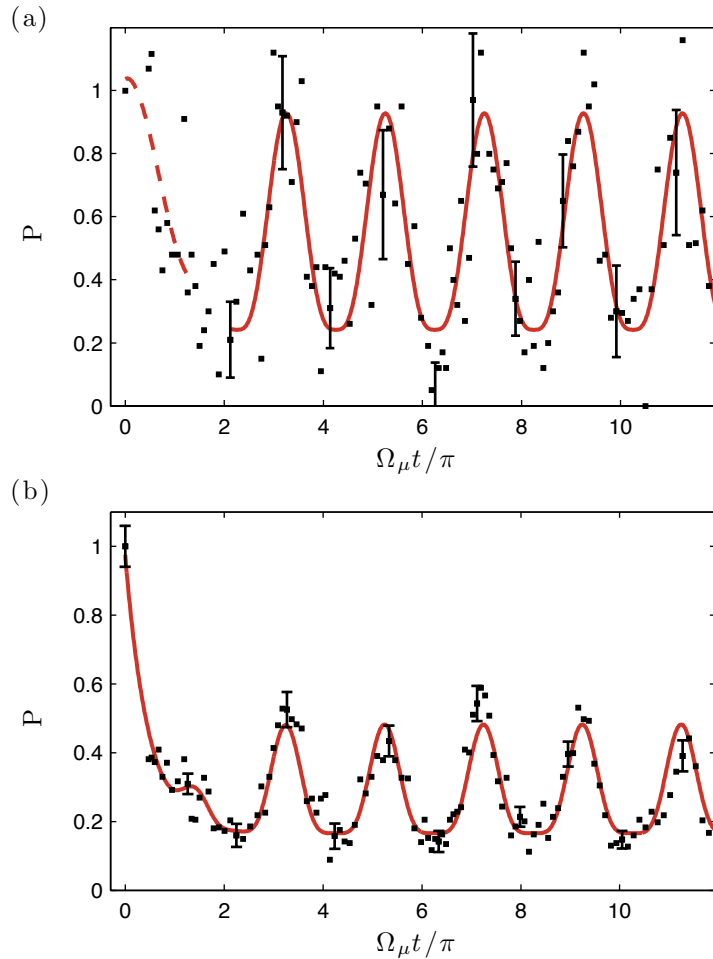


Figure 8.11: Rabi oscillations for two different probe powers. (a) Low probe power where the mean number of retrieved photons in the absence of microwaves is $\bar{n}_{\text{ret}} = (2.6 \pm 0.5) \times 10^{-3}$. From the fit $\mathcal{N} = 1.5 \pm 0.3$. (b) Higher probe power where $\bar{n}_{\text{ret}} = 0.031 \pm 0.002$. Here, $\mathcal{N} = 3.1 \pm 0.3$.

of polaritons written into the sample in each case can be parameterised in terms of the mean number of photons retrieved in the absence of microwaves, \bar{n}_{ret} . As shown in figure 7.8, the number of photons retrieved increases approximately linearly with probe power until the medium is saturated due to dipole blockade. In figure 8.11 (a), where $\bar{n}_{\text{ret}} = (2.6 \pm 0.5) \times 10^{-3}$, the Rabi oscillations have a large amplitude and the many-body nature is not clear. In this case the data at small Ω_μ does not fit to an exponential decay. The dotted line is shown to guide the eye. In figure 8.11 (b), where $\bar{n}_{\text{ret}} = 0.031 \pm 0.002$, the Rabi oscillations are suppressed and the many-body nature is much more apparent.

In figure 8.12 a systematic study of the visibility and many-body character of the Rabi oscillations for different probe powers is presented. The visibility, denoted V in figure 8.12 (a), corresponds to the value of C_1 obtained from the fit function 8.5. Only the first Rabi oscillation, centered around approximately $\Omega_\mu t / \pi = 3$, is fitted since it is the suppression in the dephasing regime

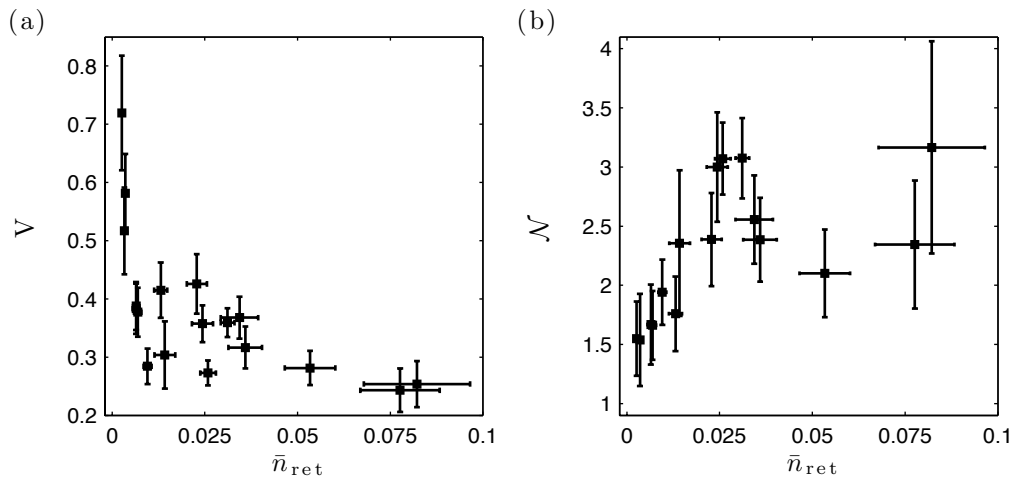


Figure 8.12: Variation of the visibility and many-body nature of the Rabi oscillations as a function of the number of polaritons written. (a) Variation of the visibility, V , of the first peak of the Rabi oscillations. The variable plotted along the x-axis is the mean number of retrieved photons in the absence of microwaves. This is proportional to the mean number of polaritons written (see figure 7.8). (b) Corresponding variation in \mathcal{N} . The values were extracted from a fit of the final three Rabi oscillations (see figure 8.11).

($\hbar\Omega_\mu < V_{\text{dd}}$) that is being studied. As a single peak is fitted, the tanh and exponential terms are dropped from the fit function. It can be seen from figure 8.12 (a) that initially the visibility drops very sharply as the probe power is increased. The decrease in the visibility then slows down at higher probe powers. The fact that the suppression of the Rabi oscillations depends strongly on the number of excitations written into the sample provides strong evidence that the observed dephasing is due to dipole-dipole interactions between polaritons. In figure 8.12 (b) the associated change in \mathcal{N} as the probe power is varied is plotted. To obtain a value representative of the number of polaritons written into the sample, \mathcal{N} was extracted from a fit of the final three Rabi oscillations i.e. in the regime $\hbar\Omega_\mu > V_{\text{dd}}$, where interaction induced dephasing should be suppressed. It can be seen that initially the value of \mathcal{N} seems to increase steadily with increasing probe power. At larger probe powers \mathcal{N} then decreases. This behavior is not understood, although it can be seen that the errors on the values of \mathcal{N} are large. Higher resolution data may be required, especially for large values of \bar{n}_{ret} where large loss rates are observed. Alternatively, the data could imply that the model used to fit the data is not complete.

Another experimental parameter which can be considered is the frequency of the microwave field. In figure 8.13 Rabi oscillations are plotted for microwave frequencies covering a range of 6 MHz. The relative heights of the Rabi oscillations seem to be very sensitive to the microwave detuning. In order to understand this behavior the effect of the microwave detuning on the interaction Hamiltonian in equation 8.7 needs to be included. This is outside the scope of this work.

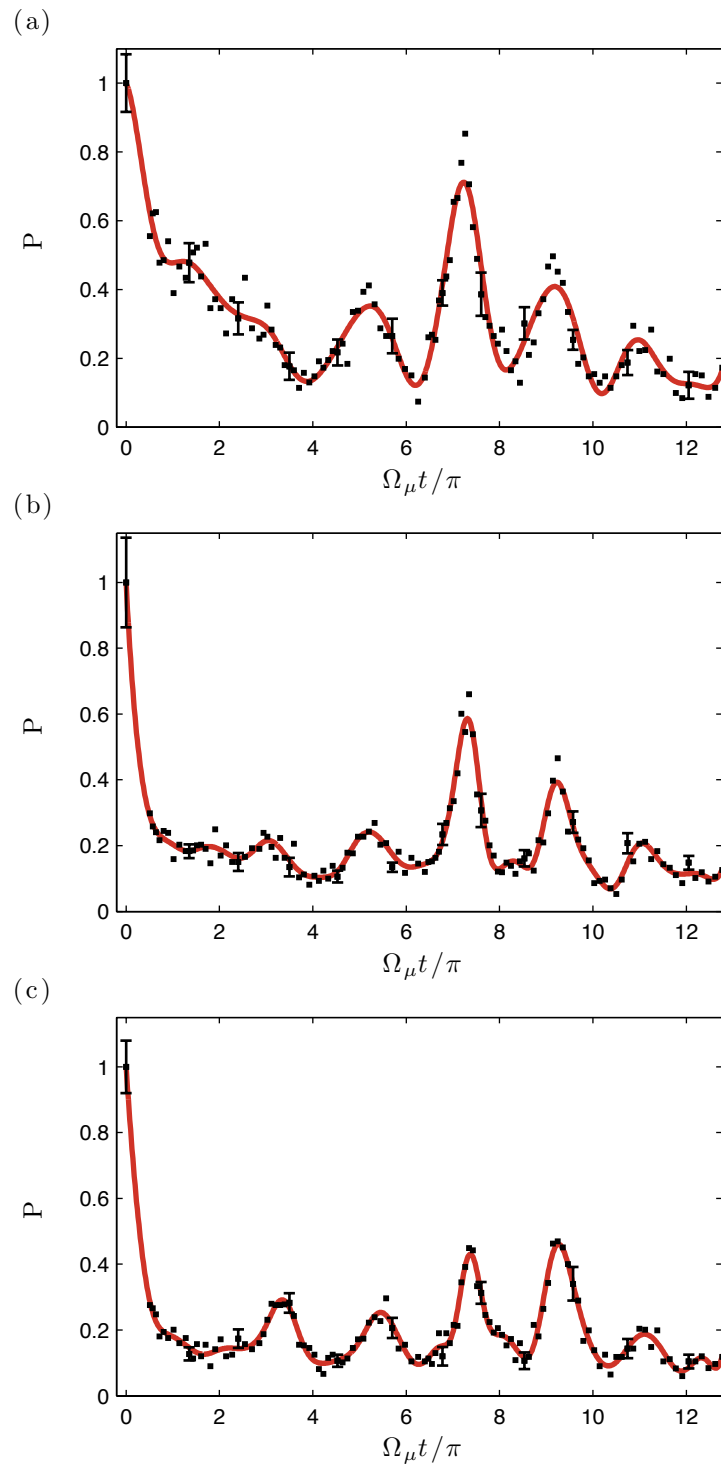


Figure 8.13: Rabi oscillations at different microwave frequencies. (a) Microwave frequency of 18.530 GHz. (b) Microwave frequency of 18.527 GHz. (c) Microwave frequency of 18.524 GHz. The resonance frequency is estimated to be roughly 18.524 GHz. The spline fits are guides to the eye.

Part III

Outlook

Chapter 9

Conclusions and future work

In this thesis the controlled interaction between stored optical photons has been demonstrated. In addition, evidence of non-linear effects associated with photon propagation through the atomic medium has been presented. There is clear scope for improvement of the experiment to enhance these effects and allow further studies to be undertaken. In this chapter an overview of the experimental findings will be given. Following this, potential research directions to pursue in future work will be discussed.

9.1 Overview of the experiment

The experiment described in this thesis concerns the highly non-linear interaction of a weak probe field with a tightly confined atomic cloud. To realise strong coupling of the probe field with the atomic cloud, a pair of high numerical aperture aspheric lenses are mounted inside the vacuum chamber to tightly focus the laser fields. Unfortunately one of these lenses has been partially coated with rubidium resulting in dark spots on the lens surface. In addition, the beam path through the other aspheric lens has been partially blocked by a conducting wire. A consequence of these issues is that the coupling efficiency of the probe beam into a single-mode collection fiber is only around 15%. The signal level is therefore seriously compromised, which is a serious issue when performing time-intensive $g^{(2)}$ measurements.

Another problem with the experiment is the positional instability and low

density of the MOT due to the small angle at which the planar MOT beams intersect. Around 100 atoms can typically be loaded into the dipole trap. The small atom number means that the optical depth of the atomic cloud is low ($OD \approx 1$). The optical depth is important as it governs the size of the slow-light group delay, and the efficiency of photon storage [74]. The low optical depth makes the observation of some effects difficult, and means that the atomic medium is a very inefficient quantum memory.

It has also been observed that the intensity of the microwaves experienced by the atomic cloud is very sensitive to the position of the antenna. This suggests that the reflection of microwaves from metal surfaces forms an interference pattern in the vacuum chamber. These reflections could also compromise the polarisation purity of the microwave field experienced by the atoms.

Despite the problems described above, a number of interesting experiments have been performed. Through the measurement of the photon statistics of an optical field stored in the medium, it has been shown that Rydberg blockade can be exploited to generate non-classical states of light [19–21]. In addition, control of the state of stored photons using a microwave field has been demonstrated. The microwave field has been shown to introduce long-range interactions between the stored photons, with single-photon states preferentially retrieved from the medium. The system therefore provides a potential interface between the optical and microwave domains [124].

9.2 Plans for an improved experimental setup

Many of the experiments performed in this thesis, such as the $g^{(2)}$ measurements or the observation of Rabi oscillations of the stored photons, are very time intensive. For example, the typical time required to perform a single $g^{(2)}$ measurement is around 5-8 hours. The instability of the dipole trap loading is an issue over these long measurement times as it can lead to large fluctuations in the optical depth of the cloud. The poor collection efficiency of the probe field into a single-mode fiber is also a major problem. The range of experiments that can be performed is limited by these issues.

A new experimental setup is being designed and constructed by Hannes

Busche which aims to solve these problems. The new features of this setup include:

- Higher focal length, wedge shaped aspheric lenses inside the vacuum chamber. The new lenses mean that the MOT beams can be arranged in the typical 90° configuration. The problems associated with the small intersection angle of the planar MOT beams in the current experiment will therefore be avoided. In addition, larger MOT beams can be used which will increase the number of captured atoms.
- A new, clean set of aspheric lenses should mean that a much higher collection efficiency of the probe beam is possible.
- A 2D-MOT [125] to provide a source of atoms from which a 3D-MOT will be loaded. The advantages of using this rather than loading the MOT from a background vapor are two-fold. First, the high flux of atoms from the 2D-MOT should allow faster loading of the 3D-MOT. Currently the experimental cycle time is dominated by the MOT loading stage. It is estimated that the experimental cycle time could be reduced from around 2 s to a few 100 ms with the new setup. Secondly, the source of atoms is directional and can therefore be directed away from the aspheric lenses in the vacuum chamber.
- The MOT quadrupole coils will be located inside the vacuum chamber. As a result of this much higher field gradients will be possible allowing a compressed-MOT phase [100] in the experimental cycle.
- As a consequence of the improvements detailed above many more atoms such be loaded into the dipole trap. A much higher optical depth should therefore be achievable. This should lead to improved photon storage and retrieval efficiencies from the sample.
- Microwave antenna will be located inside the vacuum chamber. The fact that there will be fewer metal surfaces between the atomic sample and the antenna will hopefully result in a more uniform microwave field, with better polarisation purity.

The changes detailed above should allow experiments to be performed with a much higher repetition rate. In addition the experiment should be much more stable from shot to shot.

9.3 Future experiments

The improvements described in the previous section should make a range of future experiments feasible. As discussed in chapter 1, one of the long-term goals of this work is to create a phase gate for photons. Some of the experimental demonstrations in this thesis are directly exploited in a scheme proposed by David Paredes [126]. The scheme proposes to use the dipole blockade effect to store single-photons in two spatially resolved sites, from multi-photon input pulses. As discussed in chapter 7, this is possible provided that the blockade radius is larger than the excitation region. The gate operation is realised using a microwave field. In chapter 8 it was shown that a microwave field can be used to control the range of the dipole-dipole interaction between Rydberg atoms, essentially giving an additional blockade radius. It is proposed that the two interaction scales can be used to give a conditional phase acquisition to the stored photon states [126].

The storage of two photons in adjacent sites could also allow spatially resolved studies of resonant dipole-dipole interactions to be undertaken [123]. For example, following the storage of two single photons in different $ns_{1/2}$ Rydberg states, a microwave field could be used to drive one atom into an $n'p_{3/2}$ Rydberg state. Resonant dipole-dipole interactions between the two Rydberg excitations should be manifest as excitation hopping between the two sites. Since only the photon in the $ns_{1/2}$ state can be retrieved, the site from which the photon emerges is sensitive to the dipole-dipole interactions. This could also be exploited in an optical switch, where a photon stored in one site is retrieved from an adjacent site upon application of a microwave field. In addition, it is known that resonant energy exchange plays an important role in the process of photosynthesis [127]. Ultra-cold atoms provide a well-controlled environment where the role of resonant energy transfer in biological systems could potentially be more closely studied.

Appendix A

Appendix

A.1 Dipole trap laser system

As discussed in section 5.1, to reduce the scattering rate of dipole trap light it is necessary to use a trap wavelength which is far-off resonance. In this experiment a trap wavelength of 910 nm is used. This is a convenient wavelength given the beam waist used as relatively little power (≈ 160 mW) is required to give trap depths on the order of mK. The corresponding scattering rate is on the order of 10 Hz. The trap light is generated from a diode laser and is amplified using a second laser. The laser system is described below.

The master laser for the dipole trap is a homebuilt extended cavity diode laser (ECDL) based on the design in [128]. A diagram of the laser assembly is shown in figure A.1 (a). The laser components are mounted on a fine adjustment mirror mount. This provides a stable, compact base for the laser assembly. A holographic diffraction grating is attached to the front plate of the mirror mount, with the laser diode housed in a collimation tube on the back piece of the mount. The fine adjustment screws allow precise variations of the angle of the diffraction grating, and hence the laser wavelength, to be made. The mirror mount sits on a thermo-electric cooler (TEC) which is in thermal contact with a heat-sink. A thermistor is placed inside a hole drilled in the base of the mirror mount. This allows the temperature to be regulated using an external controller which works in conjunction with the TEC.

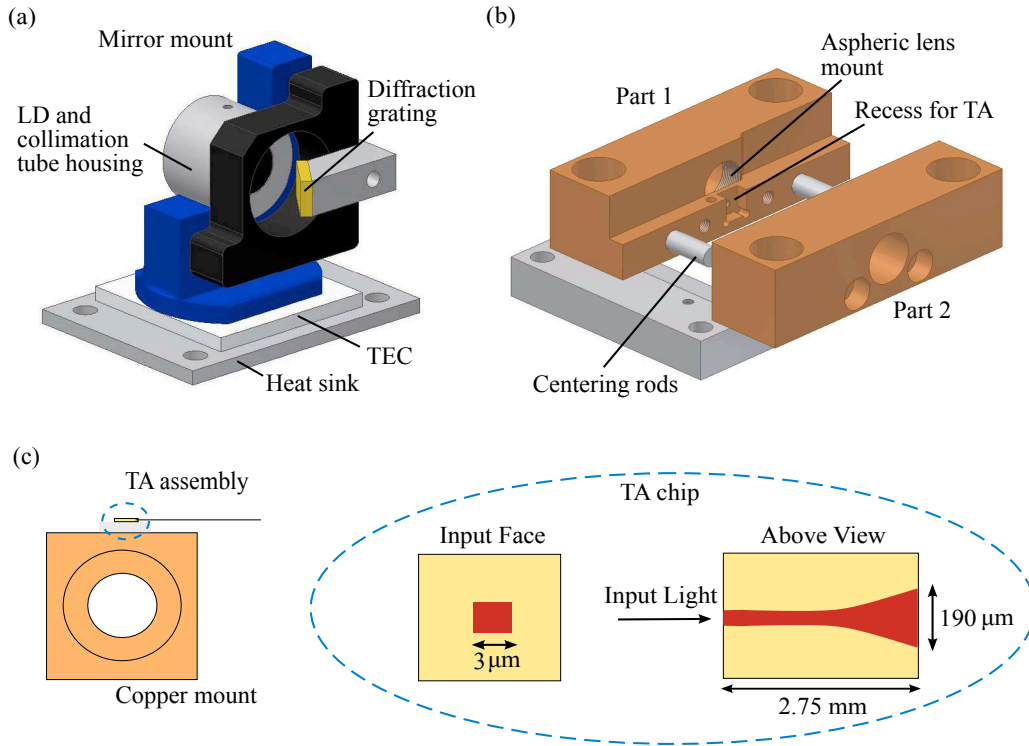


Figure A.1: The home-built laser system used to provide light for the dipole trap. (a) The master laser is an extended cavity diode laser (ECDL) assembled on a fine adjustment mirror mount. The bare laser diode runs at a wavelength of 905 nm. (b) Light from the master laser is amplified using a tapered amplifier (TA). The TA chip is mounted in an assembly consisting of two copper blocks. Aspheric lenses mounted inside the copper blocks provide focusing and subsequent collimation of the light passing through the TA. (c) Schematic showing the structure of the TA chip. The gain region (red) is tapered along the propagation direction of the input light.

Amplification of the light from the master laser is achieved using a home-built tapered amplifier assembly similar to that described in [129]. This is illustrated in figure A.1 (b). A tapered amplifier (TA) has a semiconductor heterojunction structure as in a diode laser. However the ends of the TA chip are antireflection coated so that the incoming light only passes through the gain region once [130]. An illustration of the structure of the TA is shown in figure A.1 (c). It can be seen that the gain medium is tapered along the direction of the input light. The input aperture of the TA is approximately $3 \mu\text{m}$ in size. Due to the small dimensions of the input aperture, the TA must be

mounted such that a well defined alignment can be achieved between the input light and the gain medium. The TA is assembled in a configuration such that the incoming light is focused at the TA's input aperture to a spot size approximately equal to the aperture size. The light then expands through the TA chip filling its gain region. The structure used to mount the TA assembly consists of two copper blocks, each with a circular aperture. The axis going through the center of these apertures defines the optical axis. The piece labeled part 1 in figure A.1 (b) is the copper block which holds the TA chip. This also holds an aspheric lens to focus the incoming light onto the input aperture of the TA. The position of this aspheric lens is adjusted to optimize the input coupling into the TA. The other copper block, labeled part 2, holds an aspheric lens to collimate the output light from the TA. Due to the size and shape of the output aperture of the TA, the output beam is very divergent and astigmatic. The output aspheric lens is therefore used to collimate the vertical axis of the beam, which is the most diverging. A cylindrical lens external to the TA assembly is used to collimate the horizontal axis of the beam. The optical axes of the copper blocks are aligned when bringing them together by centering rods. The two copper blocks are then screwed together. A TEC providing thermal stabilisation is sandwiched between the copper blocks and an aluminium heat sink. The copper blocks are screwed onto the heat sink, using ceramic spacers to thermally isolate the screws from the copper blocks.

The maximum power available from the master laser after optical isolation and beam shaping is 46 mW. This is significantly amplified by the TA. In figure A.2 (a) the output power from the TA as a function of the driving current is plotted for a fixed input power of 46 mW. It can be seen that the output power can exceed 1.2 W. In figure A.2 (b) the output power from the TA is plotted as a function of the input power from the master laser for a fixed driving current. It can be seen that the output power does not quite reach saturation. To achieve the maximum possible output power from the TA a higher power master laser diode would be needed.

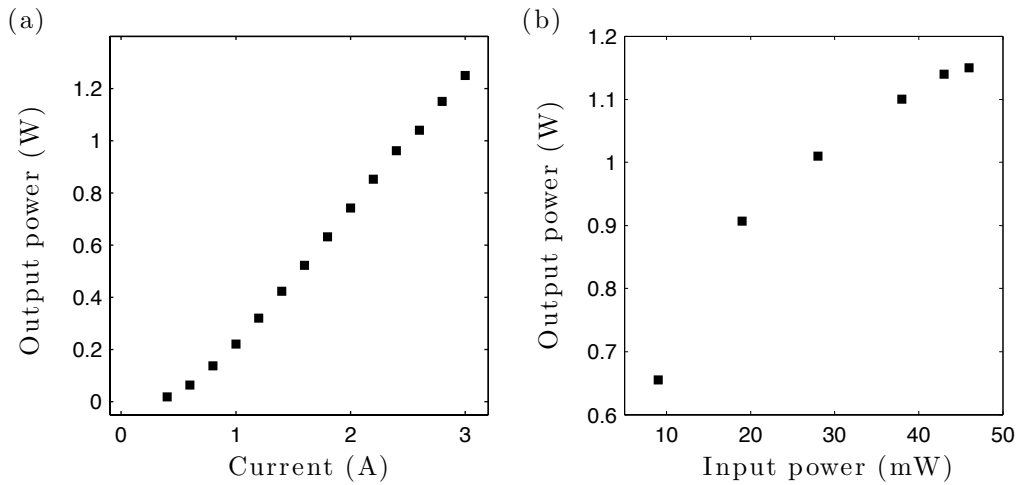


Figure A.2: Characterisation of the output power from the TA. (a) Output power from the TA as a function of driving current. The input power from the master laser is fixed at 46 mW. (b) Output power from the TA as a function of input power from the master laser. The TA driving current is fixed at 2.8 A.

A.2 Crossed dipole trap

To try and reduce the size of the atomic cloud a crossed dipole trap setup was tested. The second, transverse dipole trapping beam crossed the axial trapping beam at 90° . The desired effect of the transverse trap was to compress the atomic cloud longitudinally and therefore reduce the number of Rydberg excitations that could be supported. The high atomic densities achievable in crossed dipole traps have been used to produce BECs [131], and have been successfully used in experiments employing a dynamical reduction of the trap size [132].

In order for the transverse dipole trap to cause a significant longitudinal compression of the atomic cloud a small beam waist was required. A lens system external to the vacuum chamber focused the beam to a waist of $5.7 \pm 0.3 \mu\text{m}$. Due to the small waist of both dipole trap beams, overlapping the two traps is challenging. A variety of diagnostic techniques can be used. Resonant 780 nm light coupled into the transverse trap lens system can be used to image the atoms in the axial dipole trap. Alternatively repump light can be used following the method described in 5.2.3. Both of these

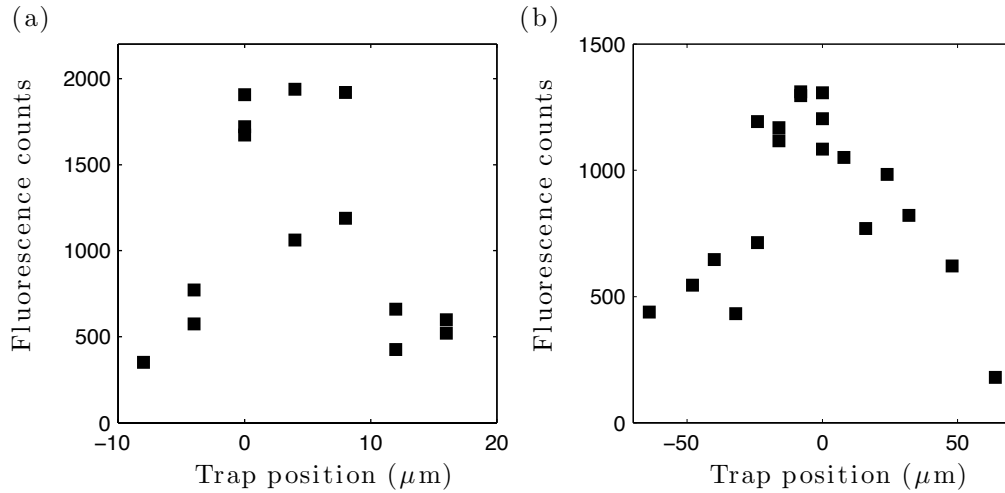


Figure A.3: Fluorescence from dipole trapped atoms as a function of transverse trap position.

techniques were used to roughly overlap the two traps. Following this the fluorescence signal from the dipole trapped atoms was used. Figure A.3 shows the fluorescence signal obtained after loading both traps as a function of the position of the transverse trap. The enhancement in the fluorescence signal obtained when scanning the position of the beam both horizontally and vertically is a signature of the overlap between the two trap beams.

No enhancement in the absorption of the probe field was observed when using the crossed dipole trap. In addition it was found that the position of the transverse trap beam was unstable. For these reasons the crossed trap arrangement was not used in the experiments described in this thesis.

A.3 Absorption spectra of dipole trapped atoms

In figure A.4 the absorption lineshape of the dipole trapped atoms is presented. It can be seen that the absorption lineshapes are blue-shifted for both the axial trap (red data) and cross trap (blue data), relative to that of the untrapped atoms (black data). The lineshapes of the trapped atoms

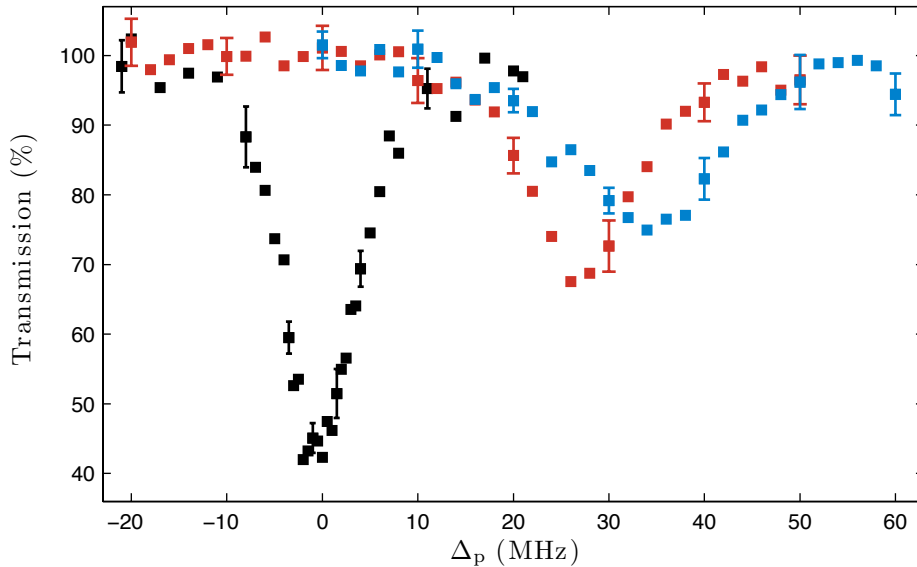


Figure A.4: Absorption spectra of dipole trapped atoms. The center of the absorption lineshape is strongly shifted when the atoms are held in the axial trap (red points) or crossed dipole trap (blue points), relative to the case where the atoms are released from the trap (black points).

are also broader. This is a consequence of that fact that the light shift experienced by an atom depends on its position in the trap. The light shift therefore varies across the atomic cloud, broadening the lineshape relative to the case of a free-space cloud at the same temperature. The inhomogeneous broadening is the reason that experiments are performed on untrapped atoms. The larger the temperature of the cloud, the greater its spatial extent and therefore the greater the broadening. The probe absorption lineshape of the dipole trapped atoms could therefore potentially be used to measure their temperature [133, 134]. However, since the spatial extent of the probe beam is smaller than the atom cloud this method was not employed.

A.4 EIT transients

Most of the data presented in this thesis involves photon counting using SPADs. Since the detection time of every photon count has been recorded, a massive amount of information is accessible when post-processing the data.

For example, one area which has been ignored is the transient effects which arise when switching the intensities of the fields under EIT conditions [135]. In figure A.5 (a) photon counts from the probe beam (red data), which is on EIT resonance, are plotted as a function of time. For reference the background probe signal (blue data) when no atoms are loaded into the dipole trap is also plotted. In both cases the initial increase in the number of photon counts corresponds to the turn-on of the probe beam. Note that the coupling beam is permanently on. At around $1.1 \mu\text{s}$ a microwave field

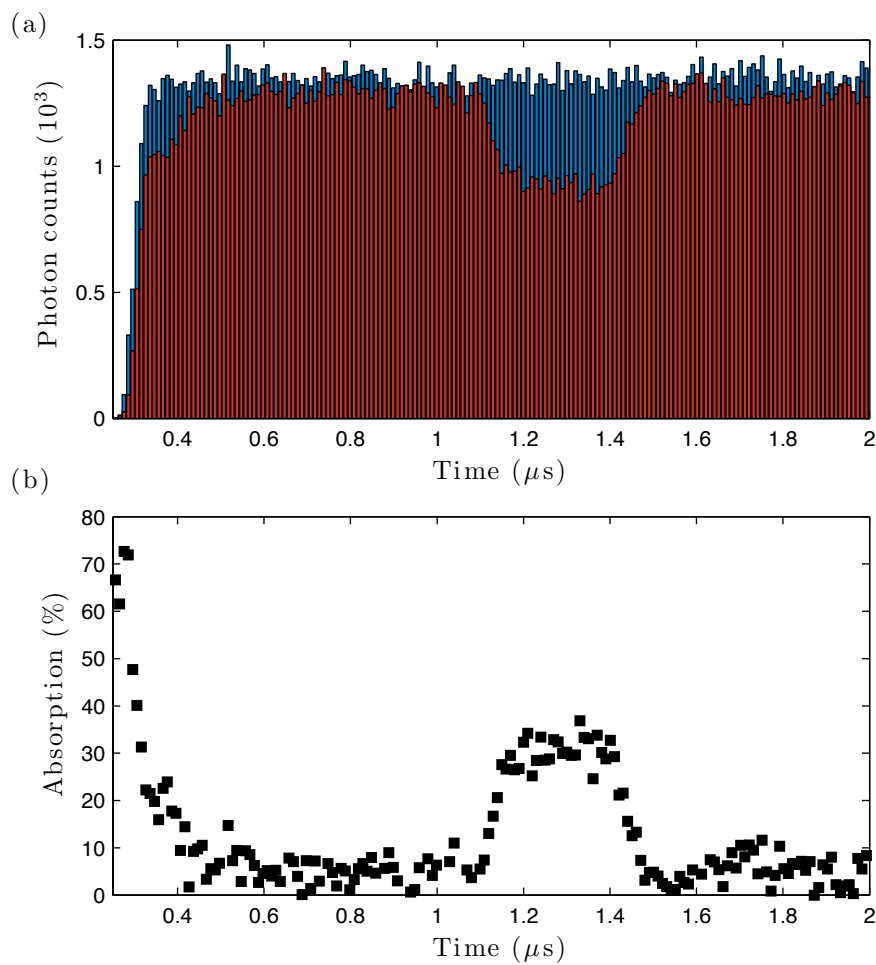


Figure A.5: Transients in EIT. (a) Photon counts from a probe field on EIT resonance (red data), and the corresponding background level (blue data) when no atoms are loaded into the dipole trap. (b) There is initially large absorption of the probe beam before the medium becomes transparent. The increase in absorption at around $1.1 \mu\text{s}$ is due to the application of a microwave field.

is turned on which results in absorption of the probe field (for example see figure 6.6 (c)). In figure A.5 (b) the absorption of the probe beam is plotted as a function of time. It can be seen that the medium is initially absorbing for a few hundred ns before becoming transparent. The transients have not been studied in this experiment but could be an interesting direction for future work in order to understand the role of atomic interactions on the population of the dark-state.

Bibliography

- [1] A. Schawlow and C. Townes, *Infrared and optical masers*, Physical Review **112**, 1940 (1958). [1](#)
- [2] T. Hänsch and A. Schawlow, *Cooling of gases by laser radiation*, Optics Communications **13**, 68 (1975). [1](#)
- [3] D. Wineland, R. Drullinger, and F. Walls, *Radiation-Pressure Cooling of Bound Resonant Absorbers*, Physical Review Letters **40**, 1639 (1978). [1](#)
- [4] M. Nielsen and I. Chuang, *Quantum computation and quantum information* (Cambridge University Press, 2010). [2](#)
- [5] N. Gisin, G. Ribordy, W. Tittel, and H. Zbinden, *Quantum cryptography*, Reviews of modern physics **74**, 145 (2002). [2](#)
- [6] ID Quantique White Paper, *Understanding quantum cryptography*, (Unpublished) (2012). [2](#)
- [7] J. L. O'Brien, *Optical quantum computing.*, Science **318**, 1567 (2007). [2](#), [3](#)
- [8] M. Saffman and T. G. Walker, *Creating single-atom and single-photon sources from entangled atomic ensembles*, Physical Review A **66**, 1 (2002). [2](#), [15](#), [24](#), [25](#), [90](#), [101](#)
- [9] J. Gea-Banacloche, *Impossibility of large phase shifts via the giant Kerr effect with single-photon wave packets*, Physical Review A **81**, 043823 (2010). [2](#), [4](#)
- [10] I. Chuang and Y. Yamamoto, *Simple quantum computer*, Physical Review A **52**, 3489 (1995). [3](#)
- [11] R. W. Boyd, *Nonlinear Optics* (Academic Press). [3](#), [72](#)
- [12] M. Fleischhauer, A. Imamoglu, and J. Marangos, *Electromagnetically induced transparency: Optics in coherent media*, Reviews of Modern Physics **77**, 633 (2005). [3](#), [4](#), [17](#), [20](#), [21](#), [22](#), [23](#), [83](#)
- [13] H. Schmidt and A. Imamoglu, *Giant Kerr nonlinearities obtained by electromagnetically induced transparency.*, Optics letters **21**, 1936 (1996). [3](#)
- [14] J. Shapiro, *Single-photon Kerr nonlinearities do not help quantum computation*, Physical Review A **73**, 062305 (2006). [4](#)

- [15] M. Hosseini *et al.*, *Memory-enhanced noiseless cross-phase modulation*, *Light: Science & Applications* **1**, e40 (2012). [4](#)
- [16] M. Bajcsy *et al.*, *Efficient All-Optical Switching Using Slow Light within a Hollow Fiber*, *Physical Review Letters* **102**, 203902 (2009). [4](#)
- [17] A. Imamolu, H. Schmidt, G. Woods, and M. Deutsch, *Strongly interacting photons in a nonlinear cavity*, *Physical Review Letters* **79**, 1467 (1997). [4](#), [74](#)
- [18] K. M. Birnbaum *et al.*, *Photon blockade in an optical cavity with one trapped atom*, *Nature* **436**, 87 (2005). [4](#), [74](#)
- [19] Y. O. Dudin and a. Kuzmich, *Strongly Interacting Rydberg Excitations of a Cold Atomic Gas.*, *Science* **336**, 887 (2012). [4](#), [5](#), [6](#), [25](#), [90](#), [92](#), [100](#), [122](#)
- [20] T. Peyronel *et al.*, *Quantum nonlinear optics with single photons enabled by strongly interacting atoms.*, *Nature* **488**, 57 (2012). [5](#), [69](#), [72](#), [74](#), [92](#), [94](#)
- [21] D. Maxwell *et al.*, *Storage and Control of Optical Photons Using Rydberg Polaritons*, *Physical Review Letters* **110**, 103001 (2013). [4](#), [6](#), [79](#), [102](#), [107](#), [122](#)
- [22] T. Gallagher, *Rydberg atoms* (Cambridge University Press, 2005). [4](#), [11](#)
- [23] A. Mohapatra, M. Bason, B. Butscher, K. J. Weatherill, and C. S. Adams, *A giant electro-optic effect using polarizable dark states*, *Nature Physics* **4**, 890 (2008). [4](#)
- [24] M. D. Lukin, M. Fleischhauer, and R. Cote, *Dipole blockade and quantum information processing in mesoscopic atomic ensembles*, *Physical Review Letters* **87**, 037901 (2001). [4](#), [14](#), [15](#), [74](#), [101](#)
- [25] S. Harris, *Electromagnetically induced transparency*, *Physics Today* **50**, 36 (1997). [4](#)
- [26] A. Mohapatra, T. Jackson, and C. Adams, *Coherent optical detection of highly excited Rydberg states using electromagnetically induced transparency*, *Physical review letters* **98**, 113003 (2007). [5](#)
- [27] J. D. Pritchard *et al.*, *Cooperative Atom-Light Interaction in a Blockaded Rydberg Ensemble*, *Physical Review Letters* **105**, 193603 (2010). [5](#), [69](#), [72](#), [73](#)
- [28] J. D. Pritchard, A. Gauguier, K. J. Weatherill, and C. S. Adams, *Optical non-linearity in a dynamical Rydberg gas*, *Journal of Physics B: Atomic, Molecular and Optical Physics* **44**, 184019 (2011). [5](#)
- [29] V. Parigi *et al.*, *Observation and Measurement of Interaction-Induced Dispersive Optical Nonlinearities in an Ensemble of Cold Rydberg Atoms*, *Physical Review Letters* **109**, 233602 (2012). [5](#)

-
- [30] I. Friedler, D. Petrosyan, M. Fleischhauer, and G. Kurizki, *Long-range interactions and entanglement of slow single-photon pulses*, Physical Review A **72**, 043803 (2005). 5
- [31] L. M. Duan, M. D. Lukin, J. I. Cirac, and P. Zoller, *Long-distance quantum communication with atomic ensembles and linear optics.*, Nature **414**, 413 (2001). 5
- [32] A. I. Lvovsky, B. C. Sanders, and W. Tittel, *Optical quantum memory*, Nature Photonics **3**, 706 (2009). 5
- [33] B. Julsgaard, J. Sherson, J. Cirac, J. Fiurášek, and E. Polzik, *Experimental demonstration of quantum memory for light*, Nature **432**, 482 (2004). 5
- [34] H. D. Riedmatten, M. Afzelius, and M. Staudt, *A solid-state lightmatter interface at the single-photon level*, Nature **456**, 773 (2008). 5
- [35] M. Hedges, J. Longdell, Y. Li, and M. Sellars, *Efficient quantum memory for light*, Nature **465**, 1052 (2010). 5
- [36] J. Fekete, D. Rieländer, M. Cristiani, and H. D. Riedmatten, *Ultranarrow-Band Photon-Pair Source Compatible with Solid State Quantum Memories and Telecommunication Networks*, Physical Review Letters **110**, 220502 (2013). 5
- [37] M. D. Eisaman *et al.*, *Electromagnetically induced transparency with tunable single-photon pulses.*, Nature **438**, 837 (2005). 5, 6
- [38] T. Chanelière *et al.*, *Storage and retrieval of single photons transmitted between remote quantum memories.*, Nature **438**, 833 (2005). 5, 6
- [39] Y. Dudin, L. Li, and A. Kuzmich, *Light storage on the time scale of a minute*, Physical Review A **87**, 031801(R) (2013). 5, 26
- [40] S. Zhang, S. Zhou, M. Loy, G. Wong, and S. Du, *Optical storage with electromagnetically induced transparency in a dense cold atomic ensemble*, Optics letters **36**, 4530 (2011). 6
- [41] I. Novikova *et al.*, *Optimal Control of Light Pulse Storage and Retrieval*, Physical Review Letters **98**, 243602 (2007). 6
- [42] Y.-H. Chen *et al.*, *Coherent Optical Memory with High Storage Efficiency and Large Fractional Delay*, Physical Review Letters **110**, 083601 (2013). 6
- [43] M. Saffman, T. G. Walker, and K. Mølmer, *Quantum information with Rydberg atoms*, Reviews of Modern Physics **82**, 2313 (2010). 11, 12
- [44] D. Jaksch *et al.*, *Fast quantum gates for neutral atoms*, Physical review letters **85**, 2208 (2000). 11
- [45] C. Brau, *Modern problems in classical electrodynamics* (OUP USA, 2003). 11

- [46] T. Walker and M. Saffman, *Consequences of Zeeman degeneracy for the van der Waals blockade between Rydberg atoms*, Physical Review A **77**, 032723 (2008). [11](#), [12](#)
- [47] J. D. Pritchard, *Cooperative Optical Non-linearity in a blockaded Rydberg Ensemble*, PhD thesis, 2011. [12](#), [17](#), [18](#), [20](#), [21](#), [23](#), [29](#), [30](#), [31](#), [37](#), [46](#), [60](#), [70](#), [72](#), [74](#), [104](#)
- [48] K. Safinya, J. Delpech, and F. Gounand, *Resonant Rydberg-atom-Rydberg-atom collisions*, Physical Review Letters **47**, 405 (1981). [13](#)
- [49] I. Mourachko *et al.*, *Many-body effects in a frozen Rydberg gas*, Physical review letters **80**, 253 (1998). [13](#)
- [50] J. Petrus, *ac electric-field-induced resonant energy transfer between cold Rydberg atoms*, Journal of Physics B: **41**, 245001 (2008). [13](#)
- [51] M. Tanasittikosol *et al.*, *Microwave dressing of Rydberg dark states*, Journal of Physics B: Atomic, Molecular and Optical Physics **44**, 184020 (2011). [13](#), [75](#), [103](#), [106](#)
- [52] E. Brekke, J. O. Day, and T. G. Walker, *Excitation suppression due to interactions between microwave-dressed Rydberg atoms*, Physical Review A **86**, 033406 (2012). [13](#), [75](#), [101](#)
- [53] D. Comparat and P. Pillet, *Dipole blockade in a cold Rydberg atomic sample*, Journal of the Optical Society of America B **27**, A208 (2010). [14](#)
- [54] D. Averin and K. Likharev, *Coulomb blockade of single-electron tunneling, and coherent oscillations in small tunnel junctions*, Journal of low temperature physics **62**, 345 (1986). [14](#)
- [55] R. Heidemann *et al.*, *Evidence for Coherent Collective Rydberg Excitation in the Strong Blockade Regime*, Physical Review Letters **99**, 163601 (2007). [14](#)
- [56] E. Urban, T. Johnson, and T. Henage, *Observation of Rydberg blockade between two atoms*, Nature Physics **5**, 110 (2009). [14](#)
- [57] D. Tong *et al.*, *Local Blockade of Rydberg Excitation in an Ultracold Gas*, Physical Review Letters **93**, 063001 (2004). [14](#)
- [58] T. Liebisch, A. Reinhard, P. Berman, and G. Raithel, *Atom counting statistics in ensembles of interacting Rydberg atoms*, Physical review letters **95**, 253002 (2005). [14](#)
- [59] A. Schwarzkopf, R. Sapiro, and G. Raithel, *Imaging spatial correlations of Rydberg excitations in cold atom clouds*, Physical Review Letters **107**, 103001 (2011). [15](#)

- [60] P. Schauß, M. Cheneau, M. Endres, and T. Fukuhara, *Observation of spatially ordered structures in a two-dimensional Rydberg gas*, Nature **491**, 87 (2012). [15](#)
- [61] T. Pohl, E. Demler, and M. D. Lukin, *Dynamical Crystallization in the Dipole Blockade of Ultracold Atoms*, Physical Review Letters **104**, 043002 (2010). [15](#)
- [62] A. Gaëtan *et al.*, *Observation of collective excitation of two individual atoms in the Rydberg blockade regime*, Nature Physics **5**, 115 (2009). [15](#), [97](#)
- [63] L. Pedersen and K. Mølmer, *Few qubit atom-light interfaces with collective encoding*, Physical Review A **79**, 012320 (2009). [15](#)
- [64] J. Gea-Banacloche, Y. Li, S. Jin, and M. Xiao, *Electromagnetically induced transparency in ladder-type inhomogeneously broadened media: Theory and experiment*, Physical Review A **51**, 576 (1995). [17](#), [20](#), [21](#)
- [65] C. Cohen-Tannoudji, J. Dupont-Roc, and G. Grynberg, *Atom-Photon Interactions* (Wiley VCH, 1998). [17](#), [18](#), [44](#)
- [66] C. J. Foot, *Atomic Physics* (OUP Oxford, 2004). [19](#)
- [67] M. D. Lukin *et al.*, *Spectroscopy in Dense Coherent Media: Line Narrowing and Interference Effects*, Physical Review Letters **79**, 2959 (1997). [22](#)
- [68] L. Hau, S. Harris, Z. Dutton, and C. Behroozi, *Light speed reduction to 17 metres per second in an ultracold atomic gas*, Nature **397**, 594 (1999). [22](#)
- [69] M. Kash *et al.*, *Ultraslow Group Velocity and Enhanced Nonlinear Optical Effects in a Coherently Driven Hot Atomic Gas*, Physical Review Letters **82**, 5229 (1999). [22](#)
- [70] M. Fleischhauer and M. D. Lukin, *Dark-state polaritons in electromagnetically induced transparency*, Physical Review Letters **84**, 5094 (2000). [23](#)
- [71] C. Liu, Z. Dutton, C. H. Behroozi, and L. V. Hau, *Observation of coherent optical information storage in an atomic medium using halted light pulses.*, Nature **409**, 490 (2001). [24](#), [25](#)
- [72] D. Phillips, A. Fleischhauer, and A. Mair, *Storage of light in atomic vapor*, Physical Review Letters **86**, 783 (2001). [24](#), [25](#)
- [73] M. Fleischhauer and M. D. Lukin, *Quantum memory for photons: Dark-state polaritons*, Physical Review A **65**, 022314 (2002). [24](#)
- [74] A. Gorshkov, A. André, M. Fleischhauer, A. Sørensen, and M. D. Lukin, *Universal Approach to Optimal Photon Storage in Atomic Media*, Physical Review Letters **98**, 123601 (2007). [24](#), [122](#)
- [75] N. Phillips, A. Gorshkov, and I. Novikova, *Optimal light storage in atomic vapor*, Physical Review A **78**, 023801 (2008). [24](#), [82](#), [89](#)

- [76] F. Bariani and T. A. B. Kennedy, *Retrieval of multiple spin waves from a weakly excited, metastable atomic ensemble*, Physical Review A **85**, 033811 (2012). [24](#), [25](#), [82](#)
- [77] A. Gorshkov, A. André, M. D. Lukin, and A. Sørensen, *Photon storage in Λ -type optically dense atomic media. II. Free-space model*, Physical Review A **76**, 033805 (2007). [25](#)
- [78] S. D. Jenkins, T. Zhang, and T. A. B. Kennedy, *Motional dephasing of atomic clock spin waves in an optical lattice*, Journal of Physics B: Atomic, Molecular and Optical Physics **45**, 124005 (2012). [25](#), [33](#)
- [79] R. Zhao *et al.*, *Long-lived quantum memory*, Nature Physics **5**, 100 (2008). [25](#)
- [80] M. Tanasittikosol, *Rydberg dark states in external fields*, PhD thesis, 2011. [26](#)
- [81] K. J. Weatherill, *A CO₂ Laser Lattice Experiment for Cold Atoms*, PhD thesis, 2007. [31](#)
- [82] R. P. Abel *et al.*, *Laser frequency stabilization to excited state transitions using electromagnetically induced transparency in a cascade system*, Applied Physics Letters **94**, 071107 (2009). [32](#)
- [83] D. Steck, *Rubidium 87 D line data*, (Unpublished) (2001). [32](#)
- [84] C. S. Adams and E. Riis, *Laser cooling and trapping of neutral atoms*, Progress in quantum electronics. **21**, 1 (1997). [34](#)
- [85] P. D. Lett *et al.*, *Optical molasses*, Journal of the Optical Society of America B **6**, 2084 (1989). [37](#)
- [86] C. Townsend, N. Edwards, and C. Cooper, *Phase-space density in the magneto-optical trap*, Physical Review A **52**, 1423 (1995). [37](#)
- [87] M. Fox, *Quantum Optics: An Introduction* (OUP Oxford, 2006). [38](#)
- [88] R. Loudon, *The Quantum Theory of Light* (OUP Oxford, 2000). [39](#), [40](#)
- [89] L. Mandel, *Sub-Poissonian photon statistics in resonance fluorescence*, Optics Letters **4**, 205 (1979). [39](#)
- [90] R. Alléaume, F. Treussart, J.-M. Courty, and J.-F. Roch, *Photon statistics characterization of a single-photon source*, New Journal of Physics **6**, 85 (2004). [39](#)
- [91] P. Grangier, G. Roger, and A. Aspect, *Experimental evidence for a photon anticorrelation effect on a beam splitter: a new light on single-photon interferences*, Europhysics Letters **173** (1986). [39](#)
- [92] L. Mandel and E. Wolf, *Optical Coherence and Quantum Optics* (Cambridge University Press, 1995). [41](#)

- [93] E. Kreyszig, *Advanced Engineering Mathematics* (John Wiley & Sons, 1999). 41
- [94] M. Orrit, *Photon Statistics in Single Molecule Experiments*, *Single Molecules* **3**, 255 (2002). 42
- [95] R. Grimm, M. Weidemüller, and Y. Ovchinnikov, *Optical dipole traps for neutral atoms*, *Adv. At. Mol. Opt. Phys* **42**, 39 (2000), 9902072. 43, 44, 45, 46
- [96] J. Miller, R. Cline, and D. Heinzen, *Far-off-resonance optical trapping of atoms*, *Physical Review A* **47**, R4567 (1993). 44
- [97] W. Silfvast, *Laser fundamentals* (Cambridge University Press, 2008). 45
- [98] S. Kuppens, K. Corwin, and K. Miller, *Loading an optical dipole trap*, *Physical review A* **62**, 1 (2000). 48, 51, 61, 62, 66
- [99] S. Chu, J. Bjorkholm, A. Ashkin, and A. Cable, *Experimental observation of optically trapped atoms*, *Physical Review Letters* **57**, 314 (1986). 52
- [100] W. Petrich, M. Anderson, J. Ensher, and E. Cornell, *Behavior of atoms in a compressed magneto-optical trap*, *JOSA B* **11**, 1332 (1994). 52, 123
- [101] M. Bajcsy *et al.*, *Laser-cooled atoms inside a hollow-core photonic-crystal fiber*, *Physical Review A* **83**, 063830 (2011). 57
- [102] L. Isenhower, W. Williams, A. Dally, and M. Saffman, *Atom trapping in an interferometrically generated bottle beam trap*, *Optics letters* **34**, 1159 (2009). 57
- [103] A. Fuhrmanek, R. Bourgain, Y. Sortais, and A. Browaeys, *Light-assisted collisions between a few cold atoms in a microscopic dipole trap*, *Physical Review A* **062708**, 1 (2012). 62
- [104] J. Weiner, V. Bagnato, S. Zilio, and P. Julienne, *Experiments and theory in cold and ultracold collisions*, *Reviews of Modern Physics* **71**, 1 (1999). 62
- [105] M. Mudrich *et al.*, *Sympathetic Cooling with Two Atomic Species in an Optical Trap*, *Physical Review Letters* **88**, 253001 (2002). 65
- [106] C. Tuchendler, A. Lance, and A. Browaeys, *Energy distribution and cooling of a single atom in an optical tweezer*, *Physical Review A* **78**, 033425 (2008). 66
- [107] C. S. Hofmann *et al.*, *Sub-Poissonian statistics of Rydberg-interacting dark-state polaritons*, *Physical Review Letters* **110**, 203601 (2012), arXiv:1211.7265v1. 69, 72, 94
- [108] A. V. Gorshkov, J. Otterbach, M. Fleischhauer, T. Pohl, and M. D. Lukin, *Photon-Photon Interactions via Rydberg Blockade*, *Physical Review Letters* **107**, 133602 (2011). 69, 92

- [109] I. Beterov, I. Ryabtsev, D. Tretyakov, and V. Entin, *Quasiclassical calculations of blackbody-radiation-induced depopulation rates and effective lifetimes of Rydberg nS , nP , and nD alkali-metal atoms*, Physical Review A **79**, 052504 (2009). [71](#)
- [110] S. Sevinçli, N. Henkel, C. Ates, and T. Pohl, *Nonlocal Nonlinear Optics in Cold Rydberg Gases*, Physical Review Letters **107**, 153001 (2011). [72](#), [73](#), [74](#)
- [111] D. Petrosyan, J. Otterbach, and M. Fleischhauer, *Electromagnetically Induced Transparency with Rydberg Atoms*, Physical Review Letters **107**, 213601 (2011). [73](#), [74](#)
- [112] K. Singer and J. Stanojevic, *Long-range interactions between alkali Rydberg atom pairs correlated to the $nsns$, $nprp$ and $ndnd$ asymptotes*, Journal of Physics B: Atomic, Molecular and Optical Physics **38**, S295 (2005). [74](#)
- [113] J. A. Sedlacek *et al.*, *Microwave electrometry with Rydberg atoms in a vapour cell using bright atomic resonances*, Nature Physics **8**, 819 (2012). [75](#)
- [114] W. Li, I. Mourachko, M. Noel, and T. Gallagher, *Millimeter-wave spectroscopy of cold Rb Rydberg atoms in a magneto-optical trap: Quantum defects of the ns , np , and nd series*, Physical Review A **67**, 052502 (2003). [77](#)
- [115] Y. Dudin, F. Bariani, and A. Kuzmich, *Emergence of spatial spin-wave correlations in a cold atomic gas*, Physical Review Letters **109**, 133602 (2012). [94](#)
- [116] C. Ates, S. Bettelli, T. Fernholz and I. Lesanovsky, *Private communication*. [97](#), [99](#)
- [117] G. Nikoghosyan and M. Fleischhauer, *Photon-Number Selective Group Delay in Cavity Induced Transparency*, Physical Review Letters **105**, 013601 (2010). [99](#)
- [118] H. Tanji-Suzuki, W. Chen, R. Landig, J. Simon, and V. Vuletić, *Vacuum-induced transparency.*, Science **333**, 1266 (2011). [99](#)
- [119] F. Bariani, Y. Dudin, T. Kennedy, and A. Kuzmich, *Dephasing of multiparticle Rydberg excitations for fast entanglement generation*, Physical review letters **108**, 030501 (2012). [100](#), [103](#), [108](#), [110](#)
- [120] J. Stanojevic *et al.*, *Generating non-Gaussian states using collisions between Rydberg polaritons*, Physical Review A **86**, 021403 (2012). [100](#), [103](#), [108](#)
- [121] M. Rose, *Elementary Theory of Angular Momentum* (Dover Publications Inc., 1995). [102](#)
- [122] C. Ates, A. Eisfeld, and J. Rost, *Motion of Rydberg atoms induced by resonant dipole dipole interactions*, New Journal of Physics **10**, 045030 (2008). [107](#)

-
- [123] C. van Ditzhuijzen *et al.*, *Spatially Resolved Observation of Dipole-Dipole Interaction between Rydberg Atoms*, Physical Review Letters **100**, 243201 (2008). [107](#), [124](#)
- [124] D. Petrosyan and M. Fleischhauer, *Quantum Information Processing with Single Photons and Atomic Ensembles in Microwave Coplanar Waveguide Resonators*, Physical Review Letters **100**, 170501 (2008). [122](#)
- [125] K. Dieckmann, R. Spreeuw, M. Weidemüller, and J. Walraven, *Two-dimensional magneto-optical trap as a source of slow atoms*, Physical Review A **58**, 3891 (1998). [123](#)
- [126] D. P. Barato, *All-optical quantum information processing using Rydberg gates*, In preparation . [124](#)
- [127] G. Panitchayangkoon *et al.*, *Direct evidence of quantum transport in photosynthetic light-harvesting complexes.*, Proceedings of the National Academy of Sciences of the United States of America **108**, 20908 (2011). [124](#)
- [128] A. S. Arnold, J. S. Wilson, and M. G. Boshier, *A simple extended-cavity diode laser*, Review of Scientific Instruments **69**, 1236 (1998). [125](#)
- [129] R. A. Nyman *et al.*, *Tapered-amplified antireflection-coated laser diodes for potassium and rubidium atomic-physics experiments*, Review of Scientific Instruments **77**, 033105 (2006). [126](#)
- [130] J. N. Walpole, *Semiconductor amplifiers and lasers with tapered gain regions*, Optical and quantum electronics **28**, 623 (1996). [126](#)
- [131] M. Barrett, J. Sauer, and M. Chapman, *All-Optical Formation of an Atomic Bose-Einstein Condensate*, Physical Review Letters **87**, 010404 (2001). [128](#)
- [132] T. Kinoshita, T. Wenger, and D. Weiss, *All-optical Bose-Einstein condensation using a compressible crossed dipole trap*, Physical Review A **71**, 011602 (2005). [128](#)
- [133] A. Fuhrmanek, *From single to many atoms in a microscopic dipole trap*, PhD thesis, 2011. [130](#)
- [134] M. Schulz, *Tightly confined atoms in optical dipole traps*, PhD thesis, 2002. [130](#)
- [135] Y. Q. Li and M. Xiao, *Transient properties of an electromagnetically induced transparency in three-level atoms.*, Optics letters **20**, 1489 (1995). [131](#)